

University of Nevada, Reno

Study of Aerosol-Cloud Interactions for Shallow Warm Clouds

A dissertation submitted in partial fulfillment of the requirements for the degree of

Doctor of Philosophy in Atmospheric Science

By

Lan Gao

Dr. Eric M Wilcox/Dissertation Advisor

August, 2018



THE GRADUATE SCHOOL

We recommend that the dissertation
prepared under our supervision by

LAN GAO

Entitled

Study Of Aerosol-Cloud Interactions For Shallow Warm Clouds

be accepted in partial fulfillment of the
requirements for the degree of

DOCTOR OF PHILOSOPHY

Dr. Eric M. Wilcox, Advisor

Dr. Douglas H. Lowenthal, Committee Member

Dr. Hans Moosmuller, Committee Member

Dr. David L. Mitchell, Committee Member

Dr. Mae S. Gustin, Graduate School Representative

David W. Zeh, Ph. D., Dean, Graduate School
August, 2018

ABSTRACT

Cumulus clouds are generally optically thick and shallow, exerting a net cooling impact on the climate system. Changes in atmospheric aerosol conditions, especially aerosol concentration increased by anthropogenic activity, can alter cloud microphysics (e.g., droplet concentration, size distribution) and cloud macrophysics (e.g., liquid water path, cloud morphology), thereby affecting cloud albedo and the Earth's radiation budget. To deepen our understanding of aerosol-cloud-radiation interactions and to investigate the errors (e.g., due to sampling scale, remote sensing artifactual retrieval) in assessing the aerosol effects on shallow cloud and associated radiative forcing, a comprehensive study was performed by utilizing the surface station, in situ aircraft, satellite remote sensing measurements and three-dimensional radiative transfer simulations.

The study over the Northern Indian Ocean revealed that more polluted clouds were substantially deeper and narrower with greater cloud liquid water path than less polluted clouds. The observed deeper clouds, mainly due to the warmer, more humid and shallower boundary layer. The narrower clouds formed in high polluted condition were caused by the intensified cloud edge evaporation effect, as a result of more and smaller cloud droplets induced by increasing aerosol concentration. The deeper and narrower clouds embedded in a high concentration of absorbing aerosols over this region contribute to a brighter atmosphere as viewed from space compared to cleaner conditions. As a consequence, the regional negative solar shortwave forcing at the top of the atmosphere due to aerosols increases in magnitude (i.e., greater cooling of regional

climate) with increasing aerosol optical depth more than is contributed by just the direct effect of aerosols alone.

Aerosol effects on continental shallow warm cloud were investigated by using multiple airborne and spaceborne remote sensing observations. Aerosol-cloud relationships were investigated under different meteorological conditions. Results showed that Cloud responses to aerosols were highly affected by lower tropospheric stability and free troposphere relative humidity. The Aerosol-cloud interaction index (ACI) was generally higher in an unstable and humid environment and lower under unstable and dry conditions. The total top of atmosphere cloud radiative forcing was calculated to be $\sim -80 \text{ W m}^{-2}$ when the ACI reached 0.3. Aerosol indirect forcing of the estimated anthropogenic portion of the aerosol due to the intrinsic aerosol effect, i.e., on cloud albedo, was estimated to be -0.63 W m^{-2} and the forcing due to the extrinsic aerosol effect, i.e., on cloud extent, was estimated to be -1.77 W m^{-2} .

The errors due to sampling scale and remote sensing retrieval artifacts in quantifying aerosol indirect effects on shallow warm cloud were investigated by utilizing remote sensing, in situ data and a Monte Carlo Radiative Transfer model (MCRT) designed by the author. The ACI showed a strong scale-dependent behavior, which decreases as data resolution decreases. Smoothing of aerosol and cloud fields from 1 to 10 km produced a decrease of $\sim 60\%$ in estimated ACI. The ACI estimated from 1-km resolution remote sensing data was similar to that derived from in-situ aircraft measurements. Analysis of aircraft data revealed that the aerosol humidification effect accounts for a $\sim 18.7\text{-}21.8\%$ decrease in estimate ACI. The MCRT simulation indicated

that the three-dimensional radiative transfer effect from cloud side multiple scattering reduced estimated ACI by $\sim 10\%$ for a broken cloud scene.

As the coupling among aerosol, cloud, radiation, and the meteorological condition is very complex, the integration of in-situ aircraft measurement, large-scale satellite observation, meteorological reanalysis data, and atmospheric modeling improves our understanding of this complex system.

I dedicate my doctorate dissertation to my beloved family, for their constant support and unconditional love.

There are no words to convey how much I love you.

Acknowledgments

First of all, I greatly thank my advisor, Dr. Eric M Wilcox, for offering me the opportunity to explore the fascinating aerosol-cloud interactions using various tools, from airborne based field observations, satellite measurements, to modeling. He allowed me freedom to develop independent research ideas. I thank him for all the patient guidance and for being so available for students. In addition, I appreciate his sharp perspectives and superb knowledge of science, as well as his positive attitude especially when facing difficulties. I have been extremely lucky to have such an advisor, and I hope that I could be as humility and enthusiastic as Dr. Wilcox.

I also thank my committee members, Dr. Douglas H. Lowenthal, Dr. Mae S. Gustin, Dr. Hans Moosmuller and Dr. David L. Mitchell, for their knowledge and scientific advice during my Ph.D. education and their constructive comments that helped to improve my research work. Special thanks to Dr. Douglas H. Lowenthal for his tremendous help with this dissertation.

Sincere thanks to all of my colleagues at Desert Research Institute (DRI) and the University of Nevada Reno (UNR), for their support and help during my Ph.D. career. I am lucky to have this opportunity to collaborate with such genius and enthusiastic research groups.

The support from my friends meant a lot to me. Special thanks go to Zhiqiang Fan for sharing tremendous experience and ideas. I thank Yunpeng Shan, Yang Han, Xia Sun, Farnaz Hosseinpour, Marco Giordano, Jingting Huang, Deep Sengupta, Ehsan Mosadegh

Anbaran and Yazeed Alsubhi for the caring and encouragement during my graduate study at DRI. I thank my old friend Wei Jiang for the mentally support overseas.

I cannot begin to express my gratitude to my family for all of the love, support, and encouragement they have sent my way along this journey. To my parents, thank you for being my champions throughout the past many years. Your unconditional love and support have meant the world to me, I hope that I have made you proud. My greatest appreciation goes to Ling. We met while we were in high school, and she unwittingly committed herself to over ten long years with a struggling and occasionally starving student. In spite of that, she has been terrifically supportive throughout. Finally, special thanks to my little one Olivia. You have made me stronger, better and more fulfilled than I could have ever imagined. I love you forever!

Table of Contents

ABSTRACT	i
Acknowledgments	v
List of Tables	ix
List of Figures	xi
List of Abbreviations	xviii
List of Symbols	xxi
Chapter 1	1
1 General overview	1
2 Aerosol effects on shallow boundary layer clouds	3
3 Current challenges and uncertainties in studying aerosol-cloud interactions	5
3.1 Field experiment limitations	6
3.2 Satellite observation limitations	7
4 Chapter overview	9
Reference	11
Chapter 2	18
1 Introduction.....	21
2 Data and methods.....	24
2.1 Airborne measurements from UAV	24
2.2 Ground measurements at the MCOH	26
2.3 Spaceborne measurements from satellite.....	28
3 Results and discussion	29
3.1 Background conditions during CARDEX	29
3.2 Aerosol effects on cloud microphysics	30
3.3 Aerosol effects on cloud macrophysics.....	33
3.4 Aerosol perturbed cloud radiative forcing.....	37
3.5 Correlation between meteorology and aerosol-cloud properties.....	38
4 Conclusions.....	39
<i>Acknowledgments</i>	41
Reference	42

Chapter 3	63
1 Introduction.....	66
2 Data and Methods	69
2.1 Data Description	69
2.2 Aerosol-Cloud Interaction Index	73
2.3 Methods.....	74
3 Results and discussion	77
3.1 The effect of aerosol on cloud properties constrained by large-scale dynamics	77
3.2 Aerosol-Cloud-Interaction as a function of dynamics.....	80
3.3 ACI-CRF relationships and aerosol indirect forcing.....	81
4 Conclusions.....	82
<i>Acknowledgments</i>	85
References.....	86
Chapter 4	101
1 Introduction.....	104
2 Data, model, and methods.....	106
2.1 Data description.....	106
2.2 Model design.....	107
2.3 Methods.....	111
3 Results and discussion	113
3.1 ACI spatial scale dependence.....	113
3.2 Aerosol near clouds.....	114
3.3 Aerosol humidification effect	116
3.4 Three-dimensional radiative transfer effect.....	118
4 Conclusions.....	119
References.....	121
Chapter 5	138
1 Summary and conclusions	139
2 Future work.....	143

List of Tables

Chapter 2

Table 1: List of data and instruments used in this study. The temporal and spatial resolution of data, instrument detection limit and precision, and platforms where the measurements took place are shown in this table.....	47
Table 2: Average value and one standard deviation of aerosol and cloud properties during CARDEX compared to MAC 2006 and INDOEX 1999. Note: 1) CARDEX results were filtered by PWV to only consider the dry days, the MAC and INDOEX results were not filtered by water vapor conditions; 2) the criterion used to determine aerosol conditions in CARDEX and MAC are, Case L ($N_a < 1000 \text{ cm}^{-3}$), Case M ($1000 \text{ cm}^{-3} < N_a < 1500 \text{ cm}^{-3}$) and Case H ($N_a > 1500 \text{ cm}^{-3}$), but in INDOEX results, the Case L* corresponds to $N_a < 500 \text{ cm}^{-3}$, Case M* corresponds to N_a between 500 and 1500 cm^{-3} , the Case H is defined the same as CARDEX and MAC; 3) CARDEX and MAC results were reported as average values while INDOEX results were reported as median values.....	49
Table 3: Linear regression analysis of surface aerosol number concentration and cloud LWP with dynamical parameters in the March 2012 ECMWF ERA-Interim reanalysis at the model grid cell corresponding to the MCOH station. Correlation coefficients (r) are shown with the sign of the relationship. To compare with measured aerosol and cloud properties, the ECMWF reanalysis data (6-hour) was interpolated into 1-hour temporal resolution to match hourly mean aerosol and cloud parameters.....	50

Chapter 3

Table 1. List of data used in this study and which data can be used to solve specific questions.....	89
--	----

Table 2. The slope of linear fit between cloud properties and aerosol, separated for non-precipitating and precipitating clouds. The sign indicates the relationship between variables.....	90
Table 3. Four conditions were defined to study aerosol-cloud relationships in different regimes.....	90
Table 4. TOA aerosol indirect radiative forcing estimated for shortwave and longwave components from all samples. The radiative forcing was separated for intrinsic and extrinsic forcing.....	90

Chapter 4

Table 1. Data used in this study from SEAC ⁴ RS campaign and selected to answer the objectives of this study: (a) Investigate biases from the spatial scale of measurements; (b) Investigate biases from artifacts in remote sensing retrievals; (c) Investigate biases from aerosol humidification and 3-D radiative transfer effect.....	123
Table 2. The parameters used in MCRT simulation and the sources of those variables. Here ‘scene’ represents each simulated eMAS scene.....	124
Table 3. Comparison of ACI calculated from aircraft, eMAS, and MODIS at different resolutions. The R ² of ACI and HP was shown in this table. The differences of ACI due to smoothing data from 1 km to 10 km, and due to artifactual retrieval were calculated. The red color represents ACI calculated using all data, and the blue data represents the ACI calculated using uncontaminated data.....	125
Table 4. Comparison of ACI calculated using contaminated and uncontaminated data. Variations of ACI caused by aerosol humidification effect and 3-D radiation transfer effect were also shown in this table. Red color represents ACI calculated using maximum hygroscopic growth factor, and blue color represents ACI calculated using minimum hygroscopic growth factor.....	125

List of Figures

Chapter 2

Figure 1: The flight patterns of aerosol payload UAV (left) and cloud payload UAV (right) on March 11, 2012. The color bars represent aerosol number concentration (N_a , cm^{-3}) and cloud droplet number concentration (N_d , cm^{-3}) along the trajectories respectively. The aerosol UAV typically spiraled up to 3 km to measure the profile of particles and performed several level flights on the descending leg to measure the aerosol absorption coefficient as shown in the figure. The cloud UAV typically first ascended to an altitude to penetrate the cloud horizontally and randomly, then ascended to another altitude to do the cloud penetration. On March 11, an elevated aerosol layer with N_a greater than 2000 cm^{-3} can be seen clearly from 1.5 to 2 km height and the cloud layer is right beneath the aerosol layer with N_d close to 500 cm^{-3} 51

Figure 2: a) Time series of surface aerosol number concentration from CPC, AOD from AERONET and MODIS during CARDEX. b) Comparison between surface CPC and UAV measured aerosol number concentration within the boundary layer. Each dot represents the mean with crosses represent the standard deviations. c) Comparison between AERONET and MODIS measured AOD. MODIS AOD at 550 nm was directly obtained from MODIS Level 2 aerosol product with spatial resolution at 10 km. AERONET AOD at 550 nm was linearly interpolated over the natural logarithm of the spectral bands at 470, 675, and 870 μm52

Figure 3: The PDF of the cloud droplet number concentration N_d , cloud droplet effective radius R_e , and liquid water content (LWC) for two pollution conditions with mean values reported in the figure (panel a, b, and e, the red line/number represents Case H, and the blue line/number represents Case L). The cloud droplet size distribution (CDS) for cloud center and cloud edge under the two conditions (panel c and d). The cloud center and edge are distinguished using the following criterion: define a cloud point where the measured cloud droplet

number concentration is greater than 50 cm^{-3} and cloud liquid water content is greater than 0.01 g m^{-3} (refers to McFarquhar and Heymsfield (2001)), at least four consecutive cloud points can be considered as a cloud penetration (i.e., cloud width $> 100 \text{ m}$). For each cloud penetration, take an average of the middle two points to represent the cloud center, and the average of the first and last points is treated as cloud edge.....53

Figure 4: (a) Cloud droplet number concentration N_d versus the aerosol number concentration N_a during CARDEX (red) and MAC (green) with the mean and standard deviation indicated by the crosses, and INDOEX (blue) with the median value. (b), (c) and (d), the same as (a) but the Y axes represent cloud droplet effective radius, liquid water path, and cloud width, respectively. Note: INDOEX results from Heymsfield and McFarquhar (2001) only show the ranges of condensation nuclei concentration (Table 2), so for convenience of visualization, the N_a values for INDOEX were assigned as Case L ($N_a=500 \text{ cm}^{-3}$), Case M ($N_a=1000 \text{ cm}^{-3}$) and Case H ($N_a=1500 \text{ cm}^{-3}$).....55

Figure 5: Cloud width as a function of average peak cloud liquid water path (LWP). Here cloud width was given by the consecutive cloudy points (shown in left Y-axis) and then estimated using the number of cloudy points multiplied by the mean UAV penetration speed. Each dot represents the mean value with error bars represent the standard deviations. A total of 376 cloud penetrations were selected. Dot size corresponds to the number of samples in that aerosol bin, where the smallest dot represents 38 samples and the largest dot represents 143 samples. The color bar represents the aerosol concentration. The upper-level wind is usually considered as an important factor regulating cloud morphology. To test if wind speed plays a role in affecting cloud width, the wind horizontal speed at cloud layer was compared for Case H and L, shown in the subplot located in the right bottom corner. The wind speed was derived from 3-D wind probe onboard the UAV. From bottom to top, the symbols represent 10%, 25%, 50%, average (triangle), 75%, and 90% value respectively. To test the quality of derived wind

speed, the assimilated wind speed from MERRA reanalysis was also compared with UAV measured wind speed (Fig. 6 left panel).....56

Figure 6: Comparison of cloud layer horizontal wind speed derived from UAV and MERRA (left panel) shows good agreement. The cloud LWP as a function of cloudy points estimated from MWR (right panel). Here the cloudy point was flagged by using surface MWR retrieval. Red symbols represent Case H and blue symbols represent Case L.....57

Figure 7: Cloud top height (CTH) and cloud base height (CBH) as a function of binned AOD. Each symbol represents the mean of samples in the corresponding AOD bin and the error bars represent the standard deviation. For example, the very left circle (triangle) represents the mean of CTH (CBH) with AOD between 0 and 0.1. The CTH was obtained from MODIS Level 2 cloud products with high spatial resolution at 1 km and was filtered when CTP is less than 700 hPa and CTT greater than 273 K to only consider the low-level cumulus clouds. The CBH was obtained from ground-based MPL and data was filtered when CBH is greater than 2 km.....58

Figure 8: PDF of virtual potential temperature perturbation θ'_v (left panel) and daily averaged θ'_v for Case L and Case H (right panel). The θ'_v was calculated by subtracting the θ_v from the mean of each cloud penetration. Here Case L - represents the daily mean of negative θ'_v in Case L while Case H - represents the daily mean of negative θ'_v in Case H. The same definition applies for Case L + and Case H +. The sum of absolute values of both negative and positive θ'_v is proportional to the magnitude of horizontal buoyancy gradient, which can serve as a metric to determine the cloud side evaporation-cooling effect.....59

Figure 9: TOA cloud shortwave forcing and aerosol direct forcing as a function of AOD. TOA cloud SW forcing was calculated using the CERES observed TOA cloudy SW flux minus the clean-clear flux. The dashed purple line represents the average cloud SW forcing for all data, and the solid red line with error bars (standard deviation) represents the cloud SW forcing for dry days only. The dashed green

line and solid blue line represent the average aerosol direct forcing induced by particle scattering for all data and dry days only, respectively.....60

Chapter 3

Figure 1. The histogram of cloud top effective radius and classification of non-precipitating ($R_e \leq 12 \mu\text{m}$, blue) and precipitating ($R_e \geq 16 \mu\text{m}$, red) clouds according to cloud top R_e . The transition clouds with R_e between 12 and 16 μm may be drizzling but not as strong as precipitating clouds. It is difficult to determine these clouds only by cloud top R_e . Therefore, we excluded these clouds in the analysis from controlling the data quality. N denotes the number of samples in each classification. The total number of samples in this analysis is 9076.....91

Figure 2. An example showing the differences in LWP constrained and unconstrained ACI for one eMAS scene. ACI calculated from (a) all data, and binned for a LWP range of (b) 50-70 g m^{-2} and (c) 100-120 g m^{-2} and (d) 140-160 g m^{-2} . The ACILWP in panel (a) denotes the averaged and LWP constrained ACI, while the ACI_{all} denotes the unconstrained ACI calculated directly from all dataset.....92

Figure 3. Flowchart of this study showing the steps to solve the research questions. The CTP, CTT, R_e represent cloud top pressure, cloud top temperature and cloud top effective radius. NAM represents the North American Mesoscale Forecast System reanalysis data.....93

Figure 4. Cloud properties and number of samples as a function of each AOD bin. The points represent the mean value of cloud properties for each AOD bin and the bars on each point are the standard error of the cloud properties in each AOD bin. Cloud properties include cloud fraction (CF), effective radius (R_e), cloud liquid water path (LWP), cloud optical thickness (COT), cloud top/base height (CTH/CBH) and cloud thickness. Here, AOD was divided into 10 bins. The right bottom panel shows the number of samples in each AOD bin.....94

- Figure 5. The histogram of lower tropospheric stability (LTS) and free troposphere relative humidity (RH_{ft}) for two precipitation conditions.....95
- Figure 6. Similar to Fig.4, but the relationships between AOD and cloud properties (CF, Re, LWP, COT, cloud thickness) were constrained by LTS and separated by higher LTS (>12 K, red) and lower LTS (<9 K, blue).....96
- Figure 7. Similar to Fig.6, but the relationships between AOD and cloud properties (CF, Re, LWP, COT, cloud thickness) were constrained by RH_{ft} and separated by higher RH_{ft} ($>80\%$, red) and lower RH_{ft} ($<70\%$, blue).....97
- Figure 8. ACI calculated by using COT and AOD under four different meteorological conditions and separated by non-precipitating/precipitating conditions. Four meteorological conditions are unstable/dry, unstable/wet, stable/dry and stable/wet, which are determined by LTS and RH_{ft} . ACI for non-precipitating/precipitating clouds is shown in blue and red, respectively. The ACI was calculated at the 95% confidence level.....98
- Figure 9. The TOA shortwave cloud radiative forcing (Panel a), TOA longwave cloud radiative forcing (Panel b) and TOA net cloud radiative forcing (Panel c) as a function of ACI. Each dot represents the mean forcing and ACI calculated for each eMAS scene. The best fitting and equation with R square are shown in the figure.....99

Chapter 4

- Figure 1. The algorithm flowchart for the Monte Carlo Radiative Transfer model used in this study. Here w represents the photon weight, (x, y, z) represents the position of the photon, (n_x, n_y, n_z) represents the direction of movement, τ_{free} represents the free optical path that a photon can travel without any interactions.....126
- Figure 2. Example of constructing three-dimensional cloud field using collocated CPL and eMAS data. Data obtained from eMAS measurement on Aug. 30 2013 (leg 9). CPL footprint overlay on eMAS image (Panel a). The library (Panel b) of cloud

- optical thickness, effective radius, cloud top temperature and extinction profiles used to compare with the off-nadir pixel from eMAS retrieval.....127
- Figure 3. Flowchart of this study showing the steps to solve the research questions.....128
- Figure 4. The ACI calculated from eMAS (red), MODIS (purple) and aircraft (DC-8, blue), as well as the homogeneity parameter (green) as a function of data resolution ranging from 1 km to 10 km (Panel a). The linear relationship between eMAS derived ACI and homogeneity parameter calculated using Eq. 10 (Panel b).....129
- Figure 5. An example scene where AOD (aerosol optical depth) was aggregated from 0.5 km to 10 km resolution (from panel 1 to panel 7). This process significantly smoothed out the signal of AOD, reducing the standard deviation of AOD without changing its mean.....130
- Figure 6. eMAS image of cloud mask (Panel a) on the 30 Aug 2013. Coinciding aerosol optical depth retrieved from eMAS (Panel b). Separated contaminated (red) and uncontaminated (blue) aerosol retrievals (Panel c) determined by using the 4 km critical distance for this scene.....131
- Figure 7. AOD (Panel a) and Angstrom exponent (Panel b) as a function of the distance from each aerosol pixel to its nearest cloud pixel. The blue squares represent the mean of $AOD/\text{\AA}$ in each distance bin. Blue bars represent the standard deviation of $AOD/\text{\AA}$. Red points represent number of samples in each bin.....132
- Figure 8. ACI calculated using all data (red, contaminated) and uncontaminated (blue) data with resolution aggregated from 1 km to 10 km.....133
- Figure 9. Profiles of RH and AOD (Panel a and b) measured from DC-8 aircraft. Aerosol hygroscopic growth factor as a function of RH (Panel c). The AOD profile was obtained from 4STAR which was installed on the top of aircraft and measures the AOD above the aircraft.....134
- Figure 10. Frequency distribution (%) of DC-8 aircraft in-situ measured clear sky RH. In this figure, only clear sky data points are included. To determine the clear sky

measurement, we first checked the cloud droplet number concentration and liquid water content sampled from the cloud probe. If cloud probe shows there is no cloud droplet in the sample, and then we classify the measured RH for clear sky, otherwise, we classify as cloudy sky.....135

Figure 11. The enhancement of TOA reflectance for clear sky pixels only simulated from MCRT model. The color bar represents the magnitude of enhancement.....136

List of Abbreviations

ACI: Aerosol Cloud Interaction

AOD: Aerosol Optical Depth

AI: Aerosol Index

APR: advanced Airborne Precipitation Radar

BC: Black carbon

CB(T)H: Cloud Base (Top) Height

CALIPSO: Cloud-Aerosol Lidar and Infrared Pathfinder Satellite Observations

CARDEX: Cloud, Aerosol, Radiative forcing, Dynamics Experiment

CCN: Cloud Condensation Nuclei

CERES: Clouds and Earth's Radiant Energy System

CF: Cloud Fractional cover

CPC: Condensation Particle Counter

CPL: Cloud Physics Lidar

CTT(P): Cloud Top Temperature (Pressure)

DC-8: NASA's aircraft laboratory

ER-2: NASA's sub-orbital aircraft laboratory

eMAS: enhanced MODIS Airborne Simulator

ECMWF: European Center for Medium-range Weather Forecasts

GOES: Geostationary Operational Environmental Satellite

HYSPLIT: HYbrid Single-Particle Lagrangian Integrated Trajectory model

IPCC AR5: Fifth Assessment Report of the Intergovernmental Panel on Climate Change

INDOEX: The Indian Ocean Experiment

LCL: Lifting Condensation Level

LTS: Lower Tropospheric Stability (K)

LWC: Liquid water content (g m^{-3})

LWP: Liquid water path (g m^{-2})

MAC: Maldives Autonomous unmanned aerial vehicle Campaign

MCOH: Maldives Climate Observatory Hanimaadhoo

MCRT: Monte Carlo Radiative Transfer

MODIS: MODerate resolution Imaging Spectroradiometer

MPL: Micropulse lidar

MWR: Microwave radiometer

NAM: North American Mesoscale Forecast System

PBL: Planetary boundary layer (also BL)

PWV: Precipitable water vapor (kg m^{-2})

RH: Relative humidity (%)

SEAC⁴RS: The Studies of Emissions and Atmospheric Composition, Clouds and Climate Coupling by Regional Surveys

SSA: Single Scattering Albedo

TOA: Top of Atmosphere

UAV: Unmanned Aerial Vehicle

List of Symbols

\AA : Ångström exponent

\mathbf{d} : Divergence (s^{-1})

θ : Potential temperature (K)

θ_e : Equivalent potential temperature (K)

θ_v : Virtual potential temperature (K)

N_a : Aerosol number concentration (cm^{-3})

N_d : Cloud droplet number concentration (cm^{-3})

P : Pressure (hPa)

ρ : Density (g m^{-3})

R_e : Cloud droplet effective radius (μm)

τ : Optical thickness

τ_{free} : Optical distance that a photon can travel freely

ϵ : random number

T : Temperature (K)

ω : Pressure vertical velocity (Pa s^{-1})

w : Photon weight (unit weight 1)

g : Asymmetry parameter

\mathbf{nx} , \mathbf{ny} , \mathbf{nz} : Unit vector along x, y and z axis

Chapter 1

Introduction

1 General overview

Atmospheric aerosols have increased dramatically since the pre-industrial era due to human activity. The quantitative impact of these aerosols on Earth's radiative budget continues to elude the scientific community. Although numerous studies have been performed over the last few decades applying field campaigns, satellite measurements, and numerical models, our understanding of aerosol effects on climate is still highly uncertain, which hampers the estimation and prediction of the anthropogenic contribution to climate change (Boucher et al., 2013).

Aerosols can affect climate in many ways. First, aerosols can scatter sunlight back to space causing direct radiative forcing. Second, aerosols can serve as cloud condensation nuclei (CCN) or ice nuclei (IN) for cloud particles and alter the albedo of clouds. The ability of an aerosol to serve as an efficient CCN or IN depends on its size, mass, shape and chemical composition (Seinfeld and Pandis, 2012). The relationship between the amount of aerosol and cloud base number of droplets is complex, but usually more aerosols will result in more droplets near cloud base (Ramanathan et al., 2001), although this depends on the types of the aerosols (Rosenfeld et al., 2002). All other things being equal, especially the cloud's geometric size and total condensed water content, more numerous smaller droplets result in the "Twomey" effect or first aerosol indirect effect

(AIE) whereby the overall increased droplet surface area increases the cloud albedo, producing a negative indirect radiative forcing (Twomey, 1974;Twomey, 1977). Third, the reduced cloud droplet size can affect the precipitation efficiency, tending to increase the cloud liquid water content, thus the cloud lifetime (Albrecht, 1989). This is so-called second AIE or cloud lifetime effect. The delay in precipitation may cause droplets to ascend to supercooled levels (Andreae et al., 2004) and may further invigorate convective clouds (Rosenfeld et al., 2008).

In addition, aerosol absorption of sunlight may decrease low cloud cover by heating the air, reducing the relative humidity, and evaporating the cloud droplets. This process leads to positive radiative forcing, termed as the “semi-direct effect” (Hansen et al., 1997;Ackerman et al., 2000;Kaufman and Koren, 2006). Aerosol absorption can also decrease the solar radiation reaching the surface and increase low-level static stability, leading to lower surface moisture fluxes (Ramanathan et al., 2001;Koren et al., 2004). This could also reduce cloud cover, or the probability of cloud formation, thus reducing rainfall. However, when the absorbing aerosol resides above a low cloud deck, the absorption of sunlight by the aerosols causes a reduction in cloud top entrainment that enhances the cloud development (Wilcox, 2010;Johnson et al., 2004). Besides the mechanisms mentioned above, aerosols can induce some other cloud-mediated climatic effects, which act through changing precipitation processes (Charlson and Heintzenberg, 1995;Lohmann and Feichter, 2005;Rosenfeld et al., 2008;Boucher et al., 2013).

AIE could be large enough to offset much of the global warming induced by anthropogenic greenhouse gases, yet even after decades of research, the magnitude is still

very uncertain (Myhre et al., 2013). The range in overall aerosol forcing since 1750 is estimated to be between -0.1 and -1.9 W m^{-2} (Myhre et al., 2013). The large uncertainty is partly due to lack of understanding of aerosol-cloud interaction feedbacks at different scales and regimes, and partly due to limited techniques used to study aerosol-cloud interactions. This requires more systematic studies under different cloud dynamics, aerosol loadings, and spatiotemporal scales. In addition, measurement techniques and data sampling need to be improved in the future. The focus of this study is on warm water cloud responses to aerosol perturbations and the uncertainty in quantifying the aerosol indirect effect.

2 Aerosol effects on shallow boundary layer clouds

Aerosol effects on shallow boundary layer clouds have been studied for decades with most of the focus on marine stratocumulus (Twohy, 2005; Wood, 2007; Wilcox, 2010; Goren and Rosenfeld, 2012, 2014, 2015) and trade cumulus (Xue and Feingold, 2006; Roberts et al., 2008; Dey et al., 2011; Yuan et al., 2011; Pistone et al., 2016). This is because they are very susceptible to aerosol loading and their important roles in the regional and global energy budget and the hydrological cycle (Wood, 2012; Rosenfeld et al., 2014). Strong longwave cooling at the cloud top is the main driver of the overturning convective circulations that constitute the key dynamical elements of these clouds (Lilly, 1968). Turbulence homogenizes the cloud-containing layer, and frequently couples this layer to the surface source of moisture that maintains the cloud layer (Bretherton and Wyant, 1997). Turbulence also controls the development of mesoscale organization (Jonker et al., 1999; de Roode et al., 2004). Latent heating in the upward branches of the

convective elements and evaporation in downdrafts provides an additional source of turbulence that strengthens the convection. While various mechanisms have been proposed to describe how aerosols affect clouds and precipitation (Solomon, 2007), the most crucial set of the mechanism is AIE, which consists of the cloud albedo effect and lifetime effect.

The majority of other aerosol effects on clouds originate from first AIE: the decrease in cloud droplet size with increasing aerosol number concentration (N_a) for a fixed liquid water path (LWP) (Twomey, 1977). Cloud albedo is enhanced in such a cloud because numerous smaller cloud drops increase the total scattering cross section and thus reflect more solar radiation (Twomey, 1977). This effect has been supported by ample evidence from satellite remote sensing (Wetzel and Stowe, 1999; Nakajima et al., 2001; Liu, 2003) and ground or in situ observations (Feingold et al., 2003; Penner et al., 2004; Sena et al., 2016). We can quantitatively describe the AIE as the sensitivity of the cloud albedo (α) to changes in activated cloud droplet number concentration (N_d) as follow (Rosenfeld et al., 2013):

$$\frac{d\alpha}{dN_d} = \left(\frac{\partial\alpha}{\partial N_d}\right)_c + \sum_i \left(\frac{\partial\alpha}{\partial C_i}\right) \left(\frac{\partial C_i}{\partial N_d}\right) \quad (1)$$

where C_i is defined as cloud macrophysical properties (e.g., liquid water path, cloud thickness, cloud cover). The first term on the right-hand side (RHS) of Equation 1 is referred as Twomey effect or the first AIE, which represents the change in albedo caused only by changes in cloud microphysics, with the cloud macrophysical properties held constant. The second term on the RHS represents the changes in albedo associated with aerosol-induced changes in cloud macrophysical properties. Equation (1) is very general

since C_i can represent any changes in system induced by aerosol. In real clouds, changes in aerosols rarely affect only N_d without changing cloud macrophysical properties such as cloud morphology and LWP. Therefore, it is necessary to study cloud microphysics and macrophysics together to investigate the aerosol impacts.

Cloud macrophysical responses to aerosols are more challenging to understand than the purely microphysical effect. These changes induce macrophysical responses in turbulent dynamics, entrainment rate, and even mesoscale reorganization. However, many of these processes still remain poorly understood (Wood, 2012). The magnitude and even the sign of the responses of the cloud are not uniform. They appear to depend upon cloud type and meteorological regime. This requires the study of aerosol-cloud interactions across different background conditions.

3 Current challenges and uncertainties in studying aerosol-cloud interactions

Some processes by which aerosols can modulate clouds have been summarized in previous sections. Although aerosol-cloud interactions can sometimes be very apparent in small-scale observations, Stevens and Feingold (2009) caution that correlations between observed cloud and aerosol properties cannot always be used to identify cause and effect. It might be necessary to also consider intrinsic buffering mechanisms in the cloud-aerosol system that may modulate or counteract the traditional cloud-aerosol effects (Feingold et al., 2010) as well as to consider the impact of the observational scale (McComiskey and Feingold, 2012). Moreover, the different meteorological contexts need to be taken into account (Loeb and Schuster, 2008) since the aerosol influence may depend on the

meteorological regime. Besides the challenges mentioned above, to measure these components and disentangle them is difficult due to many existing limitations.

3.1 Field experiment limitations

Data from field experiments are useful to understand aerosol-cloud interactions at the process scale. However, field experiment data also have their own limitations. Foremost is that these studies are relatively rare and usually cannot provide an adequate statistical sample size to show the aerosol signal from the noise of the natural variability of the system. For example, to study a convective cloud system, many parameters can influence the system, such as aerosols, thermodynamic conditions, winds, the stage of the system lifecycle, etc. To isolate the aerosol effect, a large statistical database is required. Secondly, each field experiment instrument has some limitations, and there is also operator error. Instruments may disturb the particles before measuring them, especially when measuring cloud hydrometeors. For example, large droplets can be shattered on the inlets and tips of cloud particle probes, which produces copious small particles that can be mistakenly measured as real particles (Lawson, 2011). Finally, aircraft measurements of convective clouds are limited by safety concerns of the aircraft penetrating an area of strong updrafts and downdrafts, or limited by altitude restrictions on unpressurized aircraft. Ground-based radar, lidar, and radiometers can avoid some of these issues, but are less mobile while the aircraft payloads containing these remote sensing instruments can better overcome these problems. Thus, field experiment data provide essential detailed information and can be used to calibrate the satellite and modeling results, but

should be used complementarily with satellite and modeling techniques to broaden their statistical base.

3.2 Satellite observation limitations

Despite more and more satellite data becoming available to study aerosol and cloud, there are many limitations to use these data. The biggest challenge is correctly retrieving aerosol and cloud properties from satellite observations, especially retrieving aerosol near clouds. The twilight zone near clouds (Koren et al., 2007; Charlson et al., 2007) is difficult to deal with since this region contains very small clouds and some cloud fragments as well as humidified aerosols (Koren et al., 2009). Some proposed major problems are 1) the hygroscopic growth of aerosols in the more humid near-cloud region; 2) three-dimensional radiative transfer effect from clouds, whereby the multiple scattering can illuminate the environment surrounding the cloud (Marshak et al., 2006; Várnai and Marshak, 2009). These two effects can enhance the measured clear-sky aerosol optical thickness without actually increasing the aerosol number concentration. Another problem comes from undetectable clouds which are usually very thin and small, this effect is referred to as “cloud contamination”.

In addition, retrieval of cloud properties from passive sensors (e.g., MODIS onboard the Terra and Aqua satellites) is restricted only to properties at the cloud top, and retrievals may sometimes be affected if a thick aerosol layer occurs above clouds. Active sensors have the advantage of measuring accurate vertical information (e.g., CALIOP onboard the CALIPSO satellite) and retrieving aerosol near clouds with minimal cloud-related

artifacts. However, the small spatial coverage of active sensors makes it difficult to achieve global coverage.

Another major challenge of using satellite data is to quantify the variability in cloud properties independent of large-scale meteorological forcing. Correlative studies identify associations between variables but do not distinguish between cause and effect. For example, large-scale convergence could increase cloudiness as well as concentrate aerosols, thus producing an apparent correlation between aerosol and cloud with no direct physical connection. Therefore, it is not easy to isolate the net aerosol effect on clouds in changing meteorological conditions. Different cloud types must be studied separately, and variations in meteorological parameters must be minimized. A typical way to avoid this problem is to analyze subsets of the data with similar meteorological conditions (Koren et al., 2005; Jiang et al., 2008; Koren et al., 2010; Small et al., 2011; Heiblum et al., 2012). Besides these challenges, the analysis scale is also a problem that one has to pay attention to when using remote sensing data (McComiskey and Feingold, 2012). The analysis scale has to be compatible with the scale of the process. Due to the limitations in retrieving cloud and aerosol properties simultaneously in the same location, the analysis of remote sensing data is usually based on large-scale grid boxes, much larger than the processes scale, which leads to the elimination of the higher resolution signal from the results. Therefore, the use of higher resolution remote sensing techniques can effectively overcome this problem.

4 Chapter overview

This body of work aims to contribute to an understanding of the indirect effect of aerosols on radiative forcing and the climate system, through its influence on cloud microphysics, macrophysics, and radiative properties against a varying background of meteorological conditions.

Chapter 2 focuses on aerosol-cloud interactions at the local-scale, in the trade cumulus cloud regime over the Northern Indian Ocean. High-resolution aircraft in situ data and ground-based remote sensing data collected during the Cloud Aerosol Radiative forcing Dynamics EXperiment (CARDEX) campaign were analyzed, aiming to obtain a comprehensive view of aerosol-cloud interactions in trade cumulus clouds. The cloud microphysics, macrophysics and radiative properties response to variations in the aerosol load were investigated.

In Chapter 3, the focus shifts to remote sensing measurements across a larger sampling area during the NASA Studies of Emissions and Atmospheric Composition, Clouds and Climate Coupling by Regional Surveys (SEAC⁴RS) campaign, which was carried out over North America (mostly centered over the southeastern US) from August to September 2013. A combination of high-resolution airborne remote sensing, spaceborne remote sensing, and meteorological reanalysis data has been applied to study the sensitivity of cloud properties to variations in the aerosol load under different environmental conditions.

After analyzing the local-scale aircraft in situ observations and large-scale remote sensing measurements to investigate the aerosol-cloud relationships, it is of great interest to

further explore the uncertainties in quantifying the aerosol-cloud interactions. In Chapter 4, uncertainties due to sampling scale and remote sensing retrieval artifacts when quantifying aerosol indirect effects on shallow warm clouds were investigated by utilizing remote sensing, in situ data and a radiative transfer model designed by the author. Remote sensing uncertainties due to aerosol humidification and 3-D radiative transfer effects were evaluated.

Reference

- Ackerman, A. S., Toon, O. B., Stevens, D. E., Heymsfield, A. J., Ramanathan, V., and Welton, E. J.: Reduction of tropical cloudiness by soot, *Science*, 288, 1042-1047 % @ 0036-8075, 2000.
- Albrecht, B. A.: Aerosols, cloud microphysics, and fractional cloudiness, *Science*, 245, 1227-1230 % @ 0036-8075, 1989.
- Andreae, M. O., Rosenfeld, D., Artaxo, P., Costa, A. A., Frank, G. P., Longo, K. M., and Silva-Dias, M. A. F.: Smoking rain clouds over the Amazon, *Science*, 303, 1337-1342 % @ 0036-8075, 2004.
- Boucher, O., Randall, D., Artaxo, P., Bretherton, C., Feingold, G., Forster, P., Kerminen, V. M., Kondo, Y., Liao, H., and Lohmann, U.: Clouds and aerosols, in: *Climate change 2013: The physical science basis. Contribution of working group I to the fifth assessment report of the intergovernmental panel on climate change*, Cambridge University Press, 571-657, 2013.
- Bretherton, C. S., and Wyant, M. C.: Moisture transport, lower-tropospheric stability, and decoupling of cloud-topped boundary layers, *Journal of the Atmospheric Sciences*, 54, 148-167 % @ 1520-0469, 1997.
- Charlson, R. J., and Heintzenberg, J.: *Aerosol forcing of climate*, Wiley New York, 1995.
- Charlson, R. J., Ackerman, A. S., Bender, F. A. M., Anderson, T. L., and Liu, Z.: On the climate forcing consequences of the albedo continuum between cloudy and clear air, *Tellus B*, 59, 715-727 % @ 1600-0889, 2007.
- de Roode, S. R., Duynkerke, P. G., and Jonker, H. J. J.: Large-Eddy Simulation: How Large is Large Enough?, *Journal of the Atmospheric Sciences*, 61, 403-421, 10.1175/1520-0469(2004)061<0403:lshlil>2.0.co;2, 2004.
- Dey, S., Di Girolamo, L., Zhao, G., Jones, A. L., and McFarquhar, G. M.: Satellite-observed relationships between aerosol and trade-wind cumulus cloud properties

- over the Indian Ocean, *Geophysical Research Letters*, 38, n/a-n/a, 10.1029/2010gl045588, 2011.
- Feingold, G., Eberhard, W. L., Veron, D. E., and Previdi, M.: First measurements of the Twomey indirect effect using ground-based remote sensors, *Geophysical Research Letters*, 30, n/a-n/a, 10.1029/2002gl016633, 2003.
- Feingold, G., Koren, I., Wang, H., Xue, H., and Brewer, W. A.: Precipitation-generated oscillations in open cellular cloud fields, *Nature*, 466, 849-852, 10.1038/nature09314, 2010.
- Goren, T., and Rosenfeld, D.: Satellite observations of ship emission induced transitions from broken to closed cell marine stratocumulus over large areas, *Journal of Geophysical Research: Atmospheres*, 117, n/a-n/a, 10.1029/2012jd017981, 2012.
- Goren, T., and Rosenfeld, D.: Decomposing aerosol cloud radiative effects into cloud cover, liquid water path and Twomey components in marine stratocumulus, *Atmospheric Research*, 138, 378-393, 10.1016/j.atmosres.2013.12.008, 2014.
- Goren, T., and Rosenfeld, D.: Extensive closed cell marine stratocumulus downwind of Europe-A large aerosol cloud mediated radiative effect or forcing?, *Journal of Geophysical Research: Atmospheres*, 120, 6098-6116, 10.1002/2015jd023176, 2015.
- Hansen, J., Sato, M., and Ruedy, R.: Radiative forcing and climate response, *Journal of Geophysical Research: Atmospheres*, 102, 6831-6864, 10.1029/96jd03436, 1997.
- Heiblum, R. H., Koren, I., and Altaratz, O.: New evidence of cloud invigoration from TRMM measurements of rain center of gravity, *Geophysical Research Letters*, 39, n/a-n/a, 10.1029/2012gl051158, 2012.
- Jiang, J. H., Su, H., Schoeberl, M. R., Massie, S. T., Colarco, P., Platnick, S., and Livesey, N. J.: Clean and polluted clouds: Relationships among pollution, ice clouds, and precipitation in South America, *Geophysical Research Letters*, 35, 10.1029/2008gl034631, 2008.

- Johnson, B. T., Shine, K. P., and Forster, P. M.: The semi-direct aerosol effect: Impact of absorbing aerosols on marine stratocumulus, *Quarterly Journal of the Royal Meteorological Society*, 130, 1407-1422, 10.1256/qj.03.61, 2004.
- Jonker, H. J. J., Duynkerke, P. G., and Cuijpers, J. W. M.: Mesoscale fluctuations in scalars generated by boundary layer convection, *Journal of the Atmospheric Sciences*, 56, 801-808 % @ 1520-0469, 1999.
- Kaufman, Y. J., and Koren, I.: Smoke and pollution aerosol effect on cloud cover, *Science*, 313, 655-658, 10.1126/science.1126232, 2006.
- Koren, I., Kaufman, Y. J., Remer, L. A., and Martins, J. V.: Measurement of the effect of Amazon smoke on inhibition of cloud formation, *Science*, 303, 1342-1345, 10.1126/science.1089424, 2004.
- Koren, I., Kaufman, Y. J., Rosenfeld, D., Remer, L. A., and Rudich, Y.: Aerosol invigoration and restructuring of Atlantic convective clouds, *Geophysical Research Letters*, 32, n/a-n/a, 10.1029/2005gl023187, 2005.
- Koren, I., Remer, L. A., Kaufman, Y. J., Rudich, Y., and Martins, J. V.: On the twilight zone between clouds and aerosols, *Geophysical Research Letters*, 34, n/a-n/a, 10.1029/2007gl029253, 2007.
- Koren, I., Feingold, G., Jiang, H., and Altaratz, O.: Aerosol effects on the inter-cloud region of a small cumulus cloud field, *Geophysical Research Letters*, 36, 10.1029/2009gl037424, 2009.
- Koren, I., Feingold, G., and Remer, L. A.: The invigoration of deep convective clouds over the Atlantic: aerosol effect, meteorology or retrieval artifact?, *Atmospheric Chemistry and Physics*, 10, 8855-8872, 10.5194/acp-10-8855-2010, 2010.
- Lawson, R. P.: Effects of ice particles shattering on the 2D-S probe, *Atmospheric Measurement Techniques*, 4, 1361-1381 % @ 1867-1381, 2011.
- Lilly, D. K.: Models of cloud-topped mixed layers under a strong inversion, *Quarterly Journal of the Royal Meteorological Society*, 94, 292-309 % @ 1477-1870X, 1968.

- Liu, G.: Retrieval of cloud droplet size from visible and microwave radiometric measurements during INDOEX: Implication to aerosols' indirect radiative effect, *Journal of Geophysical Research*, 108, 10.1029/2001jd001395, 2003.
- Loeb, N. G., and Schuster, G. L.: An observational study of the relationship between cloud, aerosol and meteorology in broken low-level cloud conditions, *Journal of Geophysical Research*, 113, 10.1029/2007jd009763, 2008.
- Lohmann, U., and Feichter, J.: Global indirect aerosol effects: a review, *Atmospheric Chemistry and Physics*, 5, 715-737 % @ 1680-7316, 2005.
- Marshak, A., Platnick, S., Várnai, T., Wen, G., and Cahalan, R. F.: Impact of three-dimensional radiative effects on satellite retrievals of cloud droplet sizes, *Journal of Geophysical Research*, 111, 10.1029/2005jd006686, 2006.
- McComiskey, A., and Feingold, G.: The scale problem in quantifying aerosol indirect effects, *Atmospheric Chemistry and Physics*, 12, 1031-1049, 10.5194/acp-12-1031-2012, 2012.
- Myhre, G., Shindell, D., Bréon, F. M., Collins, W., Fuglestedt, J., Huang, J., Koch, D., Lamarque, J. F., Lee, D., and Mendoza, B.: Anthropogenic and Natural Radiative Forcing. In: *Climate Change 2013: The Physical Science Basis. Contribution of Working Group 1 to the Fifth Assessment Report of the Intergovernmental Panel on Climate Change*, Table, 8, 714, 2013.
- Nakajima, T., Higurashi, A., Kawamoto, K., and Penner, J. E.: A possible correlation between satellite-derived cloud and aerosol microphysical parameters, *Geophysical Research Letters*, 28, 1171-1174, 10.1029/2000gl012186, 2001.
- Penner, J. E., Dong, X., and Chen, Y.: Observational evidence of a change in radiative forcing due to the indirect aerosol effect, *Nature*, 427, 231-234 % @ 0028-0836, 2004.
- Pistone, K., Praveen, P. S., Thomas, R. M., Ramanathan, V., Wilcox, E. M., and Bender, F. A. M.: Observed correlations between aerosol and cloud properties in an Indian

- Ocean trade cumulus regime, *Atmospheric Chemistry and Physics*, 16, 5203-5227, 10.5194/acp-16-5203-2016, 2016.
- Ramanathan, V., Crutzen, P. J., Kiehl, J. T., and Rosenfeld, D.: Aerosols, climate, and the hydrological cycle, *Science*, 294, 2119-2124, 10.1126/science.1064034, 2001.
- Roberts, G. C., Ramana, M. V., Corrigan, C., Kim, D., and Ramanathan, V.: Simultaneous observations of aerosol-cloud-albedo interactions with three stacked unmanned aerial vehicles, *Proceedings of the National Academy of Sciences of the United States of America*, 105, 7370-7375, 10.1073/pnas.0710308105, 2008.
- Rosenfeld, D., Lahav, R., Khain, A., and Pinsky, M.: The role of sea spray in cleansing air pollution over ocean via cloud processes, *Science*, 297, 1667-1670 % @ 0036-8075, 2002.
- Rosenfeld, D., Lohmann, U., Raga, G. B., O'Dowd, C. D., Kulmala, M., Fuzzi, S., Reissell, A., and Andreae, M. O.: Flood or drought: how do aerosols affect precipitation?, *Science*, 321, 1309-1313, 10.1126/science.1160606, 2008.
- Rosenfeld, D., Wood, R., Donner, L. J., and Sherwood, S. C.: Aerosol cloud-mediated radiative forcing: highly uncertain and opposite effects from shallow and deep clouds, in: *Climate Science for Serving Society*, Springer, 105-149 % @ 9400766912, 2013.
- Rosenfeld, D., Andreae, M. O., Asmi, A., Chin, M., de Leeuw, G., Donovan, D. P., Kahn, R., Kinne, S., Kivekäs, N., Kulmala, M., Lau, W., Schmidt, K. S., Suni, T., Wagner, T., Wild, M., and Quaas, J.: Global observations of aerosol-cloud-precipitation-climate interactions, *Reviews of Geophysics*, 52, 750-808, 10.1002/2013rg000441, 2014.
- Seinfeld, J. H., and Pandis, S. N.: *Atmospheric chemistry and physics: from air pollution to climate change*, John Wiley & Sons, 2012.
- Sena, E. T., McComiskey, A., and Feingold, G.: A long-term study of aerosol–cloud interactions and their radiative effect at a mid latitude

- continental site using ground-based measurements, *Atmospheric Chemistry and Physics Discussions*, 1-36, 10.5194/acp-2016-271, 2016.
- Small, J. D., Jiang, J. H., Su, H., and Zhai, C.: Relationship between aerosol and cloud fraction over Australia, *Geophysical Research Letters*, 38, n/a-n/a, 10.1029/2011gl049404, 2011.
- Solomon, S.: *Climate change 2007-the physical science basis: Working group I contribution to the fourth assessment report of the IPCC*, Cambridge University Press, 2007.
- Stevens, B., and Feingold, G.: Untangling aerosol effects on clouds and precipitation in a buffered system, *Nature*, 461, 607-613, 10.1038/nature08281, 2009.
- Twohy, C. H.: Evaluation of the aerosol indirect effect in marine stratocumulus clouds: Droplet number, size, liquid water path, and radiative impact, *Journal of Geophysical Research*, 110, 10.1029/2004jd005116, 2005.
- Twomey, S.: Pollution and the planetary albedo, *Atmospheric Environment* (1967), 8, 1251-1256 % @ 0004-6981, 1974.
- Twomey, S.: The influence of pollution on the shortwave albedo of clouds, *Journal of the Atmospheric Sciences*, 34, 1149-1152 % @ 1520-0469, 1977.
- Várnai, T., and Marshak, A.: MODIS observations of enhanced clear sky reflectance near clouds, *Geophysical Research Letters*, 36, 10.1029/2008gl037089, 2009.
- Wetzel, M. A., and Stowe, L. L.: Satellite-observed patterns in stratus microphysics, aerosol optical thickness, and shortwave radiative forcing, *Journal of Geophysical Research: Atmospheres*, 104, 31287-31299, 10.1029/1999jd900922, 1999.
- Wilcox, E. M.: Stratocumulus cloud thickening beneath layers of absorbing smoke aerosol, *Atmospheric Chemistry and Physics*, 10, 11769-11777, 10.5194/acp-10-11769-2010, 2010.

- Wood, R.: Cancellation of Aerosol Indirect Effects in Marine Stratocumulus through Cloud Thinning, *Journal of the Atmospheric Sciences*, 64, 2657-2669, 10.1175/jas3942.1, 2007.
- Wood, R.: Stratocumulus Clouds, *Monthly Weather Review*, 140, 2373-2423, 10.1175/mwr-d-11-00121.1, 2012.
- Xue, H., and Feingold, G.: Large-eddy simulations of trade wind cumuli: Investigation of aerosol indirect effects, *Journal of the Atmospheric Sciences*, 63, 1605-1622 % @ 1520-0469, 2006.
- Yuan, T., Remer, L. A., and Yu, H.: Microphysical, macrophysical and radiative signatures of volcanic aerosols in trade wind cumulus observed by the A-Train, *Atmospheric Chemistry and Physics*, 11, 7119-7132, 10.5194/acp-11-7119-2011, 2011.

Chapter 2

Aerosol effects on trade cumulus cloud over the Northern Indian Ocean during CARDEX 2012

Lan Gao^{1, 2}, Eric M. Wilcox¹, Puppala S. Praveen³, Kristina Pistone^{4, 5}, Frida A.-M. Bender⁶, Yunpeng Shan^{1, 2, 7}

¹Desert Research Institute, Reno, 89512, USA

²Atmospheric Sciences Graduate Program, University of Nevada Reno, 89557, USA

³International Centre for Integrated Mountain Development, Kathmandu, 44700, Nepal

⁴Bay Area Environmental Research Institute, Moffett Field, CA, 94035, USA

⁵NASA Ames Research Center, Moffett Field, CA, 94035, USA

⁶Department of Meteorology, Stockholm University, Stockholm, 10691, Sweden

⁷Department of Atmospheric Sciences, University of Wyoming, Laramie, WY, 82071, USA

Correspondence to: Eric M. Wilcox (Eric.Wilcox@dri.edu)

To be submitted to: Atmospheric Chemistry and Physics

Abstract. In this study, we examined how pollution from the Indian subcontinent co-varies with the properties of trade cumulus clouds over the northern Indian Ocean. In situ measurements from three Autonomous Unmanned Aerial Vehicles (UAVs) and ground-based observational data from the Maldives Climate Observatory on Hanimaadhoo (MCOH) during the Cloud Aerosol Radiative forcing Dynamics EXperiment (CARDEX) campaign in February and March 2012 were analyzed. These data were used together with satellite remote sensing data to investigate the microphysical, macrophysical, and radiative properties of trade cumulus clouds in this region. Results reveal that more polluted clouds were substantially deeper and narrower with greater cloud liquid water path (LWP) than less polluted clouds. The observed deeper clouds are mainly due to the warmer, more humid and shallower boundary layer (BL), a finding which can be corroborated with the observed thicker saturated layer in Case H as well as the lower cloud base and slightly higher cloud top height. The narrower clouds formed in Case H were caused by the intensified cloud edge evaporation effect, as a result of more and smaller cloud droplets induced by increasing aerosol concentration. The deeper and narrower clouds embedded in a high concentration of absorbing aerosols over this region contribute to a brighter atmosphere as viewed from space compared to cleaner conditions. As a consequence, the regional negative solar shortwave forcing at the top of the atmosphere due to aerosols increases in magnitude (i.e., greater cooling of regional climate) with increasing aerosol optical depth more than is contributed by just the direct effect of aerosols alone. Attempts were tried to separate the effects from meteorology, however, it's difficult to constrain meteorological conditions. A linear regression analysis between meteorological parameters and aerosol-cloud properties was performed and

results did not suggest a strong dynamical effect. Further modelling studies are needed to better understand the causality.

1 Introduction

Boundary layer (BL) clouds, especially in shallow maritime cloud systems, are the dominant atmospheric regulators of solar radiant flux and have been identified as a major source of uncertainty in climate sensitivity and climate change (Albrecht, 1989; Pincus and Baker, 1994; Bony, 2005; Medeiros et al., 2008). The clouds in such systems have an albedo several times larger than that of the ocean surface. Because of their shallowness, these clouds radiate energy at an effective temperature similar to that of the surface. Hence, shallow maritime clouds effectively modulate the net solar radiation entering the climate system, with little or no compensating effects on the budget of outgoing terrestrial radiation (Hartmann and Doelling, 1991). Besides their higher albedo, shallow clouds (particularly trade cumulus clouds) are also especially effective at moving moisture away from the surface, thus enhancing surface evaporation and moistening the lower troposphere (Tiedtke, 1989). Understanding how shallow clouds respond to climate change is critical to reducing current high uncertainties in climate forcing (Bony, 2005; Stephens, 2005; Boucher et al., 2013). However, quantifying the associated mechanisms and impacts is extremely challenging since clouds interact with aerosols through various mechanisms leading to a variety of impacts on climate forcing (Stocker et al., 2013; Rosenfeld et al., 2014a; Rosenfeld et al., 2014b).

Aerosol interactions with clouds are often described as resulting from three primary mechanisms: 1) serving as the cloud condensation nuclei (CCN) or ice nuclei (IN) for cloud droplets and ice particles, thereby altering the cloud albedo (first indirect effect) (Twomey, 1974); 2) suppressing precipitation and prolonging the cloud lifetime (second

indirect effect) (Albrecht, 1989); 3) absorbing sunlight and heating the cloud layer to burn off the clouds (semi-direct effect) (Hansen et al., 1997). Untangling the multiple cloud responses that occur as a result of aerosol perturbations is particularly difficult. For example, one can observe the Twomey effect as a result of aerosol loading when other cloud parameters, such as buoyancy or humidity are unchanged. However, other cloud parameters may not remain constant when clouds are subjected to increasing CCN concentrations. Aerosols can also alter the subsequent fate of condensed water and can drive circulations that alter the formation of clouds. Smaller droplets may cause a cloud to dissipate either more quickly by enhancing evaporative entrainment (Jiang et al., 2006; Small et al., 2009) or more slowly by decreasing the rate at which a cloud is depleted by precipitation (Albrecht, 1989). Opposing signs for cloud changes are often recorded from these aerosol effects. Aerosol-cloud interactions have been shown to be highly dependent on the regime in which they are studied (e.g., aerosol type, cloud type, meteorological condition) and the scale at which research has been done (e.g., individual cloud element, cloud system, regional/global scale) (Stevens and Feingold, 2009; McComiskey and Feingold, 2012; Bender et al., 2016). Thus aerosol, dynamics, and cloud properties are interconnected, and to date, their joint effects are not fully understood. To better understand this complexity requires studies of all types of clouds under different background conditions (e.g., aerosol and meteorological condition).

The northern Indian Ocean is considered a good natural laboratory to study aerosol-cloud-radiation interactions. This region is frequently covered by trade cumulus cloud, and the meteorological conditions show a particularly strong seasonal variation following the migration of the Intertropical Convergence Zone (ITCZ). During the winter monsoon

period, the low-level flow over the northern Indian Ocean mostly comes from the north and northeast following the ITCZ, which is south of the equator. Due to the unique location which is close to the highly polluted Indian subcontinent, air masses with a high concentration of anthropogenic aerosol are frequently transported to this area following the prevailing wind. The cumulus clouds over the Indian Ocean, coupled with the effects of injected aerosol, have a large potential to affect the regional and global climate forcing. Several major field campaigns have been performed to explore the role of anthropogenic aerosols and their interactions with clouds and radiation in this region (e.g., the Indian Ocean Experiment (INDOEX) in 1999, the Maldives Autonomous Unmanned Aerial Vehicle Campaign (MAC) in 2006). Previous studies have identified an elevated absorbing aerosol layer consisting largely of, black carbon (BC), above the marine boundary layer in the northern part of Indian Ocean and revealed its role in influencing atmospheric radiation and clouds. Main results from previous campaigns can be found from a series of papers (Ramanathan et al., 2001; Heymsfield and McFarquhar, 2001; Ramanathan et al., 2007; Roberts et al., 2008; Corrigan et al., 2008; Satheesh et al., 2008). The present study is based on the field campaign Cloud Aerosol Radiative forcing Dynamics EXperiment (CARDEX), which was conducted in the vicinity of the Maldives Climate Observatory in Hanimaadhoo (MCOH) from February 16 to March 30, 2012 and is described in Ramanathan et al. (2011). Some related results from CARDEX can be found in recent papers (Bosch et al., 2014; Höpner et al., 2016; Pistone et al., 2016; Wilcox et al., 2016). The aerosol vertical distributions, aerosol-cloud LWP and aerosol-turbulence relationships were discussed in those papers using CARDEX data. Here we expand on this work by exploring how cloud microphysics and macrophysics varies with

aerosol amount and what these results, together with the previous work on LWP and turbulence, mean for shortwave radiative fluxes in the region.

The focus of this study is on the response of cloud microphysics and macrophysics to aerosol during CARDEX, utilizing a combination of tower in-situ observations, lightweight unmanned aerial vehicles (UAVs), and ground- and satellite-based remote sensing measurements. Data and methods are described in Sect. 2. Variations of cloud micro- and macrophysical properties correlating with variations in the aerosol loading are presented and discussed in Sect. 3. The conclusions are in Sect. 4.

2 Data and methods

2.1 Airborne measurements from UAV

The central component of CARDEX was the deployment of lightweight UAVs to measure aerosol, cloud and radiation properties. There were three UAVs flown during CARDEX each with one of the aerosol/radiation, water vapor flux or cloud microphysics payloads. All UAVs were equipped with differential GPS (DGPS) capability that precisely controls their flight path and a 100 Hz data logging system that collects the high-resolution data. More details regarding the instruments used in CARDEX and the detailed experimental design can be found in Corrigan et al. (2008) and Ramanathan et al. (2011). During CARDEX, eighteen aerosol UAV flights and fifteen cloud UAV flights were performed from an airport located around 3 km southwest of MCOH. The date and time for each flight can be found in Table 2 of Pistone et al. (2016).

The aerosol UAV was equipped with a TSI condensation particle counter (CPC) that measures the total particle number concentration (N_a) for particles with diameters larger

than 10 nm. The accuracy of the CPC is within $\pm 10\%$. The cloud UAV was equipped with a cloud droplet probe that gives the cloud droplet number concentration (N_d), effective radius (R_e), liquid water content (LWC) and cloud droplet size distribution (CDS) in the diameter range of 1-50 μm with 40 consecutive size bins. In addition to aerosol and cloud properties, general meteorological parameters such as temperature (T), relative humidity (RH) and pressure (P) were also measured from all of the UAVs with a vertical resolution of 1-4 m (Table.1). A more detailed description of UAV payload can be found in Ramanathan et al. (2007), Ramana et al. (2007), Corrigan et al. (2008), Roberts et al. (2008), and Thomas et al. (2012). The typical flight patterns of aerosol and cloud UAVs are shown in Fig.1. The cloud data were selected only when the cloud UAV horizontally penetrated the cloud base (CB) level. The CB height was consecutively retrieved from a mini Micro Pulse Lidar (MPL) in the surface station and averaged into hourly mean to constrain the UAV measurements near CB. More details about the MPL operation and algorithm can be found in Höpner et al. (2016). A cloud point was defined as the measured cloud droplet number concentration is greater than 50 cm^{-3} and cloud liquid water content is greater than 0.01 g m^{-3} (McFarquhar and Heymsfield, 2001), at least four consecutive cloudy points can be considered as a cloud penetration. For each cloud penetration, take an average of the middle two points to represent the cloud center, and the average of the first and last points is treated as the cloud edge. The selected cloud penetration must also meet the following two criteria: 1) the UAV penetration altitude was within $\pm 100 \text{ m}$ of the reference CB height retrieved from MPL; The UAV flew in vicinity of the MCOH to sample clouds. Therefore, the MPL retrieved CB heights were average into every 15-minute to represent the CB in that time range and compared with

UAV penetration altitude; 2) the consecutive cloud penetration altitudes are less than 1 m apart. By doing this, we could constrain cloud microphysical analysis on the CB portion, reducing the variations of cloud droplet growth with height, since N_a and R_e are generally a function of depth from CB (Freud and Rosenfeld, 2012).

2.2 Ground measurements at the MCOH

The MCOH station, located at 6.78° N, 73.18° E on the island of Hanimaadhoo, Maldives, has a long-term history of meteorology and climate observation since 2004 (Ramana and Ramanathan, 2006). Continuous measurements of aerosol properties, solar radiation, and meteorological parameters have regularly been performed at MCOH. Selected instruments and data are listed in Table 1. The instruments for measuring meteorological parameters were mounted on the top of a 15 m tower to avoid the effects from the surrounding vegetation canopy and local aerosol sources from the island residents. The aerosol number concentration was measured by a CPC feeding from an inlet at the top of the tower. An impactor was installed at the top of the inlet pipe to collect only particles with diameters less than 10 μm . The collection efficiency is better than 90% for particles with diameters equal to 10 μm and as high as 98% for particles with diameters less than 5 μm (Corrigan et al., 2006). Following previous papers (Wilcox et al., 2016; Pistone et al., 2016), here we define two pollution conditions based on surface N_a : the low polluted case ($N_a < 1000 \text{ cm}^{-3}$, Case L) and high polluted case ($N_a > 1500 \text{ cm}^{-3}$, Case H). Then we matched the ± 2 hourly averaged surface N_a around the flight time to consider the aerosols that most likely influenced the cloud formation.

Some other aerosol metrics used to validate the surface N_a , like aerosol optical depth (AOD), can be found in Table 1. Figure 2a shows the time series of surface N_a , AOD at 550 nm wavelength (AOD_{550}) from AErosol RObotic NETwork (AERONET) sun photometer (Holben et al., 1998) which was determined by interpolating (linearly in the natural logarithm of wavelength) the measurements (V2 products) at 470, 675, and 870 μm , and AOD_{550} from MODerate resolution Imaging Spectroradiometer (MODIS) during CARDEX. Comparisons indicate good agreement among the three aerosol metrics. The linear regression shows that collocated AOD from MODIS and AERONET have good correlation ($R^2=0.81$) during CARDEX. To investigate aerosol-cloud interactions, the aerosols that exist below cloud base and at cloud layer are crucial due to role in nucleating cloud droplets. In a well-mixed boundary layer, the aerosol concentration will be reasonably constant with altitude, and the surface N_a can be used to represent the amount of aerosol at cloud base. Figure 2b shows the comparison between the aerosol number concentration measured at the tower and from the UAV. Only UAV sampled boundary layer N_a is included in this scatter plot. The correlation coefficient R^2 was 0.94 at the 95% confidence level, so that it is reasonable to use surface N_a to represent the aerosol at cloud layer.

The total column precipitable water vapor (PWV) and cloud liquid water path (LWP) were retrieved from a microwave radiometer (MWR) installed at the MCOH. The retrieval algorithm and validation of PWV from MWR can be found in Sect. 3.3.2 in Pistone (2014). The daily-averaged PWV conditions for the entire CARDEX period are given in Table 1 from Pistone et al. (2016). The cloud LWP used in this study is the average-peak value for each cloud event (see Fig. 3 and Appendix A1 in Pistone et al.

(2016) for details), which is a meaningful parameter to describe the cloud LWP when accounting for instrument noise and variability within the cloud (Warner, 1955).

2.3 Spaceborne measurements from satellite

Two types of satellite data for 91 days between 1 Jan and 31-Mar 2012 were used: MODIS/Aqua Level 2 Collection 6 products and Clouds and the Earth's Radiant Energy System (CERES) Level 3 products (Wielicki et al., 1996) (listed in Table 1). The study area for satellite data analysis is a 10° by 10° box ranging from 0° N to 10° N and 65° E to 75° E, which entirely covers the UAV sampled area and is chosen to scale results from a local measurement to a regional perspective. The variables used from MODIS product were: 1) AOD at 550 nm, serving as a proxy for CCN concentrations (Andreae, 2009); 2) cloud top pressure (CTP)/cloud top temperature (CTT), excluding data when CTP was less than 750 hPa and CTT was less than 273 K in order only to consider the low-level liquid warm clouds.

The CERES data used in this study are the SYN1deg product which gives the 3-hourly regional observed TOA fluxes and MODIS-derived AOD at 550 nm. The TOA shortwave (SW) cloud forcing can be calculated using these data. The TOA SW forcing is defined as the difference between the "clean-clear" flux and the flux for diurnal-mean solar insolation for the date and latitude of the observation. The "clean-clear" flux is constructed as follows: first convert the flux to an albedo using an estimate of the downward flux at TOA for the appropriate time, date and latitude. Second, the albedos are sorted into 5-degree bins of solar zenith angle since the albedo depends on the zenith angle. Finally, an average is taken of the 20 lowest values of albedo in each solar zenith

angle bin. This is then an estimate of the lowest possible albedo for each solar zenith bin. To evaluate the cloud forcing for a single pixel, first the SW flux sample is converted into an instantaneous albedo. Then that value is subtracted from the "clean-clear" albedo appropriate for the solar zenith angle of the observation, and the result is multiplied by the diurnal-mean solar insolation at the TOA for the date and latitude of the observation.

3 Results and discussion

3.1 Background conditions during CARDEX

This section is largely a review of Pistone et al. (2016), Wilcox et al. (2016) and Höpner et al. (2016) to understand the meteorological and aerosol conditions during CARDEX before investigating the potential aerosol effects on the cloud. During CARDEX, the total-column PWV had high variability ranging from 20 to 60 kg m⁻². Pistone et al. (2016) defined two distinct atmospheric water vapor regimes by using the criterion PWV < 40 kg m⁻² (dry) and PWV > 40 kg m⁻² (wet), and used this to filter the data to control for natural meteorological variability. The two climatologies result in different populations of cloud formation: clouds in “dry” conditions tend to be capped by an inversion, whereas the clouds in “wet” conditions show more unconstrained development due to more humid upper-layer air. Besides the cloud, meteorological parameters during wet days also show greater variation (Sect. 2 in Pistone et al. (2016)). On average, higher wind speed and lower surface pressure can be found in dry cases. Wet cases correspond to greater surface humidity and variability in cloud LWP. As a first step to minimize and constrain the impact of dynamics and meteorological variation on clouds, here we only analyzed the cloud properties sampled during the dry days.

Two pollution conditions are defined as discussed in Sect. 2.2. The Case H corresponds to warmer T and higher RH in the BL. The warmer T has previously been attributed to heating by absorbing aerosols (Ramanathan et al., 2007), while Wilcox et al., (2016) showed that the higher RH may be induced by the presence of absorbing aerosols which can suppress turbulent mixing in the BL. Pistone et al (2016) showed that the high temperature anomaly is present along with the elevated aerosol plume as it leaves the subcontinent, whereas the high humidity condition is seen to develop with time as the air mass is advected south. The theory suggests that clouds are likely to grow taller in Case H because greater humidity provides more buoyancy. To test and further investigate possible mechanisms that aerosol may affect cloud under these background conditions, here we examine the variations of cloud microphysical, macrophysical and radiative properties associated with variations in aerosol loading.

3.2 Aerosol effects on cloud microphysics

The cloud microphysical properties, as summarized in Table 2 (CARDEX column) and shown in Fig. 3, were obtained from the cloud droplet probe onboard the cloud microphysics UAV. After applying the two criteria described in Sect. 2.1, three days of Case L flights with 147 sampled clouds and three days of Case H flights with 229 sampled clouds were analyzed. The probability density function (PDF) of N_d and R_e from Case L and Case H are presented in panels a and b of Fig. 3. The mean aerosol particle concentration in Case H was $N_a=1753 \pm 259 \text{ cm}^{-3}$, which is more than twice that of Case L with $N_a=882 \pm 207 \text{ cm}^{-3}$. For Case L, the PDF of N_d shows a narrow range of maximum values appearing between 200 and 400 cm^{-3} . The Case H, conversely, has a

broader PDF with two peaks in the range of 200-400 cm^{-3} and 1000-1200 cm^{-3} . The average N_d in Case H is 607 cm^{-3} which is roughly twice the value in Case L (295 cm^{-3}). The R_e for Case L shows a broader range and higher values with most observations varying between 5 and 6.5 μm . For the Case H, the PDF is narrower with most of the values ranging between 4 and 5.5 μm . The average R_e in Case H is 4.53 μm , which is 1 μm lower than the value (5.54 μm) in Case L. Overall, Case H corresponds to more cloud droplets and smaller effective radius, which is consistent with Twomey effect. For a constant amount of cloud liquid water, more aerosols can nucleate more cloud droplets and reduce the droplet size. Increases in total droplet surface area thus increase the cloud albedo, producing a negative indirect radiative forcing.

The cloud droplet size distributions are shown in panel c and d of Fig. 3 where the cloud center and edge are compared in the two cases. Case H shows a bimodal distribution of cloud droplets with two peaks centered at 8 μm and 11 μm , while Case L shows a monomodal distribution with a peak around 11 μm , indicating the possibility that there were different types of aerosols in this region since aerosol composition may influence the cloud droplet size distribution (James, 1974). The composition of the aerosol may influence cloud properties, but these effects are beyond the scope of this study. In the smaller size bins (less than 10 μm), Case H has greater N_d than Case L, but the opposite appears to be the case in the larger size bins (larger than 12 μm). A similar CDS can be found in the center of the cloud as at cloud edge but there is a great difference in magnitude. There is larger number of cloud droplets in the cloud center than the cloud edge, and the difference in average N_d between Case H and L for cloud center is greater compared to cloud edge. The cloud center has a broader range of cloud drop sizes

compared to the cloud edge. The PDF of N_d , R_e and the CDS for both cloud center and edge all show that Case H is likely to have many more droplets with smaller diameters but fewer droplets with larger diameters. The PDF of cloud LWC shows approximately the same distribution for both cases (panel e of Fig. 3) but the mean LWC in Case H is slightly higher than in Case L. The observed variations in N_d and R_e may largely result from the differences in the aerosol conditions under the two cases and not from the variations in the LWC. The differences in the cloud microphysical properties may also be influenced by other factors, e.g., cloud top- and side- entrainment and vertical velocity; however, those variables were not directly measured during CARDEX and are excluded from this analysis. Aerosol can affect cloud by changing cloud microphysics, and more numerous smaller cloud droplets in the high aerosol case may subsequently influence cloud macrophysics. The influences of aerosol on cloud macrophysics and their connection with variations in cloud microphysics are discussed in more details in Sect. 3.3.

Comparisons of the CARDEX results with results from two previous field campaigns over the same region are also shown in Table 2 and Fig. 4. Overall, CARDEX was the most polluted campaign among the three studies, and the mean particle number concentration through the whole campaign was as large as $1520 \pm 740 \text{ cm}^{-3}$. The mean particle concentrations during MAC and INDOEX were $1215 \pm 350 \text{ cm}^{-3}$ and $1194 \pm 635 \text{ cm}^{-3}$, respectively (de Reus et al., 2001; Höpner et al., 2016). Data presented in Table 2 are partitioned into different pollution levels based on aerosol concentrations. Differences in defining the pollution levels among those three campaigns should be noted (see caption of Table 2). Figure 4 shows the relationships between N_a and cloud properties for

the three campaigns. Clear relationships can be found from panels a and b of Fig. 4. As N_a increases, N_d increases while R_e decreases. The LWC varies between the campaigns, but does not co-vary with N_a , but for each campaign, the mean value slightly increases with increasing N_a . This may not be the dominant factor influencing the observed N_d and R_e differences with changing N_a . The cloud width (defined by the consecutive cloudy points sampled from each cloud penetration) decreases as aerosol loading increases for both CARDEX and MAC, but there is no obvious difference in INDOEX.

3.3 Aerosol effects on cloud macrophysics

The aerosol loading does not only affect the cloud microphysics but is also hypothesized to influence the macrophysics and morphology of clouds. To fully understand aerosol effects on cloud, one has to consider microphysics and macrophysics together since they are connected and can influence one another. Cloud macrophysics usually refers to cloud liquid water path, cloud fraction or cloud optical thickness, while morphology refers to width or depth, all of which can individually and jointly affect the cloud radiative properties. The cloud macrophysical variables are generally controlled by both cloud-scale dynamics and the thermodynamics of the ambient air; for fair weather cumulus, a small change in microphysics may cause a substantial change in macrophysics.

Figure 5 shows the cloud width as a function of average peak cloud LWP. The estimated cloud width was calculated using the number of cloudy points in each cloud penetration multiplied by the mean UAV speed. The cloud width and average peak LWP were both averaged to a daily mean. Note that the cloud UAV was only flown for 1-2 hours each day, so here, the daily mean is actually the mean value during each flight. Although

substantial variations in sampled LWP and cloud width are apparent, two relationships emerge from Fig. 5: 1) cloud LWP increases as aerosol concentration increases; 2) cloud width decreases as aerosol concentration increases. The cloud LWPs were generally greater on more polluted days compared with those on less polluted days, as described in Pistone et al. (2016), which is consistent with the result from Fig. 6 right panel. The observed positive relationship between cloud LWP and aerosol loading indicates that thicker clouds are likely to develop under more polluted conditions. As discussed in Wilcox et al. (2016), an observed reduction in BL turbulent kinetic energy in Case H decreases the entrainment of air across the temperature inversion at the top of the BL, which favors a lower surface mixed layer top. The reduced turbulent mixing leads to greater relative humidity in the surface mixed layer because of weakened mixing of moist air up through the interface and weakened mixing of dry tropospheric air down into the mixed layer. As a result, clouds in Case H form in a thicker saturated layer and may penetrate above the inversion since greater humidity provides additional buoyancy. To further investigate the cloud depth, an analysis of cloud top height (CTH) using MODIS Level 2 cloud product and cloud base height using MPL retrieval are shown in Fig. 7. As AOD increases, the CTHs were not found to be statistically different while the cloud base height (CBH) systematically decreases. Considering the fact that the CBHs are lower in Case H and CTHs are generally the same, more polluted clouds should be substantially deeper. This result independently corroborates the results determined from UAV vertical profiles in Pistone et al. (2016).

Besides cloud depth, cloud horizontal width also shows differences between the two cases. In Case L the cloud widths were mostly distributed between 190-360 m (Fig. 5)

while in Case H the cloud widths were mostly between 150-270 m. To test the significant of difference between cloud width in Case L (mean: 8.35, standard error: 0.4) and Case H (mean: 6.86, standard error: 0.2), a Student's t-test was performed between the two populations and results indicated a statistically significant difference between the two with $t\text{-value}=3.06$, $p\text{-value}<0.05$. Hence, more polluted clouds appear to be substantially narrower than less polluted clouds. As an independent means to estimate the cloud width, an estimate derived from the vertically pointing surface MWR is shown (Fig. 6 right panel). Here the cloud width was estimated as the number of consecutive cloudy points measured by the MWR. Although there is substantial variability in both estimates of cloud width, Case H corresponds to less consecutive cloudy points indicating narrower clouds. By applying the average UAV speed (30 ms^{-1}), wind speed (5 ms^{-1}), sampling frequency (1s for UAV and ~ 20 s for MWR) and the difference in consecutive cloudy points sampled for the two cases from both UAV (3-4 points) and MWR (1-2 points), we can simply estimate the difference in cloud width in both Case H and L, which are 90-120 m and 100-200 m derived from UAV and MWR, respectively. These two independent means of estimating cloud width both have some significant uncertainties. Although the absolute values of cloud width do not necessarily agree between the two because of their uncertainties (likely dominated by uncertainty in the speed of clouds moving past the MWR), both methods indicate that the more polluted cloud are narrower. The observed decrease of cloud width under more polluted conditions is hypothesized to be due to strong evaporation at the sides of clouds. Jiang et al. (2006) used large eddy simulation to demonstrate that as aerosol concentration increases, an evaporation-entrainment feedback is likely to dilute cumulus clouds instead of increasing cloud

lifetime (aerosol second indirect effect), even though precipitation is suppressed. Normally, an actively growing cumulus cloud consists of a positively buoyant updraft core surrounded by a shell of negatively buoyant air driven by entrainment and evaporative cooling (Rodts et al., 2003; Heus and Jonker, 2008; Small et al., 2009). This pattern of buoyancy can form a vortical circulation within and around the cloud causing mixing between the cloud and the sub-saturated cloud-free environment adjacent to it. Higher aerosol loading results in smaller droplets that have shorter evaporation time scales. The enhanced evaporation rate intensifies the cloud edge evaporation, generating stronger negative buoyancy at the cloud side, and thus producing a stronger horizontal buoyancy gradient $B'_h \sim \frac{d\theta'_v}{dx}$ (Small et al., 2009), where θ'_v is the virtual potential temperature perturbation and dx is the cloud horizontal width. The stronger horizontal buoyancy gradient in turn results in stronger vortical circulation which leads to more entrainment mixing with dry air, thereby increasing cloud evaporation from the cloud edge.

The virtual potential temperature perturbation was first calculated from each individual cloud penetration (for details of calculation see Appendix) and then averaged for all clouds in the three days in Case L and three days in Case H. Panel a of Fig. 8 shows the PDF of all calculated θ'_v . In Case L the θ'_v ranges from -3.74 K to 3.82 K while in Case H it ranges from -7.21 K to 7.27 K. Panel b of Fig. 8 shows the daily averaged θ'_v . Case H has both greater negative and positive buoyancy indicating greater $d\theta'_v$. According to the relationship $B'_h \sim \frac{d\theta'_v}{dx}$, Case H is associated with greater $d\theta'_v$ (Figure 8) and smaller dx

(Figure 6). Hence, the horizontal buoyancy gradient should become greater, which in turn accelerates cloud side entrainment and evaporation and causes narrower clouds.

Another factor affecting cloud width is the elevated BC may burn off the cloud layer first from cloud edge. These effects may work together leading to the observed narrower clouds. However, the observed narrower clouds in Case H do not correspond to a reduction of cloud fractional coverage (CF) on the regional scale. Cloud fractional coverage (CF) is a crucial factor in determining cloud contribution to climate forcing. Although CF was not measured during CARDEX, high-resolution satellite imagery suggests that low cloud cover increases with increasing aerosol optical thickness in the dry season over the northern Indian Ocean (Dey et al., 2011). Therefore, the observed narrower clouds in Case H may not correspond to a reduction of CF at the regional scale if there were more clouds under polluted conditions. Further study into the frequency of occurrence and regional coverage of clouds in this region is warranted. The net cooling of radiative forcing due to aerosol is discussed in the next section. Further tests about if more clouds presented in high polluted condition are needed.

3.4 Aerosol perturbed cloud radiative forcing

The variations of clouds between the L case and H case may result in changes in radiative flux. Using the CERES data, we analyzed the TOA cloud SW forcing as a function of AOD. The results are shown in Fig. 9. Although substantial variability is apparent, a relationship can be found between net cloud SW forcing and AOD. As AOD increases, the magnitude of cloud SW forcing increases dramatically (the purple dashed curve in Fig. 9), causing a net daily maximum cooling that can reach over 70 W m^{-2} . The increase

of cloud forcing with AOD is greater than the increase in aerosol direct forcing induced by the aerosol scattering (given by the gradual green dash curve in Fig. 9). As the consequence of pollution, the regional TOA forcing increases significantly with increasing AOD due to the observed deepening of clouds and increasing cloud fraction (Dey et al., 2011).

3.5 Correlation between meteorology and aerosol-cloud properties

For empirical studies of aerosol effects on clouds, there is always a concern that the relationships between aerosols and clouds may arise simply from coincidental aerosol and cloud variations due to meteorological variability. In this study, we only analyzed data in dry days to minimize the meteorological impacts on both aerosol and cloud. To further explore the possibility that the regional dynamics may lead to coincidental aerosol and cloud variations, a linear regression analysis was performed with the European Center for Medium-Range Weather Forecast (ECMWF) ERA-Interim Reanalysis dataset. Table 3 shows the linear correlation between the daytime aerosol/cloud properties (e.g., N_a , LWP) and typical dynamical parameters (e.g., temperature, winds, divergence), which can influence the aerosol distribution and cloud formation, from February and March ECMWF data over the MCOH station. These results do not suggest a strong dynamical effect related to the large-scale dynamics, at least in the ECMWF reanalysis, that might induce coincidental changes in surface aerosol concentration and cloud LWP. Therefore, the observed cloud variations may primarily due to aerosol effects. Nevertheless, model simulations are needed for future work to better separate the effects from meteorological parameters.

4 Conclusions

This study presents observed cloud properties under low atmospheric water vapor conditions from the CARDEX field campaign that took place during the winter monsoon season, in February and March, 2012, close to the observation station MCOH over the northern Indian Ocean. The unique feature in this region is that the prevailing wind originates from the north and northeast, passing over the highly polluted Indian subcontinent causing the trade cumulus clouds to be embedded in haze over a large area. An essential component of the CARDEX campaign was equipping UAVs with instruments to obtain high-frequency aerosol and cloud data. We used a combination of ground station observations, UAV measurements, and large-scale satellite data to characterize the trade cumulus clouds over the northern Indian Ocean.

Comparison of cloud microphysics, macrophysics and radiative properties on dry days ($PWV < 40 \text{ kg m}^{-2}$) for high pollution (Case H) and low pollution (Case L) are presented in this paper. More polluted clouds are associated with more and smaller cloud droplets. These clouds are substantially deeper and narrower with greater cloud LWP than less polluted clouds, which is attributed to the observed thicker saturated layer in Case H as well as the observed lower CBH and slightly higher CTH. The deeper and narrower clouds in Case H are mainly due to the warmer, more humid and shallower BL and potentially also the intensified cloud edge evaporation effect as a result of aerosol loading. The changes in clouds that are embedded in a layer with a high concentration of absorbing aerosols over this region are not consistent with a reduction in cloud coverage and cloud LWP via the semi-direct effect (Hansen et al. 1997; Ackerman et al. 2000).

Instead, cloud cover and cloud LWP increase with increased BC aerosol. As a consequence of pollution aerosols, the regional TOA SW forcing increases significantly due to the deeper clouds (increased cloud optical and physical depth) which develop under highly polluted conditions.

This study focused on data from dry days since the measured cloud, and meteorological parameters show greater variation on wet days. But this does not mean the observed aerosol-cloud relationship is only valid under dry condition as the cloud SW forcing increases with AOD for all conditions. We note that CARDEX was carried out during the dry monsoon season, so we sampled more data on dry days compared with wet days. A longer measurement period and analysis of long-term satellite data would allow for more samples on wet days and perhaps overcome the noise associated with the greater cloud variability on those days. Because observed correlations cannot fully explain the cause and effect relationship between aerosols and clouds, further modeling studies are required to isolate the impact of aerosols from other meteorological impacts on cloud properties.

Acknowledgments

The CARDEX field campaign was sponsored by the National Science Foundation Grant ATM07-21142 and conducted by the Scripps Institution of Oceanography at the University of California at San Diego in collaboration with the Desert Research Institute, Stockholm University, Argonne National Laboratory, and the Max Planck Institute for Chemistry. V. Ramanathan is the principal investigator of CARDEX, Eric M. Wilcox is the Co-PI, and H. Nguyen was the field director who conducted the campaign with full support by the government of the Maldives. E. M. Wilcox and L. Gao were supported by NASA grant NNX11AG89G. We appreciate Professor Douglas H. Lowenthal for comments and editing. Full details of the CARDEX campaign can be found at http://www-ramanathan.ucsd.edu/files/CARDEX_prop_Jun_20.pdf. This study is Paper No. 4 from the CARDEX campaign.

Reference

- Ackerman, A. S. O. B. Toon, D. E. Stevens, A. J. Heymsfield, V. Ramanathan and E. J. Welton: Reduction of tropical cloudiness by soot, *Science*, 288, 1042-1047, 2000.
- Albrecht, B. A.: Aerosols, cloud microphysics, and fractional cloudiness, *Science*, 245, 1227-1230 % @ 0036-8075, 1989.
- Andreae, M. O.: Correlation between cloud condensation nuclei concentration and aerosol optical thickness in remote and polluted regions, *Atmospheric Chemistry and Physics*, 9, 543-556 % @ 1680-7316, 2009.
- Bender, F. A. M., Engström, A., and Karlsson, J.: Factors Controlling Cloud Albedo in Marine Subtropical Stratocumulus Regions in Climate Models and Satellite Observations, *Journal of Climate*, 29, 3559-3587, 10.1175/jcli-d-15-0095.1, 2016.
- Bony, S.: Marine boundary layer clouds at the heart of tropical cloud feedback uncertainties in climate models, *Geophysical Research Letters*, 32, 10.1029/2005gl023851, 2005.
- Bosch, C., Andersson, A., Kirillova, E. N., Budhavant, K., Tiwari, S., Praveen, P. S., Russell, L. M., Beres, N. D., Ramanathan, V., and Gustafsson, Ö.: Source-diagnostic dual-isotope composition and optical properties of water-soluble organic carbon and elemental carbon in the South Asian outflow intercepted over the Indian Ocean, *Journal of Geophysical Research: Atmospheres*, 119, 2014.
- Boucher, O., Randall, D., Artaxo, P., Bretherton, C., Feingold, G., Forster, P., Kerminen, V. M., Kondo, Y., Liao, H., and Lohmann, U.: Clouds and aerosol-Climate change 2013: The physical science basis. Contribution of working group I to the fifth assessment report of the intergovernmental panel on climate change, 2013.
- Corrigan, C. E., Ramanathan, V., and Schauer, J. J.: Impact of monsoon transitions on the physical and optical properties of aerosols, *Journal of Geophysical Research*, 111, 10.1029/2005jd006370, 2006.
- Corrigan, C. E., Roberts, G. C., Ramana, M. V., Kim, D., and Ramanathan, V.: Capturing vertical profiles of aerosols and black carbon over the Indian Ocean using autonomous unmanned aerial vehicles, *Atmos. Chem. Phys.*, 8, 737-747, 10.5194/acp-8-737-2008, 2008.
- de Reus, M., Krejci, R., Williams, J., Fischer, H., Scheele, R., and Ström, J.: Vertical and horizontal distributions of the aerosol number concentration and size distribution over the northern Indian Ocean, *Journal of Geophysical Research: Atmospheres*, 106, 28629-28641, 10.1029/2001jd900017, 2001.
- Dey, S., Di Girolamo, L., Zhao, G., Jones, A. L., and McFarquhar, G. M.: Satellite-observed relationships between aerosol and trade-wind cumulus cloud properties over the Indian Ocean, *Geophysical Research Letters*, 38, n/a-n/a, 10.1029/2010gl045588, 2011.

- Freud, E., and Rosenfeld, D.: Linear relation between convective cloud drop number concentration and depth for rain initiation, *Journal of Geophysical Research: Atmospheres*, 117, n/a-n/a, 10.1029/2011jd016457, 2012.
- Hansen, J., Sato, M., and Ruedy, R.: Radiative forcing and climate response, *Journal of Geophysical Research: Atmospheres*, 102, 6831-6864, 10.1029/96jd03436, 1997.
- Hartmann, D. L., and Doelling, D.: On the net radiative effectiveness of clouds, *Journal of Geophysical Research: Atmospheres*, 96, 869-891 % @ 2156-2202, 1991.
- Heus, T., and Jonker, H. J. J.: Subsiding Shells around Shallow Cumulus Clouds, *Journal of the Atmospheric Sciences*, 65, 1003-1018, 10.1175/2007jas2322.1, 2008.
- Heymsfield, A. J., and McFarquhar, G. M.: Microphysics of INDOEX clean and polluted trade cumulus clouds, *Journal of Geophysical Research. D. Atmospheres*, 106, 28 % @ 0148-0227, 2001.
- Holben, B. N., Eck, T. F., Slutsker, I., Tanre, D., Buis, J. P., Setzer, A., Vermote, E., Reagan, J. A., Kaufman, Y. J., and Nakajima, T.: AERONET—A federated instrument network and data archive for aerosol characterization, *Remote sensing of environment*, 66, 1-16 % @ 0034-4257, 1998.
- Höpner, F., Bender, F. A. M., Ekman, A. M. L., Praveen, P. S., Bosch, C., Ogren, J. A., Andersson, A., Gustafsson, Ö., and Ramanathan, V.: Vertical profiles of optical and microphysical particle properties above the northern Indian Ocean during CARDEX 2012, *Atmospheric Chemistry and Physics*, 16, 1045-1064, 10.5194/acp-16-1045-2016, 2016.
- James, W. F.: Effect of Aerosol Composition on Cloud Droplet Size Distribution: A Numerical Study, *Journal of the Atmospheric Sciences*, 31, 1358-1367, 10.1175/1520-0469(1974)031<1358:EOACOC>2.0.CO;2 % U
<https://journals.ametsoc.org/doi/abs/10.1175/1520-0469%281974%29031%3C1358%3AEOACOC%3E2.0.CO%3B2>, 1974.
- Jiang, H., Xue, H., Teller, A., Feingold, G., and Levin, Z.: Aerosol effects on the lifetime of shallow cumulus, *Geophysical Research Letters*, 33, 10.1029/2006gl026024, 2006.
- McComiskey, A., and Feingold, G.: The scale problem in quantifying aerosol indirect effects, *Atmospheric Chemistry and Physics*, 12, 1031-1049, 10.5194/acp-12-1031-2012, 2012.
- McFarquhar, G. M., and Heymsfield, A. J.: Parameterizations of INDOEX microphysical measurements and calculations of cloud susceptibility- Applications for climate studies, *Journal of Geophysical Research. D. Atmospheres*, 106, 28 % @ 0148-0227, 2001.
- Medeiros, B., Stevens, B., Held, I. M., Zhao, M., Williamson, D. L., Olson, J. G., and Bretherton, C. S.: Aquaplanets, climate sensitivity, and low clouds, *Journal of Climate*, 21, 4974-4991 % @ 1520-0442, 2008.

- Pincus, R., and Baker, M. B.: Effect of precipitation on the albedo susceptibility of clouds in the marine boundary layer, *Nature*, 372, 250-252 % @ 0028-0836, 1994.
- Pistone, K.: Observational estimates of planetary albedo changes due to anthropogenic effects, University of California, San Diego, 2014.
- Pistone, K., Praveen, P. S., Thomas, R. M., Ramanathan, V., Wilcox, E. M., and Bender, F. A. M.: Observed correlations between aerosol and cloud properties in an Indian Ocean trade cumulus regime, *Atmospheric Chemistry and Physics*, 16, 5203-5227, 10.5194/acp-16-5203-2016, 2016.
- Ramana, M. V., and Ramanathan, V.: Abrupt transition from natural to anthropogenic aerosol radiative forcing: Observations at the ABC-Maldives Climate Observatory, *Journal of Geophysical Research*, 111, 10.1029/2006jd007063, 2006.
- Ramana, M. V., Ramanathan, V., Kim, D., Roberts, G. C., and Corrigan, C. E.: Albedo, atmospheric solar absorption and heating rate measurements with stacked UAVs, *Quarterly Journal of the Royal Meteorological Society*, 133, 1913-1931, 10.1002/qj.172, 2007.
- Ramanathan, V., Crutzen, P. J., Lelieveld, J., Mitra, A. P., Althausen, D., Anderson, J., Andreae, M. O., Cantrell, W., Cass, G. R., Chung, C. E., Clarke, A. D., Coakley, J. A., Collins, W. D., Conant, W. C., Dulac, F., Heintzenberg, J., Heymsfield, A. J., Holben, B., Howell, S., Hudson, J., Jayaraman, A., Kiehl, J. T., Krishnamurti, T. N., Lubin, D., McFarquhar, G., Novakov, T., Ogren, J. A., Podgorny, I. A., Prather, K., Priestley, K., Prospero, J. M., Quinn, P. K., Rajeev, K., Rasch, P., Rupert, S., Sadourny, R., Satheesh, S. K., Shaw, G. E., Sheridan, P., and Valero, F. P. J.: Indian Ocean Experiment: An integrated analysis of the climate forcing and effects of the great Indo-Asian haze, *Journal of Geophysical Research: Atmospheres*, 106, 28371-28398, 10.1029/2001jd900133, 2001.
- Ramanathan, V., Ramana, M. V., Roberts, G., Kim, D., Corrigan, C., Chung, C., and Winker, D.: Warming trends in Asia amplified by brown cloud solar absorption, *Nature*, 448, 575-578, 10.1038/nature06019, 2007.
- Ramanathan, V., Thomas, R. M., Praveen, P. S., Nguyen, H. V., Wilcox, E., Bender, F. A. M., and Pistone, K.: Cloud Aerosol Radiative Forcing Dynamics EXperiment (CARDEX), in, 2011.
- Roberts, G. C., Ramana, M. V., Corrigan, C., Kim, D., and Ramanathan, V.: Simultaneous observations of aerosol-cloud-albedo interactions with three stacked unmanned aerial vehicles, *Proceedings of the National Academy of Sciences of the United States of America*, 105, 7370-7375, 10.1073/pnas.0710308105, 2008.

- Rodts, S. M. A., Duynkerke, P. G., and Jonker, H. J. J.: Size distributions and dynamical properties of shallow cumulus clouds from aircraft observations and satellite data, *Journal of the Atmospheric Sciences*, 60, 1895-1912 % @ 1520-0469, 2003.
- Rosenfeld, D., Andreae, M. O., Asmi, A., Chin, M., de Leeuw, G., Donovan, D. P., Kahn, R., Kinne, S., Kivekäs, N., Kulmala, M., Lau, W., Schmidt, K. S., Suni, T., Wagner, T., Wild, M., and Quaas, J.: Global observations of aerosol-cloud-precipitation-climate interactions, *Reviews of Geophysics*, 52, 750-808, 10.1002/2013rg000441, 2014a.
- Rosenfeld, D., Sherwood, S., Wood, R., and Donner, L.: Atmospheric science. Climate effects of aerosol-cloud interactions, *Science*, 343, 379-380, 10.1126/science.1247490, 2014b.
- Satheesh, S. K., Moorthy, K. K., Babu, S. S., Vinoj, V., and Dutt, C. B. S.: Climate implications of large warming by elevated aerosol over India, *Geophysical Research Letters*, 35, 10.1029/2008gl034944, 2008.
- Small, J. D., Chuang, P. Y., Feingold, G., and Jiang, H.: Can aerosol decrease cloud lifetime?, *Geophysical Research Letters*, 36, 10.1029/2009gl038888, 2009.
- Stephens, G. L.: Cloud feedbacks in the climate system: A critical review, *Journal of Climate*, 18, 237-273 % @ 1520-0442, 2005.
- Stevens, B., and Feingold, G.: Untangling aerosol effects on clouds and precipitation in a buffered system, *Nature*, 461, 607-613, 10.1038/nature08281, 2009.
- Stocker, T. F., Qin, D., Plattner, G.-K., Tignor, M. M. B., Allen, S. K., Boschung, J., Nauels, A., Xia, Y., Bex, V., and Midgley, P. M.: *Climate Change 2013 The Physical Science Basis*, 2013.
- Thomas, R. M., Praveen, P. S., Wilcox, E. M., Pistone, K., Bender, F., and Ramanathan, V.: First uav measurements of entrainment layer fluxes with coupled cloud property measurements, 2012, 0211.
- Tiedtke, M.: A comprehensive mass flux scheme for cumulus parameterization in large-scale models, *Monthly Weather Review*, 117, 1779-1800 % @ 1520-0493, 1989.
- Twomey, S.: Pollution and the planetary albedo, *Atmospheric Environment (1967)*, 8, 1251-1256 % @ 0004-6981, 1974.
- Warner, J.: The water content of cumuliform cloud, *Tellus*, 7, 449-457 % @ 2153-3490, 1955.
- Wielicki, B. A., Barkstrom, B. R., Harrison, E. F., Lee, R. B. III, Smith, G. L., and Cooper, J. E.: Clouds and the Earth's Radiant Energy System (CERES): An Earth Observing System Experiment, *B. Am. Meteorol. Soc.*, 77, 853-868, 1996.
- Wilcox, E. M., Thomas, R. M., Praveen, P. S., Pistone, K., Bender, F. A., and Ramanathan, V.: Black carbon solar absorption suppresses turbulence in the atmospheric boundary layer,

Proceedings of the National Academy of Sciences of the United States of America,
10.1073/pnas.1525746113, 2016.

Table 1: List of data and instruments used in this study. The temporal and spatial resolution of data, instrument detection limit and precision, and platforms where the measurements took place are shown in this table.

Variables	Description	Instrument	Temporal/spatial resolution	Detection limit/precision	Platform
CPC	Particle number concentration (cm^{-3})	TSI Condensation particle counter (CPC, model 3022)	1-minute/-	Particle concentration [0 10 ⁷]/1 with diameter [0.01 10] μm	MCOH/UAV
CB	Cloud base height (m)	SigmaSpace Mini Pulse Lidar (MPL)	2-minute/-	[250 ~15000]/30	MCOH
PWV	Precipitable water vapor (kg m^{-2})	Microwave radiometer	~30-second/-	[0 100]/~0.5	MCOH
LWP	Cloud liquid water path (g m^{-2})			[1 3000]/5%	
T	Temperature ($^{\circ}\text{C}$)	Meteorological probe package	1-minute/-	[-40 70]/0.5	MCOH
RH	Relative humidity (%)			[0 100]/2	
P	Pressure (hPa)			[500 1100]/1	
WS	Wind speed (m s^{-1})			[0 30]/0.3	
WD	Wind direction ($^{\circ}$)			[0 359]/5	
N_d	Cloud droplet number concentration (cm^{-3})	Cloud droplet spectrometer	1-second/30 m	Particle concentration [0 2000]/~10 with diameter [1 50] μm	UAV
R_e	Cloud droplet effective radius (μm)				
CDS	Cloud droplet size distribution				
LWC	Cloud liquid water content (g m^{-3})				
AOD_{550}	Aerosol optical depth at 550nm	AERONET Level 2 V2	1-hourly/-	[0 -]/0.02	MCOH
AOD_{550}^1	Aerosol optical depth at 550 nm	MODIS Level 2	daily/10 km	[-0.1 5]/0.1	Satellite

CTP/CTT/CTH	Cloud top pressure (hPa)/temperature (K)/height (m)		daily/1km	[0 18000]/50	
TOA flux	TOA shortwave flux (W m^{-2})	CERES SYN1deg	3-hourly/1°	[0 1400]/0.1	Satellite
AOD ₅₅₀ ²	Aerosol optical depth at 550 nm			[-0.1 5]/0.1	
1. AOD as shown in Fig. 2 and 6					
2. AOD as shown in Fig. 8					

Table 2: Average value and one standard deviation of aerosol and cloud properties during CARDEX compared to MAC 2006 and INDOEX 1999. Note: 1) CARDEX results were filtered by PWV to only consider the dry days, the MAC and INDOEX results were not filtered by water vapor conditions; 2) the criterion used to determine aerosol conditions in CARDEX and MAC are, Case L ($N_a < 1000 \text{ cm}^{-3}$), Case M ($1000 \text{ cm}^{-3} < N_a < 1500 \text{ cm}^{-3}$) and Case H ($N_a > 1500 \text{ cm}^{-3}$), but in INDOEX results, the Case L* corresponds to $N_a < 500 \text{ cm}^{-3}$, Case M* corresponds to N_a between 500 and 1500 cm^{-3} , the Case H is defined the same as CARDEX and MAC; 3) CARDEX and MAC results were reported as average values while INDOEX results were reported as median values.

Parameters	CARDEX 2012		MAC 2006		INDOEX 1999		
	Case L	Case H	Case L	Case M	Case L*	Case M*	Case H
$N_a (\text{cm}^{-3})$	882±207	1753±259	783±115	1347±137	<500	500~1500	>1500
$N_d (\text{cm}^{-3})$	295±175	607±287	248±76	310±114	89.2	229.9	315.7
$R_e (\mu\text{m})$	5.54±0.53	4.53±0.47	6.82±0.50	6.34±0.37	7.93	5.7	5.8
LWC (g m^{-3})	0.24±0.11	0.30±0.13	0.34±0.17	0.38±0.14	0.145	0.13	0.159
# of clouds	147	229	63	109	-	-	-
Cloud width	253±79	208±63	282±83	248±65	125.1/182.2	128.3/210.1	130.4/186.7

a. INDOEX results are from Heymsfield and McFarquhar (2001).

Table 3: Linear regression analysis of surface aerosol number concentration and cloud LWP with dynamical parameters in the March 2012 ECMWF ERA-Interim reanalysis at the model grid cell corresponding to the MCOH station. Correlation coefficients (r) are shown with the sign of the relationship. To compare with measured aerosol and cloud properties, the ECMWF reanalysis data (6-hour) was interpolated into 1-hour temporal resolution to match hourly mean aerosol and cloud parameters.

Reanalysis parameters	Correlation with N_a	Correlation with LWP
Divergence at 1000 hPa	-0.06	0.01
Divergence at 750 hPa	-0.09	0.12
Geopotential at 750 hPa	0.21	0.20
Lower tropospheric stability ($\theta_{750}-\theta_{1000}$)	-0.20	0.15
Relative humidity at 1000 hPa	0.16	0.18
Relative humidity at 750 hPa	0.05	0.23
Zonal velocity at 1000 hPa	-0.05	-0.18
Zonal velocity at 750 hPa	-0.17	-0.14
Meridional velocity at 1000 hPa	-0.01	0.19
Meridional velocity at 750 hPa	-0.19	0.02
Vertical velocity at 925 hPa	-0.01	0.03
Vertical velocity at 750 hPa	0.03	-0.11

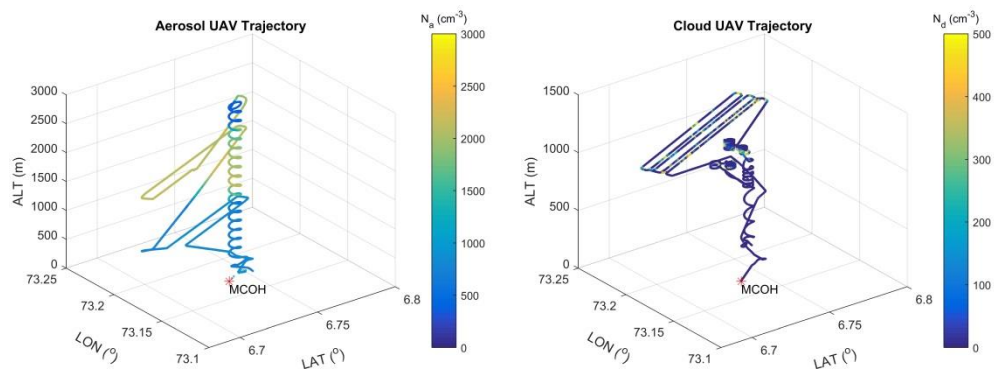


Figure 1: The flight patterns of aerosol payload UAV (left) and cloud payload UAV (right) on March 11, 2012. The color bars represent aerosol number concentration (N_a , cm^{-3}) and cloud droplet number concentration (N_d , cm^{-3}) along the trajectories respectively. The aerosol UAV typically spiraled up to 3 km to measure the profile of particles and performed several level flights on the descending leg to measure the aerosol absorption coefficient as shown in the figure. The cloud UAV typically first ascended to an altitude to penetrate the cloud horizontally and randomly, then ascended to another altitude to do the cloud penetration. On March 11, an elevated aerosol layer with N_a greater than 2000 cm^{-3} can be seen clearly from 1.5 to 2 km height and the cloud layer is right beneath the aerosol layer with N_d close to 500 cm^{-3} .

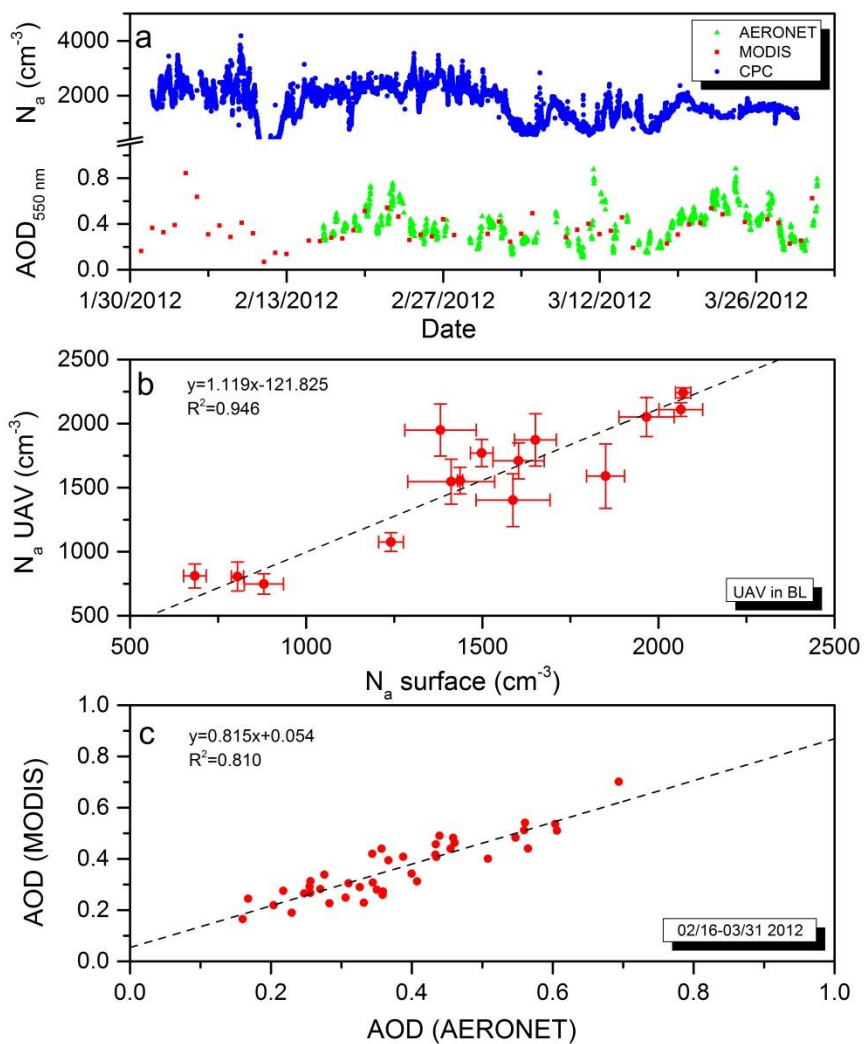


Figure 2: a) Time series of surface aerosol number concentration from CPC, AOD from AERONET and MODIS during CARDEX. b) Comparison between surface CPC and UAV measured aerosol number concentration within the boundary layer. Each dot represents the mean with crosses represent the standard deviations. c) Comparison between AERONET and MODIS measured AOD. MODIS AOD at 550 nm was directly obtained from MODIS Level 2 aerosol product with spatial resolution at 10 km. AERONET AOD at 550 nm was linearly interpolated over the natural logarithm of the spectral bands at 470, 675, and 870 μm .

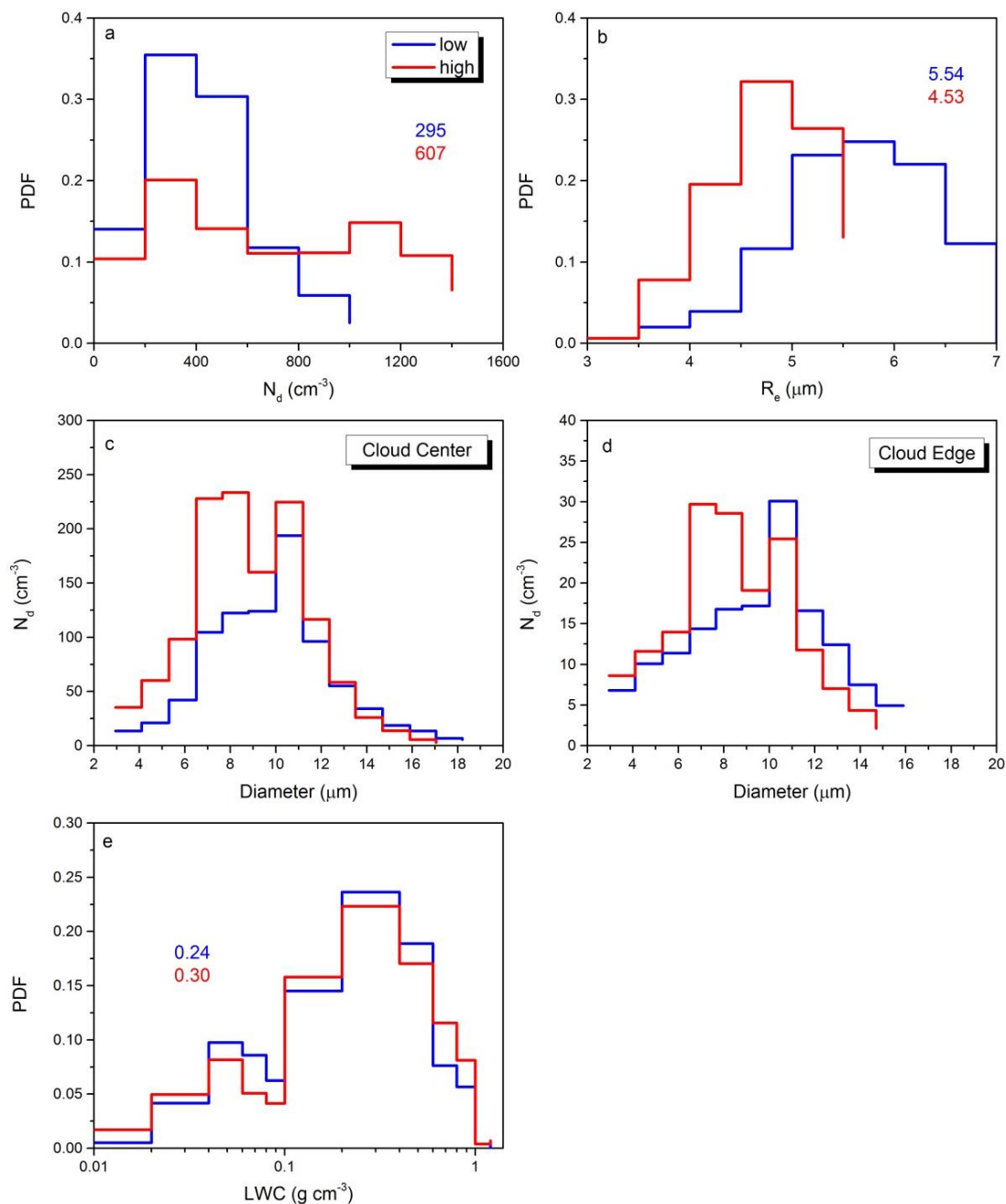


Figure 3: The PDF of the cloud droplet number concentration N_d , cloud droplet effective radius R_e , and liquid water content (LWC) for two pollution conditions with mean values reported in the figure (panel a, b, and e, the red line/number represents Case H, and the blue line/number represents Case L). The cloud droplet size distribution (CSD) for cloud center and cloud edge under the two conditions (panel c and d). The cloud center and edge are distinguished using the following criterion: define a cloud point where the measured cloud droplet number concentration is greater than 50 cm^{-3} and cloud liquid water content

is greater than 0.01g m^{-3} (refers to McFarquhar and Heymsfield (2001)), at least four consecutive cloud points can be considered as a cloud penetration (i.e., cloud width > 100 m). For each cloud penetration, take an average of the middle two points to represent the cloud center, and the average of the first and last points is treated as cloud edge.

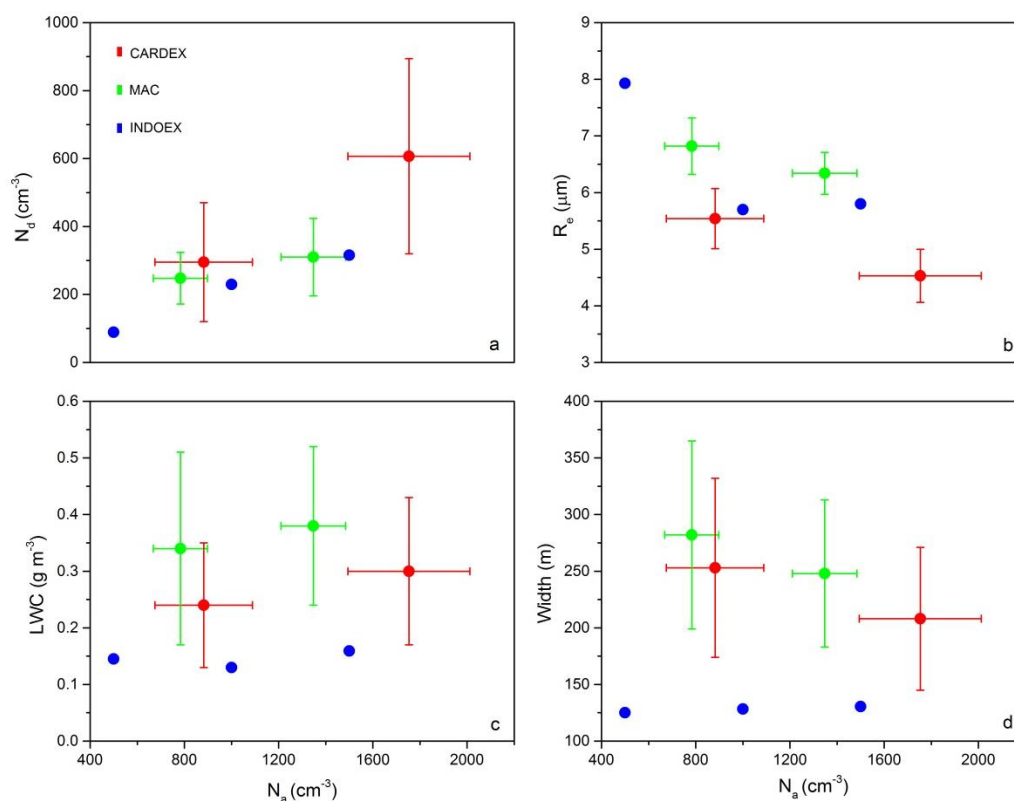


Figure 4: (a) Cloud droplet number concentration N_d versus the aerosol number concentration N_a during CARDEX (red) and MAC (green) with the mean and standard deviation indicated by the crosses, and INDOEX (blue) with the median value. (b), (c) and (d), the same as (a) but the Y axes represent cloud droplet effective radius, liquid water path, and cloud width, respectively. Note: INDOEX results from Heymsfield and McFarquhar (2001) only show the ranges of condensation nuclei concentration (Table 2), so for convenience of visualization, the N_a values for INDOEX were assigned as Case L ($N_a=500 \text{ cm}^{-3}$), Case M ($N_a=1000 \text{ cm}^{-3}$) and Case H ($N_a=1500 \text{ cm}^{-3}$).

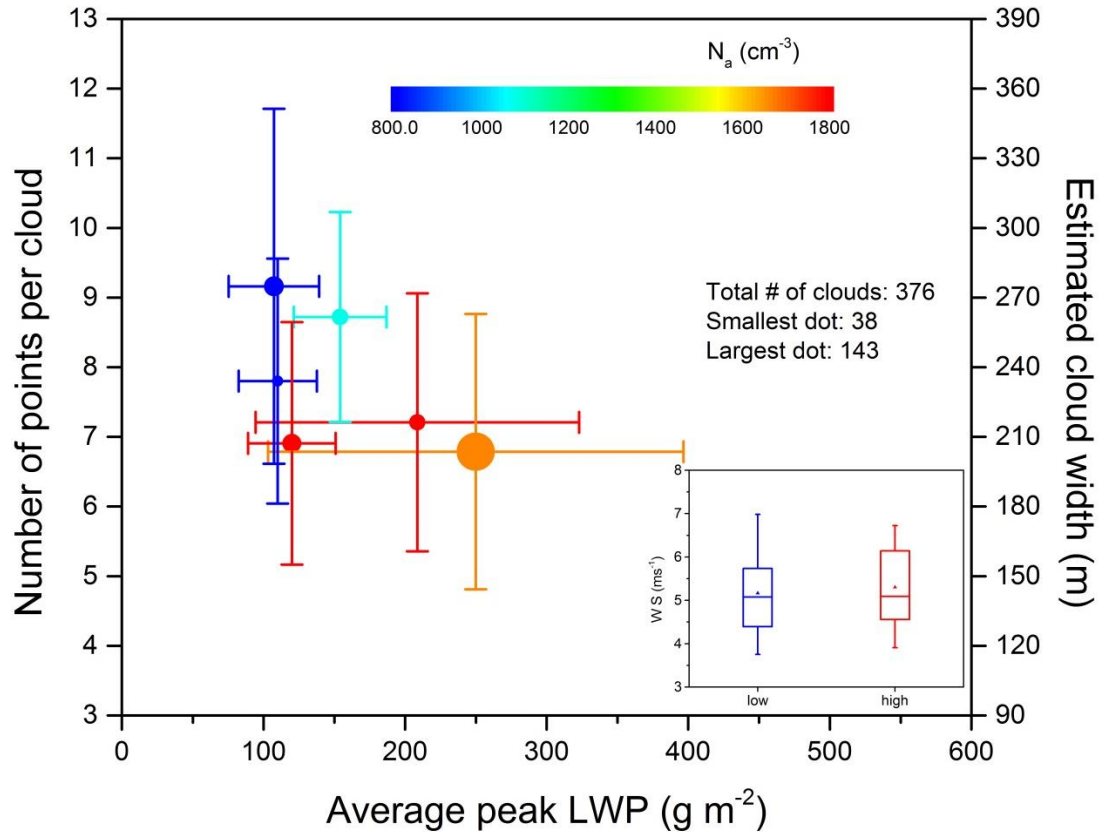


Figure 5: Cloud width as a function of average peak cloud liquid water path (LWP). Here cloud width was given by the consecutive cloudy points (shown in left Y-axis) and then estimated using the number of cloudy points multiplied by the mean UAV penetration speed. Each dot represents the mean value with error bars represent the standard deviations. A total of 376 cloud penetrations were selected. Dot size corresponds to the number of samples in that aerosol bin, where the smallest dot represents 38 samples and the largest dot represents 143 samples. The color bar represents the aerosol concentration. The upper-level wind is usually considered as an important factor regulating cloud morphology. To test if wind speed plays a role in affecting cloud width, the wind horizontal speed at cloud layer was compared for Case H and L, shown in the subplot located in the right bottom corner. The wind speed was derived from 3-D wind probe onboard the UAV. From bottom to top, the symbols represent 10%, 25%, 50%, average (triangle), 75%, and 90% value respectively. To test the quality of derived wind speed, the assimilated wind speed from MERRA reanalysis was also compared with UAV measured wind speed (Fig. 6 left panel).

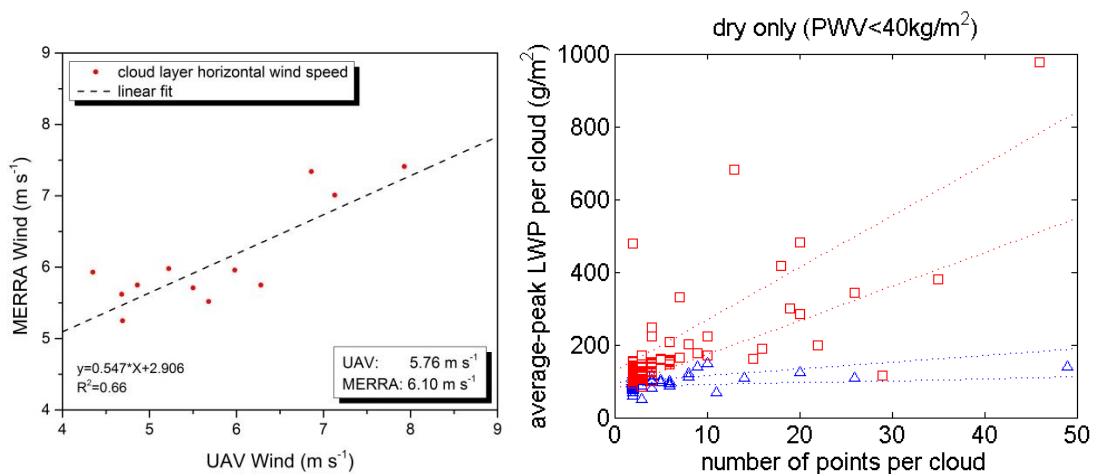


Figure 6: Comparison of cloud layer horizontal wind speed derived from UAV and MERRA (left panel) shows good agreement. The cloud LWP as a function of cloudy points estimated from MWR (right panel). Here the cloudy point was flagged by using surface MWR retrieval. Red symbols represent Case H and blue symbols represent Case L.

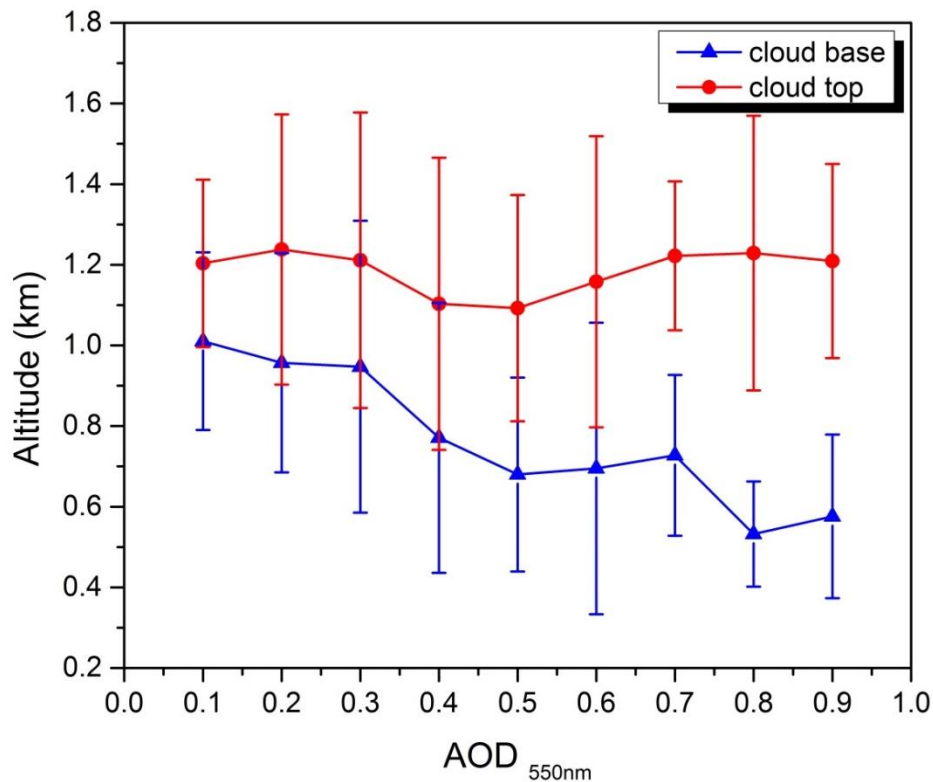


Figure 7: Cloud top height (CTH) and cloud base height (CBH) as a function of binned AOD. Each symbol represents the mean of samples in the corresponding AOD bin and the error bars represent the standard deviation. For example, the very left circle (triangle) represents the mean of CTH (CBH) with AOD between 0 and 0.1. The CTH was obtained from MODIS Level 2 cloud products with high spatial resolution at 1 km and was filtered when CTP is less than 700 hPa and CTT greater than 273 K to only consider the low-level cumulus clouds. The CBH was obtained from ground-based MPL and data was filtered when CBH is greater than 2 km.

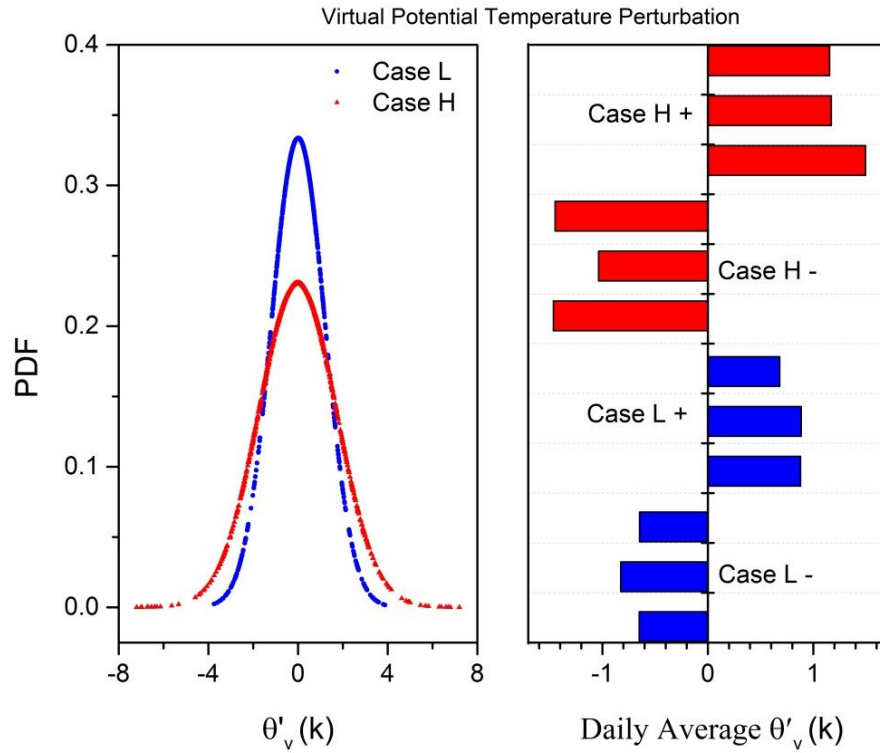


Figure 8: PDF of virtual potential temperature perturbation θ'_v (left panel) and daily averaged θ'_v for Case L and Case H (right panel). The θ'_v was calculated by subtracting the θ_v from the mean of each cloud penetration. Here Case L - represents the daily mean of negative θ'_v in Case L while Case H - represents the daily mean of negative θ'_v in Case H. The same definition applies for Case L + and Case H +. The sum of absolute values of both negative and positive θ'_v is proportional to the magnitude of horizontal buoyancy gradient, which can serve as a metric to determine the cloud side evaporation-cooling effect.

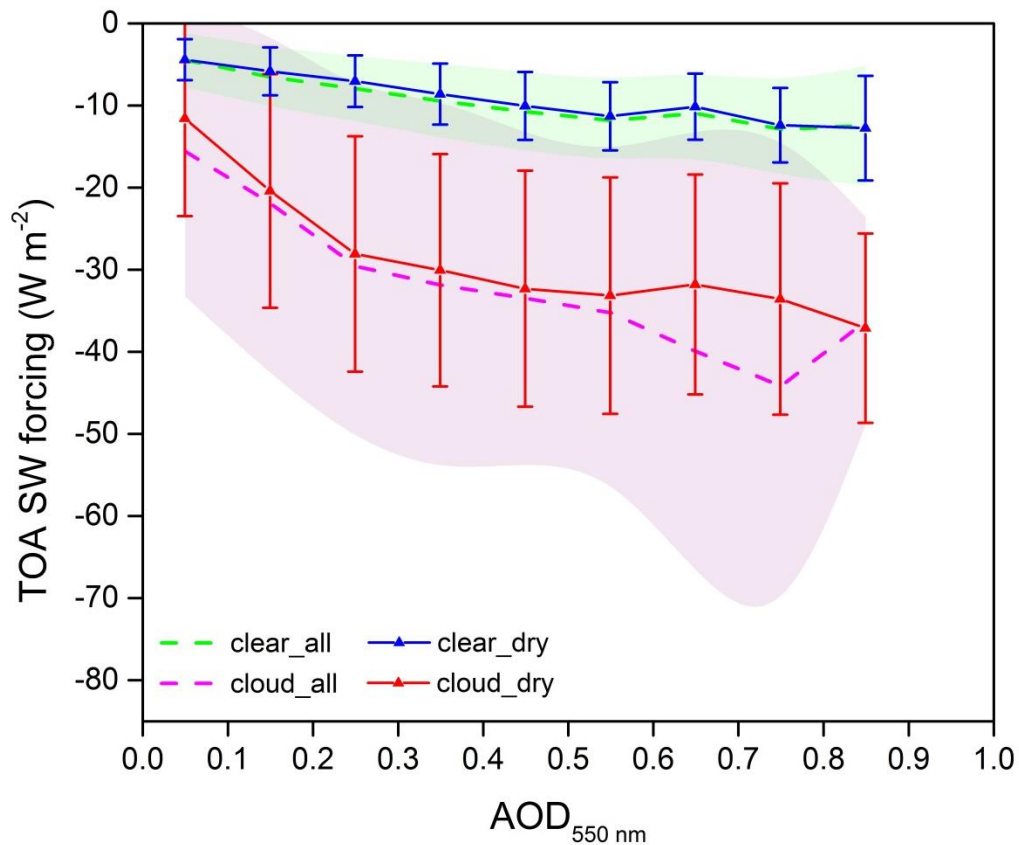


Figure 9: TOA cloud shortwave forcing and aerosol direct forcing as a function of AOD. TOA cloud SW forcing was calculated using the CERES observed TOA cloudy SW flux minus the clean-clear flux. The dashed purple line represents the average cloud SW forcing for all data, and the solid red line with error bars (standard deviation) represents the cloud SW forcing for dry days only. The dashed green line and solid blue line represent the average aerosol direct forcing induced by particle scattering for all data and dry days only, respectively.

Appendix: Calculation of virtual potential temperature perturbation.

By using Clausius-Clapeyron equation we can first calculate the saturation vapor pressure e^* :

$$e_2^* = e_1^* \exp\left(-\frac{L_{lv}}{R_v} \left(\frac{1}{T_2} - \frac{1}{T_1}\right)\right) \quad (\text{A1})$$

where L_{lv} (2260 kJ kg^{-1}) and R_v ($461.51 \text{ J K}^{-1} \text{ kg}^{-1}$) are latent heat and specific gas constant for water vapor, respectively. e_1^* (6.1173 hPa) and T_1 (273.16 K) are known saturation vapor pressure at a known temperature. For any given temperature T_2 we can calculate the saturation vapor pressure e_2^* .

Then we can determine actual vapor pressure v_{pe} and atmospheric specific humidity q_v :

$$v_{pe} = e^* \left(\frac{RH}{100}\right) \quad (\text{A2})$$

$$q_v = 1000 \left(\frac{0.62198 v_{pe}}{P - 0.37802 v_{pe}}\right) \quad (\text{A3})$$

$$T_v = (1 + 0.608 q_v) T \quad (\text{A4})$$

where RH and P are measured relative humidity and pressure. The virtual potential temperature can be derived as:

$$\theta_v = T_v \left(\frac{P_0}{P}\right)^{R_d(1-(0.26 \cdot q_v))/C_{pd}} \quad (\text{A5})$$

where P_0 is the reference pressure 1000 hPa, R_d ($287.104 \text{ J K}^{-1} \text{ kg}^{-1}$) and C_{pd} ($1004 \text{ J K}^{-1} \text{ kg}^{-1}$) are the specific gas constant and the specific heat capacity for dry air, respectively.

Once we calculated θ_v , we averaged θ_v over each cloud penetration, which includes all in cloud and outside cloud (one second before and after cloud event) θ_v . Subtracting each θ_v from the mean then we can get the virtual potential temperature perturbation θ'_v for each measurement point.

Chapter 3

Remote sensing estimate of aerosol indirect forcing by shallow warm clouds

Lan Gao^{1,2}, Eric M. Wilcox¹, Robert C. Levy³, Steve Platnick³, Yunpeng Shan^{1,2}

¹Desert Research Institute, Reno, 89512, USA

²Atmospheric Sciences Graduate Program, University of Nevada Reno, 89557, USA

³Laboratory for Atmospheres, NASA Goddard Space Flight Center, Greenbelt, Maryland, 20771, USA

Correspondence to: Eric M. Wilcox (Eric.Wilcox@dri.edu)

To be submitted to: Atmospheric Chemistry and Physics

Abstract. The impact of atmospheric aerosols on cloud radiative forcing (CRF) is termed the aerosol indirect effect (AIE). The Intergovernmental Panel on Climate Change (IPCC) reported the AIE to be the single largest uncertainty in global radiative forcing. Overall, low-level warm clouds exert the largest impact on the planet's albedo. However, even after decades of effort, the uncertainty of low-level cloud response to aerosol is still high. Previous studies have focused on marine clouds or small spatial scales over the continent (e.g., using surface remote sensing). In this study, a comprehensive analysis of collocated aerosol and cloud properties over North America was performed using multiple remote sensing measurements for the period from August to September 2013. The data set is composed of over 400 million enhanced MODIS Airborne Simulator (eMAS) pixels, of which ~ 60 million pixels passed screening for single-layer warm clouds. After collocating eMAS pixels (0.5 km resolution for aerosol and 50 m resolution for cloud) with each Geostationary Operational Environmental Satellite (GOES) pixel (4 km resolution), 9076 valid data pairs were left for this analysis. Using the anthropogenic aerosol fraction estimated from eMAS fine-mode aerosol, we systematically evaluated cloud response to aerosol and meteorological parameters. Cloud responses to aerosols were highly affected by lower tropospheric stability (LTS) and free troposphere relative humidity (RH_{ft}). The Aerosol-cloud interaction index (ACI) was generally higher in an unstable and humid environment and lower under unstable and dry conditions. The total top of atmosphere (TOA) CRF was calculated to be $\sim -80 \text{ W m}^{-2}$ when the ACI reached 0.3. Aerosol indirect forcing of the estimated anthropogenic portion of the aerosol due to the intrinsic aerosol effect, i.e., on cloud albedo, was estimated to be -0.63 W m^{-2} and the

forcing due to the extrinsic aerosol effect, i.e., on cloud extent, was estimated to be -1.77 W m^{-2} .

1 Introduction

Anthropogenic activities have dramatically increased aerosol emissions since the pre-industrial era (Solomon, 2007). These tiny particles suspended in the atmosphere can directly absorb or scatter solar radiation, and indirectly alter the cloud microphysics (e.g., droplet size distribution and concentration), cloud macrophysics (e.g., liquid water path (LWP), cloud geometric thickness), and radiative properties (e.g., cloud optical thickness (COT), cloud albedo) by serving as the cloud condensation nuclei (CCN) or ice nuclei (IN). The consequences of those processes have been the perturbation of the Earth's radiation budget and climate. The manner in which aerosols affect climate by modifying cloud properties is termed the aerosol indirect effect (AIE), which is considered one of the largest uncertainties in quantifying the anthropogenic radiative forcing of climate (Boucher, 2013). The AIE estimated from previous modeling and/or satellite studies is highly inconsistent (Penner et al., 2011), which limits our ability to predict the climate response accurately.

Shallow warm clouds, generally abundant and optically thick, have been estimated to exert an annual and globally averaged net cooling of -15 W m^{-2} (Hartmann et al., 1992). Latham et al. (2008) estimated that a 6% increase of the albedo of global marine stratocumulus would offset the warming by doubling the atmospheric CO_2 concentration. Since both aerosol loadings and meteorological parameters control cloud properties, it is essential to understand the relative contributions of aerosols and natural meteorological variability to variations in cloud properties. It is thus necessary to study cloud responses to aerosol under various environmental conditions. On seasonal to inter-annual timescales,

variations in shallow warm cloud amount are strongly correlated with variations in lower tropospheric stability (LTS) and atmospheric circulation (Klein and Hartmann, 1993; Wood and Bretherton, 2006). On sub-seasonal timescales, correlations of low cloud amount with meteorological predictors are substantially weaker than on longer timescales. Nevertheless, LTS and free troposphere relative humidity (RH_{ft}) do significantly correlate with variations in low cloud amount (Klein, 1997) and cloud liquid water path (LWP) (Xu et al., 2005). Lebsack et al. (2008) investigated aerosol effects on warm marine cloud by controlling for LTS and estimated aerosol indirect forcing as -0.42 W m^{-2} . Chen et al. (2014) studied global warm marine cloud responses to aerosol under different thermodynamic conditions. Among various meteorological parameters, they found that the LTS and RH_{ft} acted together depending on the state of precipitation to govern the cloud liquid water responses to the presence of aerosols and the strength of aerosol-cloud radiative forcing (CRF). However, the majority of previous studies focused on warm marine clouds or in limited sampling areas over the continent (e.g., studies using data from the Department of Energy's Atmospheric Radiation Measurement are summarized by Feingold and McComiskey [2016]). It is essential to understand aerosol-cloud interactions under various environmental conditions over the continent, where the anthropogenic aerosol concentrations are significantly higher than the global background. To estimate aerosol indirect radiative forcing caused by anthropogenic activities, it is necessary to distinguish the anthropogenic and natural aerosol fractions. However, satellite remote sensing cannot directly accomplish this. Further, anthropogenic aerosol can vary significantly spatially and temporally. Therefore, it is important to quantify the influence of anthropogenic emissions when assessing the total aerosol indirect forcing.

Some previous studies assumed a 30% increase in the global average aerosol concentration since the pre-industrial era (Sekiguchi, 2003;Lebsock et al., 2008). Anthropogenic aerosols are general small (fine mode) compared with nature dust and sea-salt particles. Kaufman et al. (2005) has argued that the fraction of aerosol in the fine-mode size range (particles with diameter $\leq 0.6 \mu\text{m}$) retrieved from Moderate Resolution Imaging Spectroradiometer (MODIS) to estimate the anthropogenic aerosol contribution to cloud microphysical and macrophysical properties.

The cloud response to aerosol, especially the radiative impact, is still the most uncertain component of the overall change in global radiative forcing from the pre-industrial era to the present day. The microphysical, macrophysical, and radiative properties of warm liquid clouds show sensitivity to aerosol loading, but the responses are not uniform. The magnitude and even the sign of the responses appear to depend upon cloud types and meteorological regimes (Khain, 2009). In this paper, we focus on remote sensing measurements across a large sampling area during the Studies of Emissions and Atmospheric Composition, Clouds and Climate Coupling by Regional Surveys (SEAC⁴RS) campaign, which was carried out over North America (mostly centered over the southeastern US) from August to September 2013. We perform a comprehensive investigation of the interactions between aerosols, shallow warm cloud microphysical and macrophysical properties, and large-scale dynamic and thermodynamic states using a combination of aircraft and satellite measurements and meteorological reanalysis data. To improve this assessment, the anthropogenic aerosol fraction is estimated using a high-resolution remote sensing retrieval to evaluate the anthropogenic contribution to the total aerosol indirect effect. This study builds on prior studies of warm clouds by examining a

large sample of continental clouds and applying high-resolution sub-orbital remote sensing data which is capable of resolving smaller clouds and aerosol retrievals in smaller gaps between clouds. The following questions are addressed: 1) how do the microphysical and macrophysical properties of cloud respond to aerosols?; 2) how do aerosol-cloud responses vary under different dynamical regimes?; and 3) what is the quantitative relationship between the ACI and CRF and what is the contribution of anthropogenic aerosols to indirect radiative forcing?

2 Data and Methods

2.1 Data Description

The data used in this study were derived from two months of observations from August to September 2013 with a focus on remote sensing measurements from aircraft and satellite. The dataset includes observations from the enhanced MODIS Airborne Simulator (eMAS) with a spatial resolution of 0.5 km for aerosol and 50 m for cloud, a Cloud Physics Lidar (CPL), and the Geostationary Operational Environmental Satellite (GOES) with a spatial resolution of 4 km. The North American Mesoscale Forecast System (NAM) reanalysis data were used in this study to describe the meteorological conditions.

Table 1 lists the sensors and retrieved cloud and aerosol properties used in this study and indicates which data are used to address the research questions outlined above. The primary data used in this study is eMAS data, which were pre-, in-flight and post-deployment calibrated by the NASA science group (Meyer et al., 2016). The eMAS data were preliminarily filtered using recommended data quality assurance (QA), similar to

those are widely used from MODIS data (Levy et al., 2013; Baum and Platnick, 2006), which means only good quality/high confidence data were used in the following analysis. This would reduce the volume of the dataset to some extent but effectively ensure the quality of data. The aerosol optical depth (AOD) was used in this study as a proxy for column cloud condensation nuclei (CCN), similar to those derived from MODIS (Remer, 2005). The fine-mode fraction of AOD from the eMAS retrieval is used to estimate the amount of anthropogenic aerosol (Kaufman et al., 2005). Cloud properties were obtained from the eMAS retrieval, including the number and types of cloud layers, cloud phase, cloud top temperature (CTT) and pressure (CTP), cloud fractional cover (CF), cloud top effective radius (R_e), cloud optical thickness (τ), and cloud liquid water path (LWP). The pixel-level uncertainties for cloud properties retrieval, the same as used in MODIS retrieval and described in Tsay et al. (2004) and Platnick et al. (2017), were also used to improve the calculation and enhance the results. The GOES-retrieved cloud top height (CTH) and cloud base height (CBH) were used together with the eMAS-derived cloud properties.

To exclude ice and mixed-phase clouds from the analysis, warm liquid clouds were defined as those with eMAS-derived CTP and CTT greater than 500 hPa and 273 K, respectively. The cloud phase retrieval from eMAS was also used to screen out pixels where ice cloud was present. In addition, the CPL provides an independent estimate of vertical aerosol and cloud distribution. For each eMAS scene, the collocated CPL retrieval was used to identify AOD above the cloud which can obscure the scene below cloud top. Thus, the AOD above the cloud must be less than 0.1 to identify cloud responses to changing aerosols (Wilcox et al., 2009). Furthermore, cloud retrievals tend

to become more uncertain due to the weakness of the multiple scattering signal and shadow effects (cloud is between the satellite and the sun) caused by large solar zenith angles. Therefore, only observations with low solar zenith angle (less than 60°) were include to reduce these potential sources of error.

To distinguish between precipitating and non-precipitating clouds, we draw on the results from Rosenfeld and Gutman (1994), Kobayashi (2007) and Rosenfeld et al. (2012). For non-precipitating clouds in those studies, the cloud top R_e was consistently less than $12 \mu\text{m}$. The probability of occurrence of small raindrops increased rapidly once cloud top R_e exceeded $12 \mu\text{m}$. When R_e reached $\sim 14 \mu\text{m}$ warm rain was often more developed. Hence, two regimes were defined to describe precipitation intensity: non-precipitating clouds with cloud top R_e less than $12 \mu\text{m}$ and precipitating clouds with cloud top R_e greater than $16 \mu\text{m}$. Clouds with R_e between 12 and $16 \mu\text{m}$ were classified as transition clouds. Such clouds may produce drizzle but not with the intensity of precipitating clouds and not all transition clouds are certain to be precipitating. Thus, transition clouds were excluded from the following analysis. Figure 1 shows the histogram of cloud top effective radius for all single-layer warm clouds in this analysis. According to cloud top R_e , about 60% ($N=5412$) of all clouds were non-precipitating. About $\sim 16\%$ ($N=1425$) were precipitating. The remainder ($\sim 24\%$) were transition clouds.

Meteorological effects on clouds were evaluated using LTS and RH_{ft} . The LTS was derived based on the potential temperature difference between 700 hPa and 970 hPa ($\text{LTS} = \theta_{700} - \theta_{970}$) calculated from the NAM reanalysis data. The RH_{ft} was obtained by averaging the two levels closest to the height flagged as boundary layer top from the

collocated CPL retrieval. Note that the NAM data are reported every 6 hours with 12 km resolution. For comparison with the eMAS and GOES data, the raw NAM data was interpolated to higher resolution with about 4 km horizontal spacing and 0.5 hour temporal resolution.

Cloud radiative forcing (CRF) is derived from the TOA longwave fluxes and shortwave albedo which are both acquired from GOES retrieval products (Doelling et al., 1998). The CRF can be used to measure the effect of clouds on the reflected solar flux relative to the clear sky flux as a function of variations in AOD. The GOES platform provides continuous pixel-level (4 km) cloud properties and TOA radiative fluxes. Broadband shortwave (SW) and longwave (LW) radiative fluxes at the TOA are estimated from narrowband GOES data using narrowband-to-broadband (NB-BB) conversion formulas (Minnis et al., 1995). Formula coefficients have historically been derived by regressing matched polar-orbiting satellite BB fluxes or radiances with their NB counterparts from GOES. But the GOES data has a resolution of 4 km, which is too coarse to resolve clouds, especially warm cumulus clouds. Therefore, the 4 km pixel product from GOES was used together with the collocated eMAS cloud retrieval to calculate the CRF for each eMAS scene. To determine whether a GOES pixel represented clear or cloudy sky, the GOES pixel was collocated with the corresponding eMAS pixel in space and time. If all of the collocated eMAS pixels were designated as clear sky, then the corresponding GOES pixel was also considered as clear sky. If all eMAS cloud pixels within one GOES pixel were determined to contain single-layer warm clouds, then the corresponding GOES pixel was designated as a cloudy pixel.

2.2 Aerosol-Cloud Interaction Index

Cloud responses to changes in aerosol are typically represented by power-law functions (Feingold et al., 2003). Using a linear regression between aerosol and cloud properties expressed as: $y = a + bx$, where y is the logarithm of the cloud property (dependent variable) and x is the logarithm of the aerosol property (independent variable), then the aerosol-cloud interaction index (ACI) is derived as the estimate of the regression slope (b). The slope is defined as $b = r_{xy} \frac{s_y}{s_x}$, where r_{xy} is the correlation coefficient between x and y , $r_{xy} = \frac{\text{COV}(x,y)}{s_x s_y}$, where $\text{COV}(x,y)$ is the covariance between x and y , and s_x (s_y) is the standard deviation of x (y). Applying this to the aerosol-cloud system yields $\text{ACI} = r_{\text{aerosol,cloud}} \frac{s_{\text{cloud}}}{s_{\text{aerosol}}}$. Commonly used observables for the quantities x and y are effective radius (R_e), cloud optical thickness (τ_c), or cloud droplet number concentration (N_d) for cloud and aerosol optical depth (AOD) or aerosol index (AI, the product of the AOD and the extinction angstrom exponent) for aerosol. McComiskey et al. (2009) showed that there is consistency amongst calculations of ACI using different microphysical proxies, but a constraint on cloud LWP is needed, as described further below. The equation used is as follows:

$$\text{ACI} = -\frac{d \ln R_e}{d \ln A} \Big|_{\text{LWP}}, \quad \text{ACI} = -\frac{d \ln \tau}{d \ln A} \Big|_{\text{LWP}}, \quad \text{ACI} = \frac{1}{3} \frac{d \ln N_d}{d \ln A} \quad (1)$$

where A represents the aerosol properties, e.g., AOD, AI, etc.

Cloud optical properties are highly correlated with LWP (Schwartz et al., 2002). Various factors including meteorology and cloud microphysical properties can result in variability

in optical properties. By constraining LWP, the remaining variability will be due primarily to changes in microphysical properties associated with variation in aerosol. Without this constraint, larger-scale meteorological processes that produce variability in LWP and therefore optical properties will confound detection of aerosol-cloud interactions.

Figure 2 demonstrates the effect of constraining LWP on the ACI calculation. Figure 2 a shows the total data collected from one eMAS scene used for calculation. Figures 2 b, c, and d are the R_e -AOD data pairs in different LWP ranges. Each aerosol and cloud variable was grouped based on 20 g m^{-2} LWP bins. Independent calculations of ACI were made using the aerosol and cloud data from each bin, and then these values were averaged (weighted by the numbers of total data points in each bin) to provide a single ACI value for the scene. It is clear that different LWP bins correspond to different ACI values. The constrained ACI (ACI_{LWP}) and unconstrained ACI (ACI_{all}) are shown from Fig.2 a. The unconstrained ACI value of 0.12 is lower than any of other constrained values of 0.21, 0.24, and 0.28. For this scene, the averaged constrained ACI value is 0.23.

2.3 Methods

Figure 3 is a flowchart for the analysis used to address the issues outlined in the Introduction. Aerosol-cloud interactions are defined in terms the relationship (correlation) between AOD and cloud properties (Fig.3, Q1). eMAS and NAM data were aggregated into each collocated GOES pixel at $4 \text{ km} \times 4 \text{ km}$ resolution to create aerosol and cloud data pairs. A valid data pair must meet the criteria that more than 90% of eMAS pixels within an individual GOES pixel have valid retrievals and can pass the single-layer warm

cloud test (i.e., $CTP > 500$ hPa and $CTT > 273$ K). When averaging the eMAS data within each GOES pixel, the retrieval uncertainties were taken into account. A weight was created for each eMAS pixel within the GOES pixel based on the retrieval uncertainty (i.e., the weight assigned to each eMAS pixel was inversely proportional to the retrieval uncertainty) and weighted averages were calculated. There were 9,076 valid data pairs for the analysis. Cloud properties (R_e , LWP, τ , CF, cloud thickness) were then compared under non-precipitating and precipitating scenarios as a function of AOD.

For any empirical study of aerosol-cloud interactions, it is necessary to separate the effects of aerosols from those from meteorological variations on clouds. This was done by systematically constraining meteorological parameters (Fig.3, Q2). ACI was calculated using the method described in Sect. 2.2 under different meteorological conditions, which were defined in terms of the NAM reanalysis data. Histograms of key meteorological parameters are shown in Fig.5. The variations of the ACI were investigated over a range of meteorological conditions.

Finally, aerosol indirect radiative forcing was evaluated (Fig.3, Q3). Computation of aerosol indirect radiative forcing is based on a top-down approach to estimate CRF as a function of aerosol loading. This effectively reduces the number of free parameters to those (e.g., cloud fraction, albedo, and AOD) that can be most easily retrieved from satellite measurements. The method used to calculate the aerosol indirect radiative forcing at the TOA is similar as that used by Chen et al. (2014) and is derived from the cloud radiative effect equation as:

$$CRF_{sw,lw} = F_{clear} - F_{all} \quad (2)$$

where SW/LW represents the shortwave/longwave components of the radiative flux, F_{clear} is clear sky net radiative flux (i.e., the difference between upward flux and downward flux for pixels containing no clouds), and F_{all} is the TOA net flux that is observed for all sky conditions. Since the focus of this study is shallow warm clouds, ice clouds are excluded from this calculation. F_{all} can be further decomposed into:

$$F_{all} = (1 - CF) \times F_{clear} + CF \times F_{cloud} \quad (3)$$

where CF is the cloud fractional cover over the GOES pixel estimated from the collocated eMAS retrievals and F_{cloud} is the component of the radiative flux contributed by clouds. F_{cloud} can be calculated using equation (3). Combining Eq.2 and Eq.3, the cloud radiative forcing is expressed as:

$$CRF_{sw,lw} = CF \times (A_{clear} - A_{cloud}) \times \bar{F}^\downarrow \quad (4)$$

where A represents the albedo ($A = F^\uparrow - F^\downarrow$). Taking the derivative of Eq.4 with respect to aerosol loading (AOD) gives the cloud radiative effect aerosol sensitivity which is written as:

$$\begin{aligned} \frac{dCRF_{sw}}{d\ln(Aero)} = & [\bar{CF} \left(\frac{dA_{clear}}{d\ln(Aero)} - \frac{dA_{cloud}}{d\ln(Aero)} \right) \\ & + \overline{(A_{clear} - A_{cloud})} \frac{dCF}{d\ln(Aero)}] \times \bar{F}^\downarrow \end{aligned} \quad (5)$$

The first term on the right-hand side of Eq.5 is the intrinsic aerosol effect which represents the impact of aerosol on changes in cloud albedo. The second term is the extrinsic effect, which represents the impact of aerosol on cloud fraction.

To determine the aerosol indirect radiative effect, Eq.5 is multiplied by an amount of aerosol attributable to anthropogenic activities which has been estimated here as the fraction of AOD from fine-mode aerosol as follows:

$$\Delta\alpha = [\log(AOD) - \log(AOD - AOD_{anth})] = \log\left(\frac{1}{1 - A_{frc}}\right) \quad (6)$$

where A_{frc} is the anthropogenic contribution as a fraction of the total aerosol optical depth.

Similarly, the longwave component of the CRF sensitivity to aerosol is derived as:

$$\begin{aligned} \frac{dCRF_{lw}}{d\ln(Aero)} = & \left[\overline{CF} \left(\frac{dF_{clear}}{d\ln(Aero)} - \frac{dF_{cloud}}{d\ln(Aero)} \right) \right. \\ & \left. + \overline{(F_{clear} - F_{cloud})} \frac{dCF}{d\ln(Aero)} \right] \end{aligned} \quad (7)$$

where the F_{clear} and F_{cloud} represent the TOA clear sky and cloudy sky longwave flux.

The primary uncertainties in estimated aerosol indirect forcing are from estimation of anthropogenic aerosol contribution using fine-mode fraction (up to 30%), the relative uncertainty in eMAS measurement is 5-10%. Some sources of error are not presently quantifiable, e.g., surface albedo error (Meyer et al., 2016).

3 Results and discussion

3.1 The effect of aerosol on cloud properties constrained by large-scale dynamics

Averaged aerosol-cloud relationships are plotted in Fig.4. The slope of the linear fits between aerosol and cloud properties are shown in Table 2. Clouds are separated into two categories: precipitating clouds and non-precipitating clouds, classified by cloud top effective radius. AOD fell between 0 and 1 for 95.6% of the total data. It is uncommon for AOD to exceed 1 in the atmosphere except for locations very close to the aerosol source (e.g., wildfire, volcano eruptions). Very high values of AOD may be due to artifacts in the remote sensing retrievals, for example, unresolved broken clouds and aerosol swelling from hygroscopic growth. Therefore, in the following analysis, only AOD less than 1 are considered. In general, non-precipitating and precipitating clouds showed different responses to aerosol loading. Cloud R_e decreased as AOD increased for both types of clouds. However, the aerosol affected cloud R_e more for non-precipitating cloud than for precipitating clouds, as demonstrated in Table 2, where the slope was smaller (negative) for the non-precipitating cloud. This may be due to a higher concentration of larger droplets developed in precipitating clouds, shifting the droplet size distribution to larger sizes (Lebsock et al., 2008). Cloud fraction, LWP, COT and cloud thickness generally increased with AOD for both cloud types. Cloud LWP and COT had a similar response to aerosol loading. COT strongly depends on cloud LWP, as $\tau = \frac{3LWP}{2R_e\rho_l}$. The observed relationship between cloud properties and AOD can be ambiguous (Quaas et al., 2010; Grandey et al., 2013). Large-scale convergence tends to both concentrate aerosols and cause cloud to grow, producing a positive relationship between AOD and LWP, for example. It is therefore necessary to constrain meteorological conditions before evaluating aerosol-cloud interactions.

Large-scale dynamical variability can be represented by Lower Tropospheric Stability (LTS) and free tropospheric relative humidity (RH_{ft}). Both are controlled by large-scale subsidence and play significant roles in cloud formation (Bretherton and Wyant, 1997; Lebock et al., 2008; Chen et al., 2014). Previous attempts to establish dependencies between aerosol-cloud interactions and dynamical parameters such as vertical pressure velocity (ω) and convective available potential energy (CAPE) were not conclusive (Chen, 2014). Therefore, we focus on LTS and RH_{ft} effects in this study. Figure 5 shows the histogram of LTS and RH_{ft} for two precipitation conditions. To define different meteorological conditions, we classified two regimes for LTS ($LTS > 12$ K and $LTS < 9$ K) and RH_{ft} ($RH_{ft} > 80\%$ and $RH_{ft} < 70\%$) respectively. Due to the complexity involved in precipitation processes, only non-precipitating clouds responses to AOD under different meteorological conditions are considered in Fig.6 and Fig.7. Figure 6 shows cloud property responses to AOD compared to LTS intensity. Generally, all cloud properties are higher when $LTS > 12$ K compare to $LTS < 9$ K condition. The R_e decreases with increased AOD (Twomey, 1974). The CF, LWP, COT and cloud thickness increase with increased AOD from 0 to 0.7. For $AOD > 0.7$, these parameters generally decreased with increasing AOD. Aerosols favor cloud growth under relatively unpolluted conditions. However, the cloud tends to dissipate at high pollution condition with higher aerosol concentrations. Figure 7 shows the cloud property responses to AOD as a function of RH_{ft} . As seen in Fig.7, cloud properties increase with increased AOD except for R_e . Under moist ($RH_{ft} > 80\%$) conditions, the cloud response to AOD is more rapid than under dry condition ($RH_{ft} < 70\%$). Cloud water tends to decrease when AOD is greater than 0.7 under dry conditions. This may be result from enhanced turbulent

entrainment of overlying dry air, which sometimes accompanies aerosol-cloud interactions and which promotes evaporation of cloud droplets (Ackerman et al., 2004). Besides the LWP, CF, COT and cloud thickness also show the same trend.

3.2 Aerosol-Cloud-Interaction as a function of dynamics

As discussed in Sect.3.1, LTS and RH_{ft} can play important roles in determining the effect of aerosols on cloud microphysical and macrophysical properties. In this section, the data are separated into different meteorological regimes based on LTS and RH_{ft} and on whether or not precipitation occurred. In this case, the response variable is the ACI, which is essentially the sensitivity of the cloud to variation in aerosol concentrations. The ACI index was calculated using COT/AOD binned by LWP for data within the 95% confidence interval to reduce the effect of outliers. The detailed meteorological conditions are described in the Table 3. Here, four dynamical conditions were chosen to investigate cloud responses to the aerosol: stable/dry, stable/wet, unstable/dry and unstable/wet. The criteria for defining these categories are shown in Table 3.

Figure 8 shows the ACI estimated under different meteorological conditions for non-precipitating and precipitating clouds. For non-precipitating clouds, ACI for unstable/wet conditions is much larger than for unstable/dry conditions. For unstable/dry conditions, stronger entrainment and a more rapid change in droplet size increase cloud top mixing with dry air above the cloud. Evaporation of the cloud droplets leads to a reduction in LWP (Ackerman et al. (2004). This tends to dissipate the stratus cloud and make it more like stratocumulus. However, cloud growth in the former case is stronger than cloud dissipation in the latter case, which is evidenced by the larger ACI. For non-precipitating

clouds, ACI under stable/wet conditions is larger than under stable/dry conditions. This is similar to unstable conditions except that the effect is weaker. Under stable conditions, the ACI is higher for precipitating than for non-precipitating clouds for both wet and dry conditions. The precipitating cloud is more sensitive to aerosols because precipitation suppression by aerosol-induced reduction in droplet size, which is less relevant in the non-precipitating case, can significantly increase the LWP and COT. In all cases, increasing the aerosol concentration tends to reduce droplet size. Under unstable conditions, cloud sensitivity to aerosols (ACI) is related to dynamics (entrainment at cloud top) while under stable conditions, the ACI is more strongly related to the potential for precipitation suppression.

3.3 ACI-CRF relationships and aerosol indirect forcing

The CRF was estimated for each eMAS scene using Eq.4 and is shown in Fig.9 as a function of ACI. The SW CRF encompasses a broad range from ~ -10 to $\sim -90 \text{ W m}^{-2}$. The SW CRF decreases dramatically as ACI increases from 0.02 to 0.32. The negative relationship denotes a cooling effect from the reflection of solar radiation back into space. The LW CRF ranges from ~ 3 to $\sim 14 \text{ W m}^{-2}$ as ACI increases from 0.02 to 0.32. The magnitude of LW CRF is much smaller than SW forcing. The positive value means that the LW CRF exerts a warming effect by trapping LW radiation, however this effect is weaker for low liquid water clouds than the cooling by the SW forcing because the cloud-top temperature is only slightly cooler than the surface. The TOA net CRF is obtained by adding SW and LW forcing. As shown in Fig.9 right panel, the TOA net CRF decreases as ACI increases. The net forcing ranges from ~ -8 to $\sim -81 \text{ W m}^{-2}$. This relationship

likely reflects the fact that ACI increases with the LWP of clouds as found for the scene analyzed in Fig.2.

The TOA SW and LW components of aerosol radiative forcing were estimated using methods described in Sect.2.3 and are reported in Table 4. The SW aerosol indirect forcing was estimated using Eq.5 and Eq.6. The radiative forcing related to the AIE was estimated for each eMAS scene. For all samples, the estimated intrinsic component of SW AIE forcing was -0.66 W m^{-2} . The magnitudes are higher than results from Lebsock et al. (2008) and Chen et al. (2014), who reported values of -0.42 W m^{-2} and -0.49 W m^{-2} , respectively. However, those studies focused on warm marine clouds, while this study focuses on warm continental clouds. The differences in estimated AIE forcing may be caused by: 1) abundance of aerosols over land are typically higher than over the ocean; 2) the albedo over land is higher than the albedo over the ocean. The extrinsic component of AIE was estimated to be -1.82 W m^{-2} . The extrinsic forcing is about three times larger than the intrinsic forcing. Note that the extrinsic component is directly related to the aerosol effect on cloud cover. As discussed in Sect.3.1, the observed agreement between CF and AOD can be related to large-scale dynamics. The LW component was estimated as 0.03 W m^{-2} for intrinsic AIE and 0.05 W m^{-2} for extrinsic AIE. Total LW forcing was positive but very small (less than 0.1 W m^{-2}) compared with SW forcing. Therefore, the LW warming effect is much smaller than the SW cooling effect.

4 Conclusions

The interactions among aerosol, cloud, precipitation, and environmental conditions are complex. In this study, remote sensing measurements from aircraft and satellite during

the SEAC⁴RS campaign over the southeastern US were used together to perform an analysis of the relationships among cloud and aerosol properties. The aerosol-cloud relationships and aerosol-cloud interaction index (ACI) were evaluated under different meteorological conditions. The top of atmosphere (TOA) cloud radiative forcing (CRF), and aerosol indirect forcing were also estimated using the same dataset.

Results show that non-precipitating and precipitating clouds have similar responses to aerosol loading but different magnitudes. Cloud R_e decreased as AOD increased for both types of clouds. However, the aerosol affected cloud R_e more for non-precipitating cloud than for precipitating clouds. Cloud LWP, COT, CF and cloud thickness generally increased with AOD for both cloud types. All cloud properties are higher when $LTS > 12$ K (or $RH_{ft} > 80\%$) compared to $LTS < 9$ K (or $RH_{ft} < 70\%$). The CF, LWP, COT and cloud thickness increase with increased AOD from 0 to 0.7. After that, these parameters generally decreased with increasing AOD. This indicates that aerosols favor cloud growth under relatively unpolluted conditions but are likely to dissipate cloud at high pollution condition, mainly due to enhanced entrainment of overlying dry air which evaporates cloud droplets.

Cloud responses to aerosol were highly affected by lower tropospheric stability (LTS) and free troposphere relative humidity (RH_{ft}). The ACI was generally higher under unstable, humid conditions and was lower under unstable, dry conditions. This was due to stronger entrainment of dry air above the cloud which increased mixing at cloud top, evaporating cloud droplets leading to a loss of cloud water. Under stable conditions, the ACI is higher for precipitating than for non-precipitating clouds because the former are

susceptible to precipitation suppression by aerosol-induced reduction in droplet size. The total TOA CRF was estimated to be -80 W m^{-2} when the ACI increased to 0.3. Clouds with greater LWP exhibit a greater ACI as well as stronger CRF. Aerosol indirect forcing of the estimated anthropogenic portion of the aerosol due to the intrinsic aerosol effect was estimated to be -0.63 W m^{-2} and the forcing due to the extrinsic aerosol effect was estimated to be -1.77 W m^{-2} . This demonstrates the strong radiative forcing associated with the aerosol indirect effect on cloud cover for the clouds observed during SEAC⁴RS.

Acknowledgments

We thank the NASA ER-2 scientists, flight crews, and support staff for their outstanding efforts

in the field campaign. SEAC⁴RS eMAS data are available at <https://ladsweb.modaps.eosdis.nasa.gov/missions-and-measurements/mas/>. CPL data are available at <http://cpl.gsfc.nasa.gov>. GOES data are available at <https://www-air.larc.nasa.gov/cgi-bin/ArcView/seac4rs?SATELLITE=1>. NAM reanalysis data are available at ftp://nomads.ncdc.noaa.gov/NAM/analysis_only/. E. M. Wilcox and L. Gao were supported by NASA grant NNX11AG89G. We appreciate Professor Douglas H. Lowenthal for comments and editing.

References

- Ackerman, A. S., Kirkpatrick, M. P., Stevens, D. E., and Toon, O. B.: The impact of humidity above stratiform clouds on indirect aerosol climate forcing, *Nature*, 432, 1014-1017 % @ 0028-0836, 2004.
- Baum, B. A., and Platnick, S.: Introduction to MODIS cloud products, in: *Earth science satellite remote sensing*, Springer, 74-91, 2006.
- Boucher, O., Randall, D., Artaxo, P., Bretherton, C., Feingold, G., Forster, P., Kerminen, V.-M., Kondo, Y., Liao, H., Lohmann, U., Rasch, P., Satheesh, S. K., Sherwood, S., Stevens, B., and Zhang, X.-Y.: Chapter 7: Clouds and Aerosols. In: *Climate Change 2013: The Physical Science Basis. Contribution of Working Group I to the Fifth Assessment Report of the Intergovernmental Panel on Climate Change* [Stocker, T.F., D. Qin, G.-K. Plattner, M. Tignor, S. K. Allen, J. Boschung, A. Nauels, Y. Xia, V. Bex and P.M. Midgley (eds.)], Cambridge University Press, Cambridge, United Kingdom and New York, NY, USA. Cambridge University Press, Cambridge, United Kingdom and New York, NY, USA, 2013.
- Bretherton, C. S., and Wyant, M. C.: Moisture transport, lower-tropospheric stability, and decoupling of cloud-topped boundary layers, *Journal of the Atmospheric Sciences*, 54, 148-167 % @ 1520-0469, 1997.
- Chen, Y.-C.: Satellite Estimate of Global Aerosol Indirect Forcing by Marine Warm Clouds, NCEO, 10.1038/ngeo2214
10.1038/NCEO2214, 2014.
- Chen, Y.-C., Christensen, M. W., Stephens, G. L., and Seinfeld, J. H.: Satellite-based estimate of global aerosol-cloud radiative forcing by marine warm clouds, *Nature Geoscience*, 7, 643-646 % @ 1752-0894, 2014.
- Doelling, D. R., Nguyen, L., Smith, W. L., and Minnis, P.: Comparison of ARM GOES-derived broadband albedos with broadband data from ARM-UAV and ScaRaB, 1998.
- Feingold, G., Eberhard, W. L., Veron, D. E., and Previdi, M.: First measurements of the Twomey indirect effect using ground-based remote sensors, *Geophysical Research Letters*, 30, n/a-n/a, 10.1029/2002gl016633, 2003.
- Grandey, B. S., Stier, P., and Wagner, T. M.: Investigating relationships between aerosol optical depth and cloud fraction using satellite, aerosol reanalysis and general circulation model data, *Atmospheric Chemistry and Physics*, 13, 3177-3184, 10.5194/acp-13-3177-2013, 2013.
- Hartmann, D. L., Ockert-Bell, M. E., and Michelsen, M. L.: The effect of cloud type on Earth's energy balance: Global analysis, *Journal of Climate*, 5, 1281-1304 % @ 1520-0442, 1992.

- Kaufman, Y. J., Koren, I., Remer, L. A., Rosenfeld, D., and Rudich, Y.: The effect of smoke, dust, and pollution aerosol on shallow cloud development over the Atlantic Ocean, *Proceedings of the National Academy of Sciences of the United States of America*, 102, 11207-11212, 10.1073/pnas.0505191102, 2005.
- Khain, A. P.: Notes on state-of-the-art investigations of aerosol effects on precipitation: a critical review, *Environmental Research Letters*, 4, 015004, 10.1088/1748-9326/4/1/015004, 2009.
- Klein, S. A., and Hartmann, D. L.: The seasonal cycle of low stratiform clouds, *Journal of Climate*, 6, 1587-1606 % @ 1520-0442, 1993.
- Klein, S. A.: Synoptic variability of low-cloud properties and meteorological parameters in the subtropical trade wind boundary layer, *Journal of climate*, 10, 2018-2039 % @ 1520-0442, 1997.
- Kobayashi, T.: Significant differences in the cloud droplet effective radius between nonprecipitating and precipitating clouds, *Geophysical Research Letters*, 34, 10.1029/2007gl029606, 2007.
- Latham, J., Rasch, P., Chen, C. C., Kettles, L., Gadian, A., Gettelman, A., Morrison, H., Bower, K., and Choulaton, T.: Global temperature stabilization via controlled albedo enhancement of low-level maritime clouds, *Philosophical transactions. Series A, Mathematical, physical, and engineering sciences*, 366, 3969-3987, 10.1098/rsta.2008.0137, 2008.
- Lebsock, M. D., Stephens, G. L., and Kummerow, C.: Multisensor satellite observations of aerosol effects on warm clouds, *Journal of Geophysical Research*, 113, 10.1029/2008jd009876, 2008.
- Levy, R. C., Mattoo, S., Munchak, L. A., Remer, L. A., Sayer, A. M., Patadia, F., and Hsu, N. C.: The Collection 6 MODIS aerosol products over land and ocean, *Atmospheric Measurement Techniques*, 6, 2989-3034, 10.5194/amt-6-2989-2013, 2013.
- McComiskey, A., Feingold, G., Frisch, A. S., Turner, D. D., Miller, M. A., Chiu, J. C., Min, Q., and Ogren, J. A.: An assessment of aerosol - cloud interactions in marine stratus clouds based on surface remote sensing, *Journal of Geophysical Research*, 114, 10.1029/2008jd011006, 2009.
- Meyer, K., Platnick, S., Arnold, G. T., Holz, R. E., Veglio, P., Yorks, J., and Wang, C.: Cirrus cloud optical and microphysical property retrievals from eMAS during SEAC(4)RS using bi-spectral reflectance measurements within the 1.88 μm water vapor absorption band, *Atmos Meas Tech*, 9, 1743-1753, 10.5194/amt-9-1743-2016, 2016.

- Minnis, P., Smith Jr, W. L., and Dp, G.: Cloud properties derived from GOES-7 for spring 1994 ARM intensive observing period using version 1.0. 0 of ARM satellite data analysis program, 1995.
- Penner, J. E., Xu, L., and Wang, M.: Satellite methods underestimate indirect climate forcing by aerosols, *Proceedings of the National Academy of Sciences*, 108, 13404-13408 % @ 10027-18424, 2011.
- Platnick, S., Meyer, K. G., King, M. D., Wind, G., Amarasinghe, N., Marchant, B., Arnold, G. T., Zhang, Z., Hubanks, P. A., and Holz, R. E.: The MODIS cloud optical and microphysical products: Collection 6 updates and examples from Terra and Aqua, *IEEE Transactions on Geoscience and Remote Sensing*, 55, 502-525 % @ 0196-2892, 2017.
- Quaas, J., Stevens, B., Stier, P., and Lohmann, U.: Interpreting the cloud cover – aerosol optical depth relationship found in satellite data using a general circulation model, *Atmospheric Chemistry and Physics*, 10, 6129-6135, 10.5194/acp-10-6129-2010, 2010.
- Remer, L. A.: The MODIS Aerosol Algorithm, Products, and Validation, *JAS*, 2005.
- Rosenfeld, D., and Gutman, G.: Retrieving microphysical properties near the tops of potential rain clouds by multispectral analysis of AVHRR data, *Atmospheric research*, 34, 259-283 % @ 0169-8095, 1994.
- Rosenfeld, D., Wang, H., and Rasch, P. J.: The roles of cloud drop effective radius andLWP in determining rain properties in marine stratocumulus, *Geophysical Research Letters*, 39, n/a-n/a, 10.1029/2012gl052028, 2012.
- Schwartz, S. E., Harshvardhan, and Benkovitz, C. M.: Influence of anthropogenic aerosol on cloud optical depth and albedo shown by satellite measurements and chemical transport modeling, *Proceedings of the National Academy of Sciences of the United States of America*, 99, 1784-1789, 10.1073/pnas.261712099, 2002.
- Sekiguchi, M.: A study of the direct and indirect effects of aerosols using global satellite data sets of aerosol and cloud parameters, *Journal of Geophysical Research*, 108, 10.1029/2002jd003359, 2003.
- Solomon, S.: *Climate change 2007-the physical science basis: Working group I contribution to the fourth assessment report of the IPCC*, Cambridge University Press, 2007.
- Tsay, S. C., Platnick, S., Yokota, T., Pincus, R., Wind, B., Ahn, M.-H., King, M. D., Gray, M. A., and Hubanks, P.: An initial analysis of the pixel-level uncertainties in global MODIS cloud optical thickness and effective particle size retrievals, 5652, 30, 10.1117/12.578353, 2004.
- Twomey, S.: Pollution and the planetary albedo, *Atmospheric Environment* (1967), 8, 1251-1256 % @ 0004-6981, 1974.

- Wilcox, E. M., Harshvardhan, and Platnick, S.: Estimate of the impact of absorbing aerosol over cloud on the MODIS retrievals of cloud optical thickness and effective radius using two independent retrievals of liquid water path, *Journal of Geophysical Research*, 114, 10.1029/2008jd010589, 2009.
- Wood, R., and Bretherton, C. S.: On the relationship between stratiform low cloud cover and lower-tropospheric stability, *Journal of Climate*, 19, 6425-6432 % @ 1520-0442, 2006.
- Xu, H., Xie, S.-P., and Wang, Y.: Subseasonal variability of the southeast Pacific stratus cloud deck, *Journal of climate*, 18, 131-142 % @ 1520-0442, 2005.

Table 1. List of data used in this study and which data can be used to solve specific questions

Platform	Target	Instrument/method	Variable	Spatial Resolution	Q1	Q2	Q3
Airborne remote sensing	Aerosol	eMAS	AOD (470, 550, 660 nm)	0.5 km	√	√	√
			AOD fine mode fraction		√	√	√
	Cloud	CPL	Layer AOD	0.2 km	√		
		eMAS	R _e		√	√	√
			LWP		√	√	√
			τ		√		
CTH/CTP	0.05 km		√				
Geostationary satellite	Cloud	GOES	CF		√		
			CTT		√		
			Cloud layer		√		
			CTH		√		
Reanalysis	Meteorology	NAM	CBH	4 km	√		
			Albedo				√
			T				√
			ω	12 km			√
			RH				√
			CAPE				√

Table 2. The slope of linear fit between cloud properties and aerosol, separated for non-precipitating and precipitating clouds. The sign indicates the relationship between variables.

	ln(AOD)	
	Non-precipitating	Precipitating
CF	0.04	0.06
R_e (μm)	-0.32	-0.13
COT	5.51	1.57
LWP (gm^{-2})	29.55	13.52
Thickness (km)	0.19	0.12

Table 3. Four conditions were defined to study aerosol-cloud relationships in different regimes.

	stable/dry	stable/wet	unstable/dry	unstable/wet
LTS (K)	< 9	< 9	> 12	> 12
RH_{ft} (%)	< 70%	> 80%	< 70%	> 80%
# of samples (Non-Precipitating)	399	428	632	697
# of samples (Precipitating)	68	125	179	422

Table 4. TOA aerosol indirect radiative forcing estimated for shortwave and longwave components from all samples. The radiative forcing was separated for intrinsic and extrinsic forcing.

Aerosol indirect forcing (W m^{-2})	AOD	
	Intrinsic	Extrinsic
TOA SW	-0.66	-1.82
TOA LW	0.03	0.05

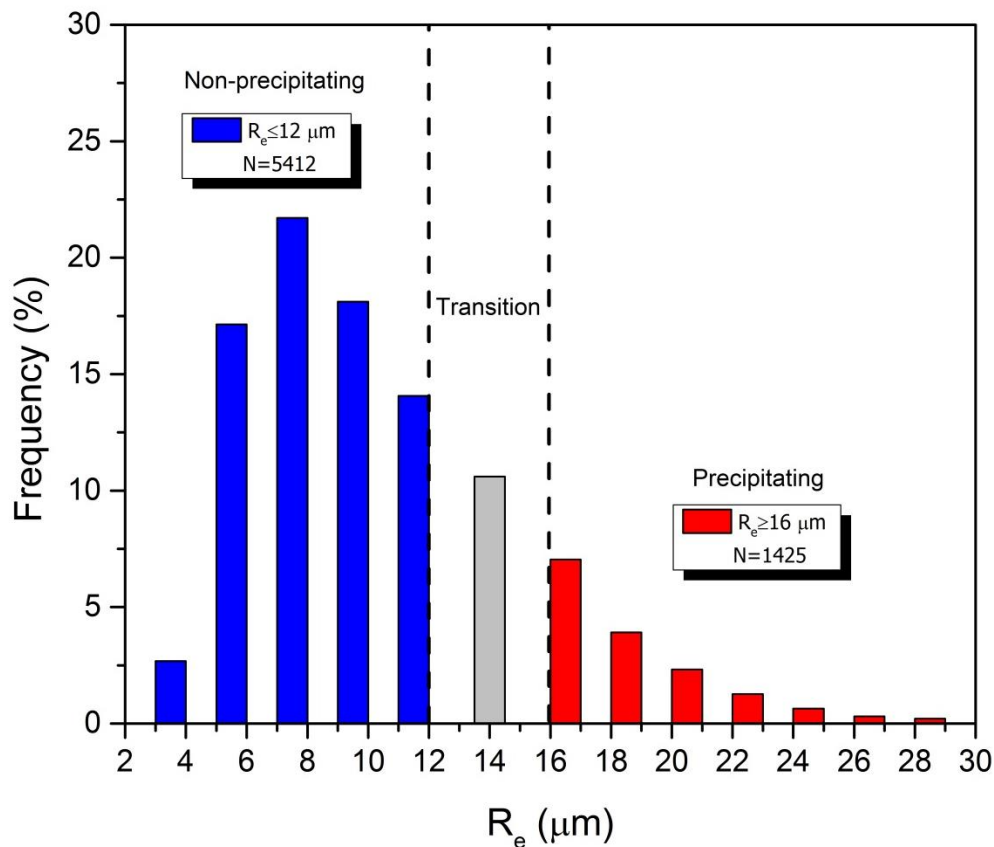


Figure 1. The histogram of cloud top effective radius and classification of non-precipitating ($R_e \leq 12 \mu\text{m}$, blue) and precipitating ($R_e \geq 16 \mu\text{m}$, red) clouds according to cloud top R_e . The transition clouds with R_e between 12 and 16 μm may be drizzling but not as strong as precipitating clouds. It is difficult to determine these clouds only by cloud top R_e . Therefore, we excluded these clouds in the analysis from controlling the data quality. N denotes the number of samples in each classification. The total number of samples in this analysis is 9076.

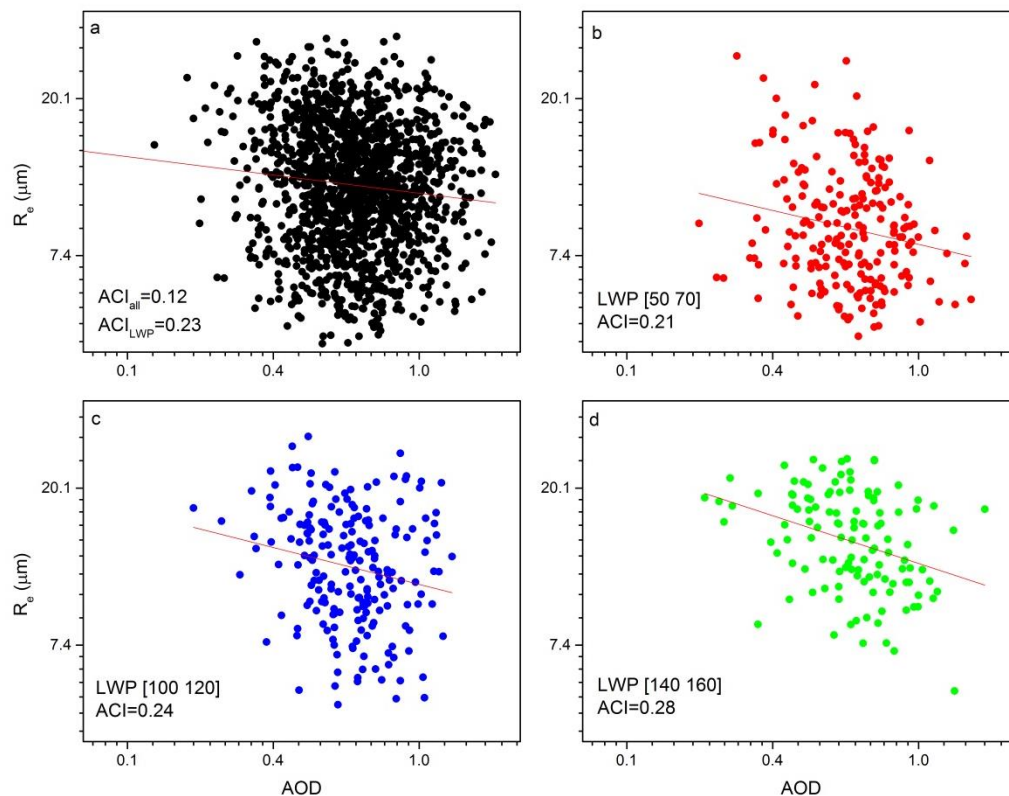


Figure 2. An example showing the differences in LWP constrained and unconstrained ACI for one eMAS scene. ACI calculated from (a) all data, and binned for a LWP range of (b) 50-70 g m^{-2} and (c) 100-120 g m^{-2} and (d) 140-160 g m^{-2} . The ACILWP in panel (a) denotes the averaged and LWP constrained ACI, while the ACI_{all} denotes the unconstrained ACI calculated directly from all dataset.

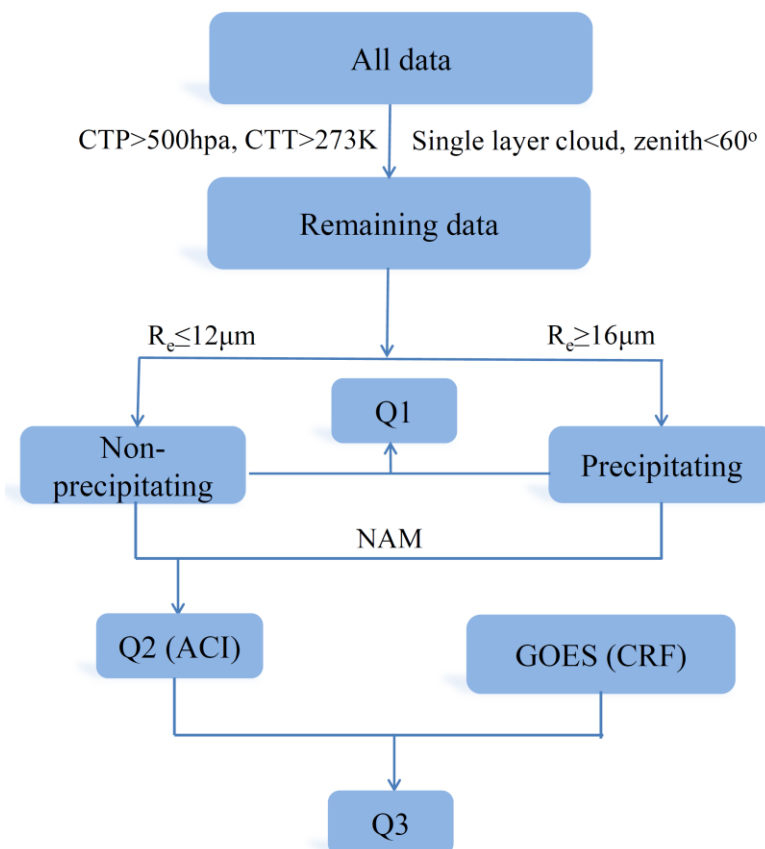


Figure 3. Flowchart of this study showing the steps to solve the research questions. The CTP, CTT, R_e represent cloud top pressure, cloud top temperature and cloud top effective radius. NAM represents the North American Mesoscale Forecast System reanalysis data.

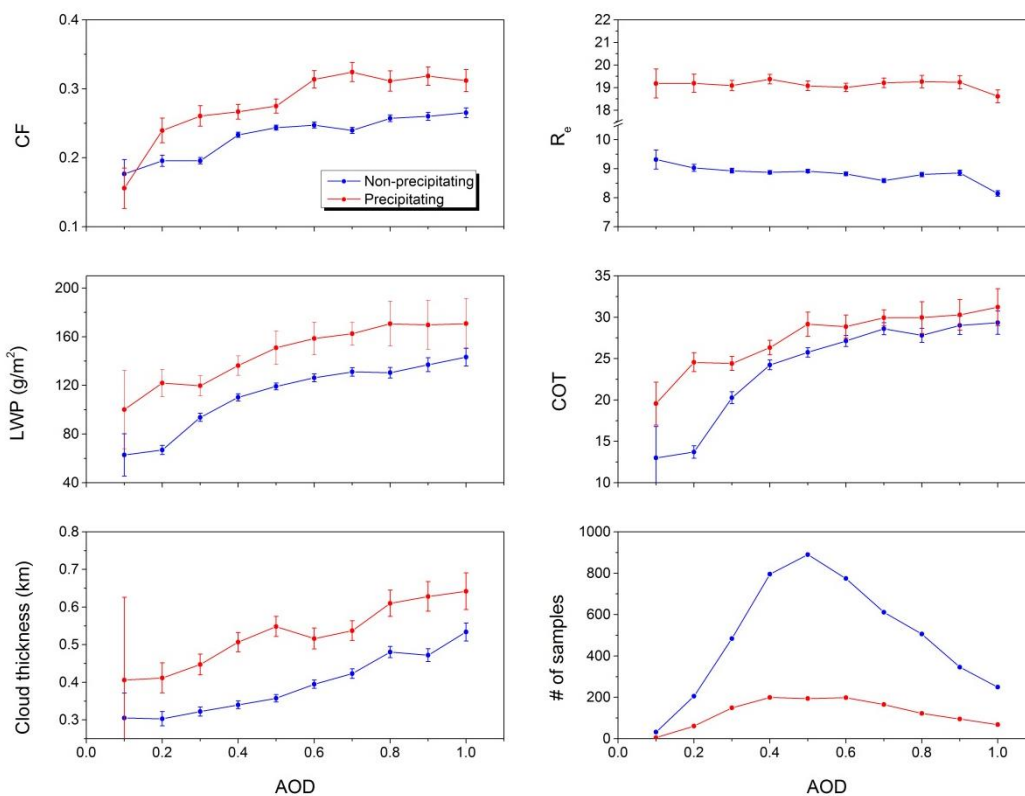


Figure 4. Cloud properties and number of samples as a function of each AOD bin. The points represent the mean value of cloud properties for each AOD bin and the bars on each point are the standard error of the cloud properties in each AOD bin. Cloud properties include cloud fraction (CF), effective radius (R_e), cloud liquid water path (LWP), cloud optical thickness (COT), cloud top/base height (CTH/CBH) and cloud thickness. Here, AOD was divided into 10 bins. The right bottom panel shows the number of samples in each AOD bin.

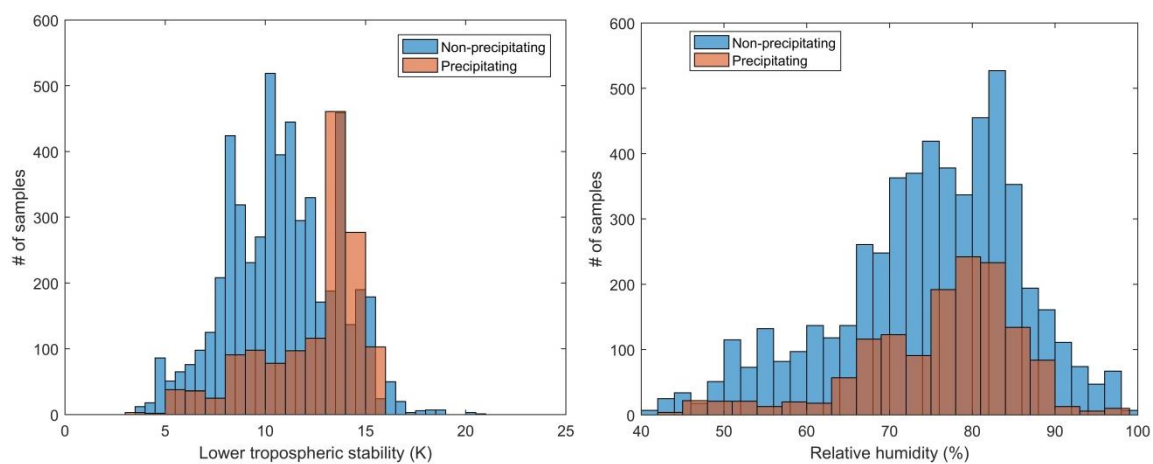


Figure 5. The histogram of lower tropospheric stability (LTS) and free troposphere relative humidity (RH_f) for two precipitation conditions.

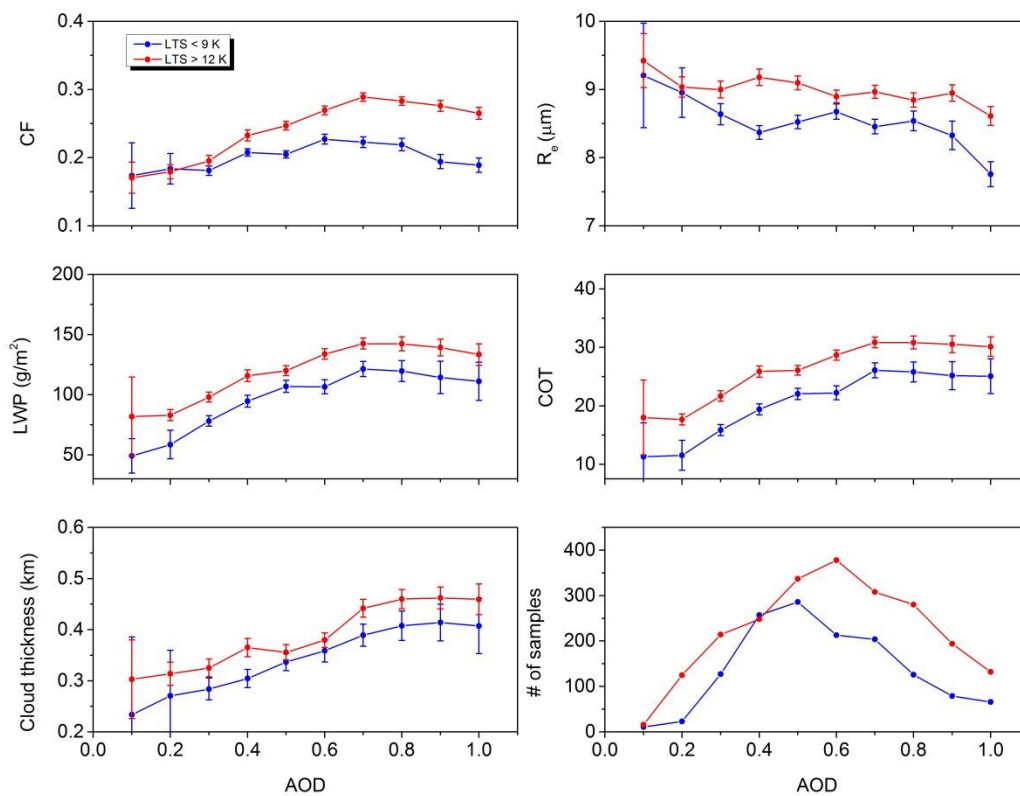


Figure 6. Similar to Fig.4, but the relationships between AOD and cloud properties (CF, R_e , LWP, COT, cloud thickness) were constrained by LTS and separated by higher LTS (>12 K, red) and lower LTS (<9 K, blue).

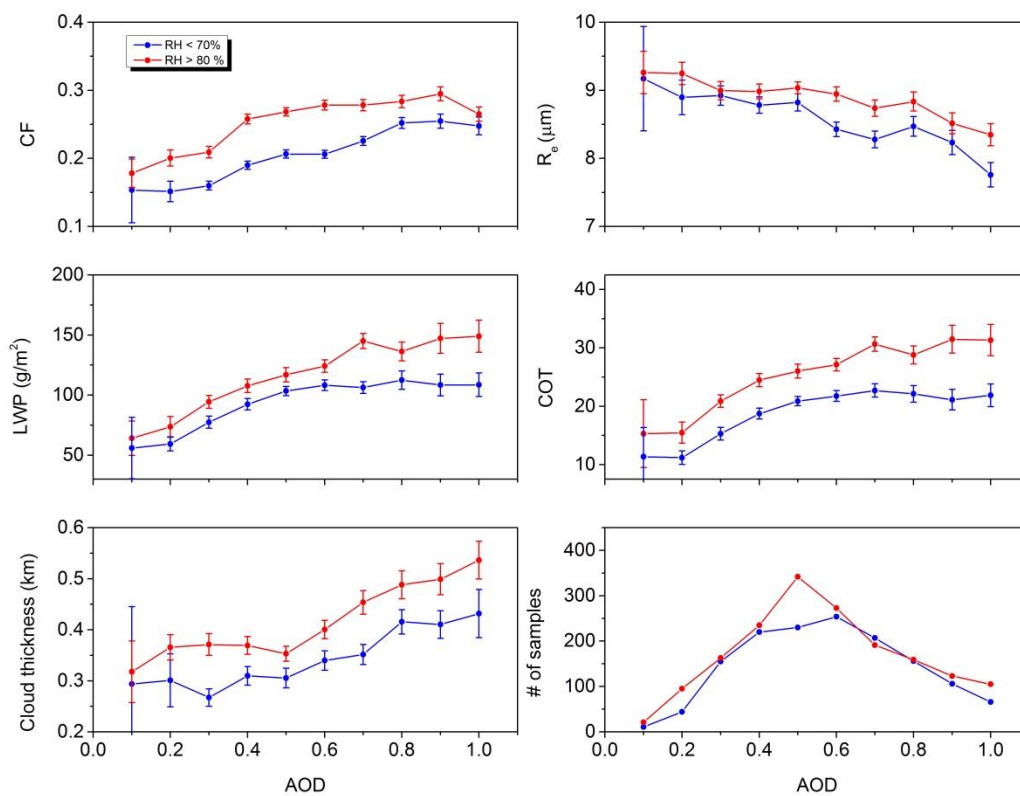


Figure 7. Similar to Fig.6, but the relationships between AOD and cloud properties (CF, R_e , LWP, COT, cloud thickness) were constrained by RH_{ft} and separated by higher RH_{ft} ($>80\%$, red) and lower RH_{ft} ($<70\%$, blue).

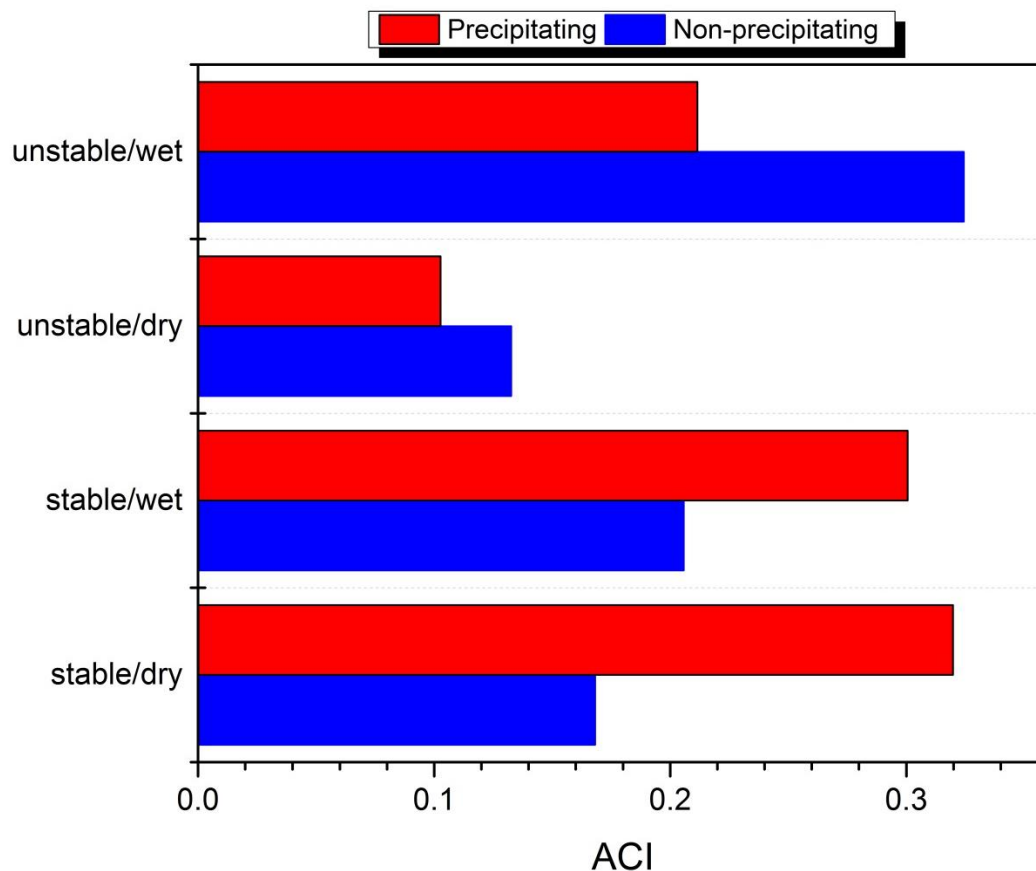


Figure 8. ACI calculated by using COT and AOD under four different meteorological conditions and separated by non-precipitating/precipitating conditions. Four meteorological conditions are unstable/dry, unstable/wet, stable/dry and stable/wet, which are determined by LTS and RH_{it} . ACI for non-precipitating/precipitating clouds is shown in blue and red, respectively. The ACI was calculated at the 95% confidence level.

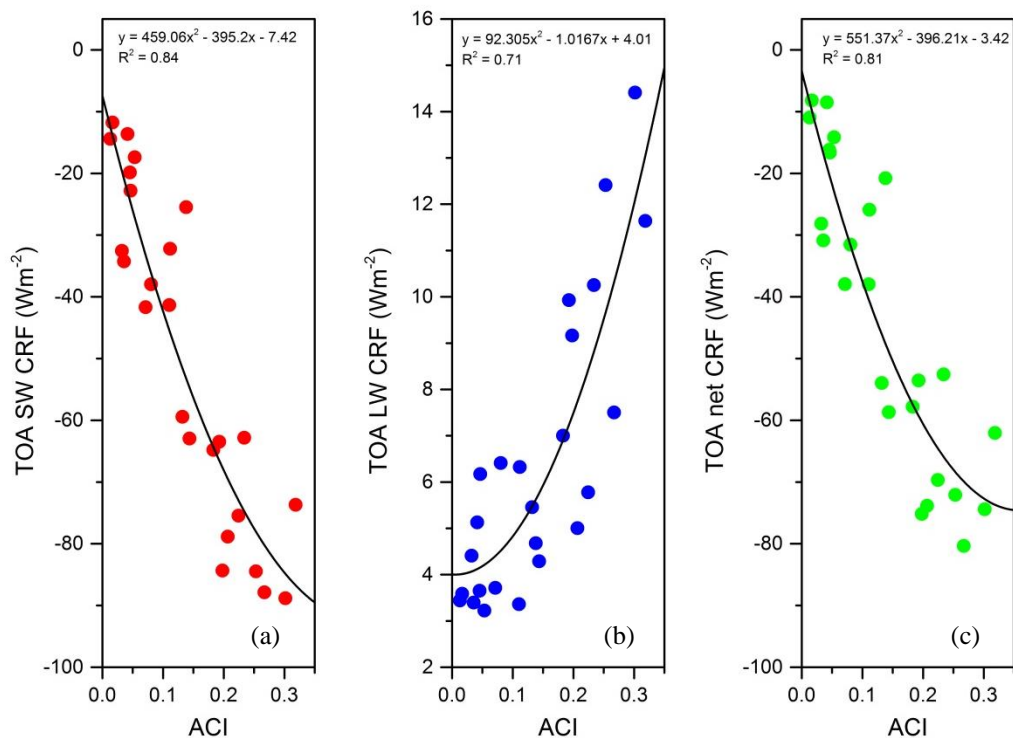


Figure 9. The TOA shortwave cloud radiative forcing (Panel a), TOA longwave cloud radiative forcing (Panel b) and TOA net cloud radiative forcing (Panel c) as a function of ACI. Each dot represents the mean forcing and ACI calculated for each eMAS scene. The best fitting and equation with R square are shown in the figure.

Chapter 4

Investigation of errors in quantifying the aerosol-cloud interactions

Lan Gao^{1,2}, Eric M. Wilcox¹, Robert C. Levy³, Steve Platnick³, Yunpeng Shan^{1,2}

¹Desert Research Institute, Reno, 89512, USA

²Atmospheric Sciences Graduate Program, University of Nevada Reno, 89557, USA

³Laboratory for Atmospheres, NASA Goddard Space Flight Center, Greenbelt, Maryland, 20771, USA

Correspondence to: Eric M. Wilcox (Eric.Wilcox@dri.edu)

To be submitted to: Atmospheric Chemistry and Physics

Abstract. The aerosol indirect effect continues to be a key component in climate forcing which is associated with large uncertainty. The issues causing this large uncertainty are partly due to our limited understanding of the physical process associated with the aerosol-cloud interaction (ACI) and partly due to challenges related to our measurements. An important component of this uncertainty derives from the use of multiple observational platforms at different spatial scales. Aerosol influences cloud properties at the microphysical scale, but observations are most often made over a wide range of spatial resolution. Aerosol-cloud interaction estimated from observations and models at the microphysical scale usually suggests a stronger aerosol indirect effect than do estimates from observations made at scales comparable to General Circulation Models (GCM) grid cell sizes. For future climate projections, it is critical to close this gap so we can understand the extent that anthropogenic aerosols have cooled the climate system. Despite decades of effort, satellite-based remote sensing as the primary source of global data for aerosol-cloud interactions remains a significant concern regarding how measurement artifacts affect retrievals of both aerosol and cloud properties. For example, the aerosol optical depth (AOD) retrieval is higher due to hygroscopic growth in humid air near a cloud field. Radiation scattered by clouds illuminates the nearby clear sky enhances the AOD retrieval without increasing the aerosol number concentration. However, these retrievals are routinely used in generating satellite-based estimates of aerosol-cloud interaction-induced radiative forcing. With the availability of high-resolution remote sensing data, in-situ aircraft data, and a Monte Carlo Radiative Transfer model developed in this study, the magnitude of the effects of variation of sampling scale and artifacts related to remote sensing retrievals on the estimated ACI were evaluated.

The ACI showed a strong scale-dependent behavior, which decreases as data resolution decreases. Smoothing of aerosol and cloud fields from 1 to 10 km produced a decrease of ~ 60% in estimated ACI. The ACI estimated from 1-km resolution remote sensing data was similar to that derived from in-situ aircraft measurements. Analysis of aircraft data revealed that the aerosol humidification effect accounts for a ~ 18.7-21.8% decrease in estimate ACI. The Monte Carlo model indicated that the three-dimensional (3-D) radiative transfer effect from cloud side multiple scattering reduced estimated ACI by ~ 10% for a broken cloud scene.

1 Introduction

Aerosol particles suspended in the air are crucial for Earth's climate system due to their interactions with radiation and clouds. Aerosol-cloud interactions (ACI) account for the largest uncertainty in the estimation of climate radiative forcing (Boucher et al., 2013a) and hamper prediction of future climate. Many studies have revealed differences in the response of cloud properties to changes in aerosol optical depth (AOD) based on observation and model simulations (Quaas et al., 2009; McComiskey and Feingold, 2012; Boucher et al., 2013b). The fundamental issues causing these differences are related in part to artifacts in satellite retrieval products and missing processes in General Circulation Models (GCMs) (Stevens and Feingold, 2009).

Biases in the estimation of aerosol-cloud interactions are related to the spatial scale at which observations are made (McComiskey and Feingold, 2012). ACI estimated from observations and models at the microphysical scale suggests that aerosol indirect radiative forcing is much stronger than ACI estimates derived from observations at spatial scales comparable to GCM grid cell sizes. An additional problem related to spatial scale is the misclassification of partly cloudy satellite pixels as the cloud-free clear sky, especially in areas of broken cloud.

Aerosol optical depth is a vertically integrated metric used to represent the amount of aerosol in the column. Its magnitude depends on aerosol mass loading and light scattering and absorption efficiencies that are related to aerosol size and chemical composition. AOD increases as particles absorb water vapor and their scattering cross section increases. This is a process that depends in part on the ambient relative humidity (RH) which

increases in humid environments near clouds (Twohy et al., 2009;Neubauer et al., 2017). The relationship between RH and aerosol light scattering was investigated by Li et al. (2001) and Tang, (1996). The hygroscopic growth factor (f) is defined as a function of RH as the ratio of the aerosol scattering coefficient at ambient RH (or an arbitrarily chosen high RH (e.g., ~80%) to the aerosol scattering coefficient under dry conditions, for example, at a low RH of ~40% (Jeong et al., 2007).

Three-dimensional (3-D) multiple scattering from cloud droplets at the sides of clouds is known to enhance the adjacent clear-sky reflectance, thus artificially increasing estimated AOD. A series of the papers discussed the 3-D radiation transfer effect (Várnai and Marshak, 2009;Davis and Marshak, 2010;Marshak et al., 2008;Wen et al., 2007). Here we exploit high-resolution airborne remote sensing data to expand on this previous work by considering a real 3-D clouds based on observations, and relating both the 3-D radiative effect and hygroscopic growth near clouds to the ACI. It is essential to evaluate the magnitudes of each of these potential biases in order to reduce errors in the estimation of the impact of aerosols and clouds on the Earth's climate system.

The purpose of this study is to evaluate the effects of biases related to the spatial scale of measurements, artifacts in remote sensing retrievals, and separating individual effects of aerosol humidification and 3-D radiative transfer on the magnitude of aerosol indirect radiative forcing. The errors in estimating the aerosol indirect forcing associated with those effects have not been systematically studied before. This analysis is facilitated by the availability of high-resolution remote sensing measurements from aircraft along with remote sensing measurements by satellite, a Monte Carlo Radiation Transfer model to

quantify the 3-D radiation effect, and direct measurement of the in-situ hygroscopic growth factor to quantify the aerosol humidification effect. The ultimate goal of this study is to evaluate the biases in the estimation of the ACI from remote sensing data.

2 Data, model, and methods

2.1 Data description

Table 1 lists the instruments and measurements along with sampling spatial resolutions used in this study. The primary data are enhanced MODIS airborne simulator (eMAS) retrieved aerosol and cloud properties (Table 1). The eMAS was deployed on a NASA ER-2 aircraft. The eMAS data were preliminarily filtered using criteria widely used for MODIS data (Levy et al., 2013; Baum and Platnick, 2006). This reduced the amount of data but ensured its quality. The remote sensing data were assigned uncertainties which were incorporated into the analysis. The AOD was retrieved from eMAS with the approach used for MODIS (Remer, 2005). AOD was used as a proxy for column cloud condensation nuclei (CCN). The Ångström exponent (\AA) was calculated based on the AOD at wavelengths of 0.55 μm and 0.66 μm . The \AA provides information on particle size; the larger the Ångström exponent, the smaller the particle. Cloud properties were also obtained from eMAS retrievals, including the number and types of cloud layers, cloud phase, cloud top temperature (CTT) and pressure (CTP), cloud fractional cover (CF), cloud top effective radius (R_e), cloud optical thickness (τ), and cloud liquid water path (LWP). To exclude ice and mixed-phase clouds from the analysis, warm liquid clouds were defined as those with eMAS-derived CTP and CTT greater than 500 hPa and

273 K, respectively. The cloud phase retrieval from eMAS was also used to screen out pixels where ice cloud was present.

Besides eMAS remote sensing data, this study also makes use of the Cloud Physics Lidar (CPL) which measured extinction profiles, the DC-8 aircraft in-situ aerosol properties (number concentration [N_a], single scattering albedo [SSA], asymmetry parameter [g] and hygroscopic growth factor [f]) and cloud properties (droplet number concentration [N_d], effective radius [R_e]), and satellite remote sensing data from MODIS including AOD, R_e , and cloud optical thickness (COT) retrievals. All aircraft data were synchronized to a common time scale with 1 Hz resolution and were spatially and temporally aligned with the remote sensing data (eMAS and MODIS). The full details of the measurements during the SEAC⁴RS campaign can be found in Toon et al. (2016).

2.2 Model design

A Monte Carlo Radiative Transfer (MCRT) model was developed for this study. The fundamentals of radiative transfer in a cloudy atmosphere can be found from Barker et al. (2003), Marshak and Davis (2005) and Mayer (2009). Figure 1 shows the flowchart of the MCRT model. The input for model simulation is based on the extinction profile measured from the CPL, and average observed aerosol and cloud properties from in-situ aircraft measurements. The model is designed to trace the trajectories of each photon from a radiation source (solar light) to termination due to absorption or escape from the domain. The Cartesian coordinate system and a cyclic boundary condition are employed. Table 2 lists the parameters used in the MCRT model.

The essential component of the Monte Carlo method is sampling from probability distribution functions (PDFs). To sample a quantity x_0 from a PDF $P(x)$, we need to invert the cumulative probability distribution (CPD), $\psi(x_0)$, which is the integral of $P(x)$:

$$\psi(x_0) = \frac{\int_a^{x_0} P(x) dx}{\int_a^b P(x) dx} \quad (1)$$

As x_0 ranges from a to b , $\psi(x_0)$ ranges from 0 to 1 in a uniform distribution (Kalos and Whitlock, 2008). Thus, to sample x_0 , we need to call a random number generator that samples from 0 to 1 uniformly and invert Eq.1 to get x_0 .

In the MCRT model, we need to sample the optical depth that a photon can travel freely before being absorbed or scattered. The probability that a photon can travel through an optical depth without any interactions is

$$P(\tau) d\tau = e^{-\tau} d\tau \quad (2)$$

Applying the cumulative probability distribution:

$$\psi(\tau) = \frac{\int_0^{\tau_0} e^{-\tau} d\tau}{\int_0^{\infty} e^{-\tau} d\tau} = 1 - e^{-\tau_{free}} = \varepsilon \quad (3)$$

Inverting this gives:

$$\tau_{free} = -\ln(1 - \varepsilon) = \int_0^L \sigma n dL \quad (4)$$

where the τ_{free} describes the optical distance that a photon can freely travel to the next extinction event, and ε is a random number uniformly distributed from 0 to 1. Expanding

τ by its definition, we can estimate the physical distance (L). σ and n are the cross section and number density of the particles, respectively.

In each simulation, the weight associated with a photon is initialized to 1 (unit weight). Subsequently, the weight is reduced at each scattering event to simulate partial absorption using $w_{\text{after}} = w_{\text{before}} \times \text{SSA}$, where w_{before} and w_{after} denote the weight of photon before and after interaction with a particle and SSA is the single scattering albedo of the particle. In reality, the photon cannot reduce its weight, but this computational method is used as a simplification to simulate the absorption. To save computational time, if the weight of a photon falls below a very small value (i.e., $w = 0.001$), the photon is terminated since it contributes nothing to the fluxes emerging from the boundaries of the domain. To simulate scattering, the Henyey-Greenstein (HG) phase function was used, since this is a popular approximation to the directionality of real scattering and widely used in models of particle scattering in the atmosphere (Barker et al., 2003). The phase function quantifies the probability that a photon is scattered from the previous direction of movement to a new direction. The HG phase function is given by:

$$P(\cos\Theta) = \frac{1 - g^2}{(1 + g^2 - 2g\cos\Theta)^{3/2}} \quad (5)$$

where g is the asymmetry parameter ($-1 \leq g \leq 1$), describing the degree of scattering in the forward direction. $g = -1$ indicates that all radiation is backward scattered like a mirror, $g = 1$ indicates that all radiation is forward scattered, and isotropic scattering (the same in all directions) is represented as $g = 0$. To implement the HG phase function in the Monte Carlo model, it is necessary to translate a uniformly distributed random number ϵ

into the corresponding value of $\cos \Theta$. This can be accomplished by setting up the following relationship:

$$\varepsilon = \int_{-1}^{\cos\Theta} P(\cos\Theta) d\cos\Theta = \int_{-1}^{\cos\Theta} \frac{1-g^2}{(1+g^2-2g\cos\Theta)^{3/2}} d\cos\Theta \quad (6)$$

and solving for $\cos\Theta$:

$$\cos\Theta = \frac{1}{2g} \left[1 + g^2 - \left(\frac{1-g^2}{1+g(2\varepsilon-1)} \right)^2 \right] \quad (7)$$

Using Eq.7, the scattering phase function can be implemented in the model. For air molecules, the Rayleigh phase function $p(\Theta) = \frac{3}{4}(1 + \cos^2\Theta)$ is used instead of the HG phase function. Once the photon's path crosses the boundary of the model domain, it is considered exited, and its contribution to the radiance is recorded.

To simulate radiation transfer in the 3-D cloud using the MCRT model, a 3-D cloud field must be constructed as the input for the model. Here we used observational data based on the eMAS and CPL retrievals. While eMAS provides a two-dimensional view of the properties of the top of the clouds, CPL provides vertical profiles of cloud. However, the CPL is only a nadir looking instrument, therefore this method extrapolates the cloud profiles measured with the CPL into off-nadir regions within the eMAS swath based on collocated measurement of eMAS and CPL. The method “clones” a CPL-measured cloud profile at an off-nadir pixel within the eMAS swath when the two pixels from eMAS and CPL have similar retrieved cloud properties. This is based on the assumption that the vertical cloud profile measured from CPL would be similar if the cloud properties obtained from the eMAS are similar. To achieve this, we first created a library of

collocated eMAS and CPL retrievals and then filled an off-nadir pixel of some eMAS cloud properties with a lidar profile in the library that has eMAS cloud properties best matching those of the off-nadir pixel. The cloud properties used to create the library are cloud optical thickness, cloud top effective radius and cloud top temperature, as shown in Fig.2. The eMAS cloud properties for each pixel were compared with those in the library to find the best-matched pixel. The best-match pixel was defined as follows:

$$\min\left\{\frac{(COT_p - COT_l)^2}{(\sigma_{l_{COT}})^2} + \frac{(Re_p - Re_l)^2}{(\sigma_{l_{Re}})^2} + \frac{(CTT_p - CTT_l)^2}{(\sigma_{l_{CTT}})^2}\right\} \quad (8)$$

where the subscript p represents the pixel, the subscript l represents the library, σ is the standard deviation, and min represents the minimum value. After determining the best-matched pixel, the corresponding cloud profile is then assigned to the off-nadir pixel. In this study, the size of the eMAS scene was used as the horizontal domain, and the top of the domain was set at 5 km to restrict the analysis to water clouds. The mean surface reflectance over each eMAS scene was used to reflect the photon once it hit the surface.

2.3 Methods

Figure 3 is a flowchart showing how the data were processed and which data were used to address specific issues. As noted above, the first issue is how the ACI depends on the spatial scale of the measurements. With the availability of high-resolution (50 m) eMAS data, the ACI can be calculated at larger spatial scales by aggregating the eMAS data from 1 km to 10 km (i.e., the MODIS analysis scale). First, collocated eMAS, MODIS and other aircraft data were selected from the SEAC⁴RS dataset. Second, the ACI was calculated at different scales by aggregating the eMAS data. Third, ACIs calculated from

eMAS, MODIS and aircraft in-situ data were compared to explore the ACI scale-dependent behavior.

The second problem is to identify how artifacts in the AOD retrieval for pixels near clouds can affect the ACI estimation. First, the distance (Δx) between each aerosol pixel and its nearest cloud retrieval from eMAS scene was calculated. Second, the AOD and Ångström exponent were sorted as a function of Δx , and the critical distance (Δx^*) was determined such that the mean AOD and Å did not change as Δx increased. This determines the range of a completely clear area from a cloud pixel. Third, data with Δx less than Δx^* were removed such that the remaining data were considered as the uncontaminated retrieval (not affected by e.g., aerosol humidification and 3-D radiative transfer). Finally, the reconstructed dataset was used to calculate ACI and compared with the results when including contaminated data. The difference can be considered as the error associated with the artifacts in the AOD retrieval. To maintain the volume of the dataset, the high-resolution pixel-scale cloud observations were paired to the nearest aerosol retrieval using only uncontaminated data within each eMAS scene. This results in a significant boost to the total number of samples used in the statistical analysis.

The final issue was to distinguish the effects of aerosol humidification and 3-D radiative transfer. For the aerosol humidification effect, aircraft in-situ measured RH and the particle hygroscopic factor (the ratio of humidified to dry extinction, here replaced by AOD: $f = \frac{AOD_{humidified}}{AOD_{dry}}$) were used to calculate AOD under dry conditions. Thus, the ACI is defined for dry conditions (ACI_{dry}). The contribution from aerosol humidification is then $\frac{ACI_{humidified} - ACI_{dry}}{ACI_{humidified}}$. To evaluate the 3-D radiative transfer effect, the MCRT

model was used to estimate cloud effects on clear sky reflectance following the method described in Wen et al. (2008). The difference in clear pixel TOA reflectance between a 3-D cloudy simulation (R_{cld}) and a cloudless simulation (R_{clr}) was considered as the cloud-enhanced clear sky reflectance due to cloud side multiple scattering: $\Delta R = R_{\text{cld}} - R_{\text{clr}}$. Once the enhancement of reflectance was calculated, the enhanced AOD and the contribution from the 3-D radiation effect was estimated.

3 Results and discussion

3.1 ACI spatial scale dependence

In the following analysis, we focus on one case (leg 9) using eMAS measurements on Aug. 30, 2013. Results from this and other cases are shown in Tables 3 and 4.

The eMAS data were aggregated from 1 km to 10 km and ACI was calculated over this spatial range. The results are shown in Fig.4. Calculated ACI was 0.3 at 1 km resolution but decreased to 0.11 at 10 km resolution. Thus, ACI decreases as spatial scale resolution decreases. Next, ACI calculated from in-situ aircraft data were compared to ACI calculated from satellite data (MODIS) when the two were collocated temporally and spatially. The aircraft derived ACI was 0.32 while the MODIS derived ACI was 0.12. The ACI derived from the in-situ aircraft data and the satellite remote sensing data represent the two extremes of the resolution range in this study. To further explore why ACI decreases as the spatial resolution of the data decreases, we used the homogeneity parameter (HP) (Barker, 1996; Wood and Hartmann, 2006).

The homogeneity parameter of a variable is defined as:

$$HP = \left(\frac{\mu}{\sigma}\right)^2 \quad (9)$$

where μ is the mean and σ is the standard deviation of the variable. To calculate the HP for ACI, HP was calculated for cloud and aerosol properties. Then, HP_{ACI} is defined as:

$$HP_{ACI} = \frac{HP_{cloud}}{HP_{aerosol}} \quad (10)$$

As shown in Fig.4, HP_{ACI} increases as spatial resolution decreases. The scatter plot in Fig.4 shows a linear relationship between ACI and HP. For different data resolutions, ACI and HP show a strong ($R^2 = 0.93$) inverse relationship.

The ACI- HP_{ACI} relationship implies that: 1) as spatial resolution decreases, HP_{ACI} increases; and 2) HP of cloud properties increases more rapidly than HP of aerosol properties as the data are aggregated to lower spatial resolution. Figure 5 further demonstrates how aggregating the data to lower spatial resolution increases the HP. Panel 1 of Fig.5 shows an example of an AOD scene at 0.5 km resolution. As the data are aggregated from panel 1 (AOD = 0.37 ± 0.22) to panel 7 (AOD = 0.37 ± 0.07), spatial detail in AOD is lost. However, while the mean AOD of this scene does not change (0.37), the standard deviation of AOD decreases dramatically. As the spatial resolution of AOD decreases, $HP_{aerosol}$ and HP_{cloud} both increase, but HP_{cloud} changes more rapidly than $HP_{aerosol}$, and HP_{ACI} increases. Decreasing the spatial resolution of the data leads to a large change in estimated ACI: ACI derived at 10 km resolution (0.1) was approximately 60% lower than ACI derived at 1 km resolution (0.3).

3.2 Aerosol near clouds

Figure 6 shows the shallow cumulus eMAS scene from leg 9 on Aug.30 2013. The cloud mask (cloud boundary) and AOD are plotted in Fig.6a and 6b, respectively. AOD near the cloud is generally higher, as shown in yellow color in Fig.6b. We calculated the distance from each aerosol pixel (clear sky) to its nearest cloud pixel and sorted AOD and \AA as a function of this distance (shown in Fig.7). Generally, AOD decreases as this distance increases while \AA increases as distance increases. Smaller \AA infers larger particle size. The higher AOD and smaller \AA near clouds may due to aerosol hygroscopic growth in the more humid air near the cloud. For this scene, the mean of both AOD and \AA do not change for distances greater than 4 km. Therefore, 4 km was chosen as the “critical distance” for this scene to identify contaminated aerosol retrievals. Aerosol retrievals with the distance to their nearest cloud pixel less than 4 km were flagged as a cloud-contaminated retrieval. Otherwise, aerosol pixels were flagged as uncontaminated retrievals. The separated data are shown in Fig.6c. The red data are cloud-contaminated (inaccurate) and the blue data are uncontaminated (accurate). Then the uncontaminated data (blue) and all data (red and blue) were used to calculate ACI. Note that, after filtering the data, only a small portion of uncontaminated data with respect to the all data was left for this scene. To maintain the original data volume, the aerosol-cloud pair method was used to re-create the dataset.

The approach for this method is to pair each cloud pixel to its nearest aerosol pixel and use the retrieval for this pixel to represent the aerosol most likely to influence the cloud pixel. Distances were computed between each cloud pixel and all possible aerosol pixel retrievals. Since we focus on shallow warm clouds in the broken cloud scene, the cloud fractional coverage is relatively low. Therefore, the aerosol pixels that are adjacent to the

cloud pixel are searched first (as there is a relatively higher probability that an aerosol retrieval is located in an adjacent pixel when the cloud coverage is lower). If an aerosol retrieval is not found in the adjacent pixels, this step is repeated until an aerosol target is found. By using this method, the computation time decreases dramatically. If two or more aerosol pixels are located at the same distance from the cloud pixel, then one is randomly selected.

After re-creating the aerosol and cloud data pairs, the uncontaminated original datasets were used to calculate the ACI, which is presented as a function of spatial resolution in Fig.8. Regardless which dataset was used, ACI decreased with decreasing resolution, as seen in Fig.4. The difference between contaminated (red) ACI and uncontaminated (blue) ACI is due to a combination of the humidification and 3-D effects discussed above. At 1 km resolution, as shown in Table 4 for case 1, the uncontaminated ACI is approximately 20% higher than contaminated (by the humidification and 3-D effects) ACI. From Table 4, the average enhancement in ACI resulting from accounting for these effects is 25%. Therefore, unless cloud-contaminated data are removed from the analysis, ACI derived from remote sensing measurements will be significantly biased low.

3.3 Aerosol humidification effect

The aerosol humidification effect can be described by the aerosol hygroscopic growth factor (f), which represents the increase in aerosol particle size due to absorption of water vapor as a function of RH. Tang (1996) and Akpootu and Gana, (2013) showed that the hygroscopic growth factor (f) increases with increasing RH and that this increase is most pronounced at 90-98% RH. Here, RH and the aerosol hygroscopic factor measured in-situ

aboard the aircraft were used to investigate the aerosol humidification effect. Figure 9a shows the profiles of RH and AOD above aircraft. The RH is higher in the boundary layer (below 3 km) with a maximum at ~1.5-2 km where the clouds form. AOD shows the similar profile (Fig.9b) with aerosol concentrated in the boundary layer. Thus, the humidification effect is likely to be strongest in this region of high aerosol concentration and high RH. Figure 9c shows the measured particle hygroscopic growth factor (f) as a function of RH. f increases as RH increases with a significant change observed when RH greater than 80%. A non-linear model was constructed to characterize the relationship between the f and RH, as shown in Fig.9c.

With the empirical relationship between the f and RH, f for any RH condition can be calculated. For each of the three eMAS scenes, we created the frequency histogram for clear sky RH as shown in Fig.10 for case 1. For this scene, the average RH for the highest and lowest 10% of RH are approximately 85 and 45%, respectively. These RH values were used to represent the maximum and minimum RH for this scene and to calculate the corresponding f for the two extreme RH conditions. According to the best fit function shown in Fig.9c, f was estimated as 1.043 at 45% RH and 1.396 at 85% RH for this scene. These two growth factors were used to evaluate the sensitivity of the ACI to aerosol humidification at high and low RH conditions, respectively. The results are shown in Table 4, case 1, which indicates that the estimated ACI under the maximum and minimum hygroscopic growth conditions were 0.26 and 0.247, respectively. Accounting for aerosol hygroscopic growth results in a ~ 8.3% and 2.9% increase in estimated ACI for high and low RH conditions, respectively, relative to ACI estimated for all (contaminated) data. Results from other selected scenes are also shown in Table 4.

Overall, the humidification effect contributes a ~ 4.9 to 8.9% increase in estimated ACI relative to all data estimated ACI. Since aerosol hygroscopic growth depends on aerosol chemical composition, the effect of hygroscopic growth on estimation of the ACI will vary for different aerosol populations.

3.4 Three-dimensional radiative transfer effect

The TOA reflectance was simulated using the MCRT model for two scenarios. One is the cloudless atmosphere containing only aerosols and gas molecules. The other is the 3-D cloudy atmosphere. To simulate the cloudless atmosphere, we used the CPL-measured molecular extinction profile for the entire eMAS scene and used the nearest clear sky extinction profile to fill the cloud pixel. To simulate the 3-D cloudy atmosphere, the “cloning” method described in section 2.2 was used. The difference between these two scenarios was considered to be the 3-D radiation effect. The enhancement of reflectance for clear sky pixels is shown in the Fig.11. There is reflectance enhancement (positive values) for most but not all clear sky pixels. This suggests that the 3-D radiation effect is not always responsible for increasing the clear sky reflectance. The negative values appear in the shadow side of the clouds and around optically thin clouds. The scene-averaged enhancement is ~ 0.019 according to previous studies (Wen et al., 2007; Wen et al., 1999; Kaufman et al., 1997). From this analysis, the mean enhancement of AOD from the 3-D effect is estimated as ~ 0.19. Based on the 3-D-corrected AOD, the estimated 3-D corrected ACI is 0.28 (Table 4, Case 1). Compared to the ACI calculated from original data (Table 4, ACI=0.24), accounting for the 3-D radiation effect increases the ACI by 16.7%. Including results from the other two cases in Table 4, accounting for the 3-D

effect increases the estimated ACI by an average of 21%, which represents a significant potential bias which must be accounted for in estimating the indirect aerosol radiative forcing.

4 Conclusions

The high-resolution remote sensing retrieved aerosol and cloud properties from eMAS aboard the ER-2 aircraft during the SEAC⁴RS campaign were used to derive the aerosol-cloud interaction index (ACI), which is a metric used to describe cloud responses to aerosol loading. ACI shows a strong scale-dependent behavior. It decreases as spatial resolution decreases. Estimation of the ACI using in-situ aircraft data is similar to ACI derived from eMAS data at 1 km resolution, but generally higher than ACIs derived using coarser resolution data. The MODIS-derived ACI is similar to eMAS derived ACI at 10 km resolution. This high-resolution remote sensing data demonstrates its ability to bridge the scale gap through data aggregation. 1-km resolution is sufficient to compare with in-situ measurements. The smoothing of aerosol and cloud fields may cause a large variation of estimated ACI which can be as high as 69% at 10 km resolution. It is therefore essential to account for biases arising from the spatial resolution of the data when estimating the aerosol-cloud interaction and associated radiative forcing.

To further investigate biases in the ACI arising from artifacts related to remote sensing retrievals, the effects of aerosol humidification and 3-D radiation transfer from the cloud sides were evaluated. A Monte Carlo Radiation Transfer model was constructed and used together with in-situ and remote sensing observations. The results show that the aerosol humidification effect (i.e., aerosol hygroscopic growth near cloud) accounts for an 18.7%

- 21.8% decrease in corrected estimated ACI. The magnitude of this effect depends on aerosol loading and its chemical composition. The effect should be larger for pollution-derived sulfate particles than for natural mineral dust. The 3-D radiative transfer effect enhances the reflectance in clear regions around broken clouds. The 3-D effect can cause about a ~ 10% difference in ACI for a broken cloud scene. Accounting for 3-D radiative effects in the regions near clouds is necessary for accurately estimating aerosol indirect effects on climate from satellite observations. Thus, one should be cautious in applying the 1-D approximation in frequently-used plane parallel radiative transfer models to compute clear-sky solar radiation in cumulus fields or using aerosol products derived from the 1-D approximation in aerosol indirect effect research.

The three cases selected for this study generally showed the same results. However, in the real atmosphere, aerosol and cloud properties change from scene to scene. Future work is needed to evaluate more cases over a wider range of conditions.

References

- Akpootu, D. O., and Gana, N. N.: The Effect of Relative Humidity on the Hygroscopic Growth Factor and Bulk Hygroscopicity of water Soluble Aerosols, *The International Journal Of Engineering And Science (IJES)*, 2, 48-57, 2013.
- Barker, H. W.: A parameterization for computing grid-averaged solar fluxes for inhomogeneous marine boundary layer clouds. Part I: Methodology and homogeneous biases, *Journal of the atmospheric sciences*, 53, 2289-2303 % @ 1520-0469, 1996.
- Barker, H. W., Goldstein, R. K., and Stevens, D. E.: Monte Carlo simulation of solar reflectances for cloudy atmospheres, *Journal of the atmospheric sciences*, 60, 1881-1894 % @ 1520-0469, 2003.
- Baum, B. A., and Platnick, S.: Introduction to MODIS cloud products, in: *Earth science satellite remote sensing*, Springer, 74-91, 2006.
- Boucher, O., Randall, D., Artaxo, P., Bretherton, C., Feingold, G., Forster, P., Kerminen, V. M., Kondo, Y., Liao, H., and Lohmann, U.: Clouds and aerosol-Climate change 2013: The physical science basis. Contribution of working group I to the fifth assessment report of the intergovernmental panel on climate change, 2013a.
- Boucher, O., Randall, D., Artaxo, P., Bretherton, C., Feingold, G., Forster, P., Kerminen, V. M., Kondo, Y., Liao, H., and Lohmann, U.: Clouds and aerosols, in: *Climate change 2013: The physical science basis. Contribution of working group I to the fifth assessment report of the intergovernmental panel on climate change*, Cambridge University Press, 571-657, 2013b.
- Davis, A. B., and Marshak, A.: Solar radiation transport in the cloudy atmosphere: a 3D perspective on observations and climate impacts, *Reports on Progress in Physics*, 73, 026801, 10.1088/0034-4885/73/2/026801, 2010.
- Jeong, M.-J., Li, Z., Andrews, E., and Tsay, S.-C.: Effect of aerosol humidification on the column aerosol optical thickness over the Atmospheric Radiation Measurement Southern Great Plains site, *Journal of Geophysical Research: Atmospheres*, 112, 10.1029/2006jd007176, 2007.
- Kalos, M. H., and Whitlock, P. A. X.: *Monte carlo methods*, John Wiley & Sons, 2008.
- Kaufman, Y. J., Tanré, D., Remer, L. A., Vermote, E. F., Chu, A., and Holben, B. N.: Operational remote sensing of tropospheric aerosol over land from EOS moderate resolution imaging spectroradiometer, *Journal of Geophysical Research: Atmospheres*, 102, 17051-17067, 10.1029/96jd03988, 1997.

- Levy, R. C., Mattoo, S., Munchak, L. A., Remer, L. A., Sayer, A. M., Patadia, F., and Hsu, N. C.: The Collection 6 MODIS aerosol products over land and ocean, *Atmospheric Measurement Techniques*, 6, 2989-3034, 10.5194/amt-6-2989-2013, 2013.
- Li, J., Wong, J. G. D., Dobbie, J. S., and Chýlek, P.: Parameterization of the optical properties of sulfate aerosols, *Journal of the atmospheric sciences*, 58, 193-209 % @ 1520-0469, 2001.
- Marshak, A., and Davis, A.: 3D radiative transfer in cloudy atmospheres, Springer Science & Business Media, 2005.
- Marshak, A., Wen, G., Coakley, J. A., Remer, L. A., Loeb, N. G., and Cahalan, R. F.: A simple model for the cloud adjacency effect and the apparent bluing of aerosols near clouds, *Journal of Geophysical Research*, 113, 10.1029/2007jd009196, 2008.
- Mayer, B.: Radiative transfer in the cloudy atmosphere, *The European Physical Journal Conferences*, 1, 75-99, 10.1140/epjconf/e2009-00912-1, 2009.
- McComiskey, A., and Feingold, G.: The scale problem in quantifying aerosol indirect effects, *Atmospheric Chemistry and Physics*, 12, 1031-1049, 10.5194/acp-12-1031-2012, 2012.
- Neubauer, D., Christensen, M. W., Poulsen, C. A., and Lohmann, U.: Unveiling aerosol–cloud interactions – Part 2: Minimising the effects of aerosol swelling and wet scavenging in ECHAM6-HAM2 for comparison to satellite data, *Atmospheric Chemistry and Physics*, 17, 13165-13185, 10.5194/acp-17-13165-2017, 2017.
- Quaas, J., Ming, Y., Menon, S., Takemura, T., Wang, M., Penner, J. E., Gettelman, A., Lohmann, U., Bellouin, N., and Boucher, O.: Aerosol indirect effects–general circulation model intercomparison and evaluation with satellite data, *Atmospheric Chemistry and Physics*, 9, 8697-8717 % @ 1680-7316, 2009.
- Remer, L. A.: The MODIS Aerosol Algorithm, Products, and Validation, *JAS*, 2005.
- Stevens, B., and Feingold, G.: Untangling aerosol effects on clouds and precipitation in a buffered system, *Nature*, 461, 607-613, 10.1038/nature08281, 2009.
- Tang, I. N.: Chemical and size effects of hygroscopic aerosols on light scattering coefficients, *Journal of Geophysical Research: Atmospheres*, 101, 19245-19250 % @ 12156-12202, 1996.
- Toon, O. B., Maring, H., Dibb, J., Ferrare, R., Jacob, D. J., Jensen, E. J., Luo, Z. J., Mace, G. G., Pan, L. L., Pfister, L., Rosenlof, K. H., Redemann, J., Reid, J. S., Singh, H. B., Thompson, A. M., Yokelson, R., Minnis, P., Chen, G., Jucks, K. W., and Pszenny, A.: Planning, implementation, and scientific goals of the Studies of Emissions and Atmospheric Composition, Clouds and Climate Coupling by Regional Surveys (SEAC4RS) field mission, *Journal of Geophysical Research: Atmospheres*, 121, 4967-5009, 10.1002/2015jd024297, 2016.

- Twohy, C. H., Coakley, J. A., and Tahnk, W. R.: Effect of changes in relative humidity on aerosol scattering near clouds, *Journal of Geophysical Research*, 114, 10.1029/2008jd010991, 2009.
- Várnai, T., and Marshak, A.: MODIS observations of enhanced clear sky reflectance near clouds, *Geophysical Research Letters*, 36, 10.1029/2008gl037089, 2009.
- Wen, G., Tsay, S. C., Cahalan, R. F., and Oreopoulos, L.: Path radiance technique for retrieving aerosol optical thickness over land, *Journal of Geophysical Research: Atmospheres*, 104, 31321-31332 % @ 32156-32202, 1999.
- Wen, G., Marshak, A., Cahalan, R. F., Remer, L. A., and Kleidman, R. G.: 3-D aerosol-cloud radiative interaction observed in collocated MODIS and ASTER images of cumulus cloud fields, *Journal of Geophysical Research: Atmospheres*, 112, n/a-n/a, 10.1029/2006jd008267, 2007.
- Wen, G., Marshak, A., and Cahalan, R. F.: Importance of molecular Rayleigh scattering in the enhancement of clear sky reflectance in the vicinity of boundary layer cumulus clouds, *Journal of Geophysical Research*, 113, 10.1029/2008jd010592, 2008.
- Wood, R., and Hartmann, D. L.: Spatial variability of liquid water path in marine low cloud: The importance of mesoscale cellular convection, *Journal of Climate*, 19, 1748-1764 % @ 1520-0442, 2006.

Table 1. Data used in this study from SEAC⁴RS campaign and selected to answer the objectives of this study: (a) Investigate biases from the spatial scale of measurements; (b) Investigate biases from artifacts in remote sensing retrievals; (c) Investigate biases from aerosol humidification and 3-D radiative transfer effect.

Platform	Method	Variable	Resolution	(a)	(b)	(c)
Airborne remote sensing	eMAS	AOD	500 m	√	√	√
		Å			√	√
		R _e (μm)		√	√	√
		LWP (g m ⁻²)		√	√	√
		CTP (hPa)	50 m	√		
		CTT (K)				√
	COT		√		√	
	CPL	Layer AOD	200 m	√		√
		Extinction (m ⁻¹)				√
	Satellite remote sensing	MODIS	AOD	10 km	√	
R _e (μm)			1 km	√		
COT				√		
Aircraft in-situ	Cloud probe	N _d (cm ⁻³)	1 sec	√		
		R _e (μm)		√		
	Aerosol probe	N _a (cm ⁻³)		√		
		SSA	1 sec			√
		g				√
	4STAR	AOD above aircraft	1 sec	√		√
	Meteorology probe	RH	1 sec			√

Table 2. The parameters used in MCRT simulation and the sources of those variables. Here ‘scene’ represents each simulated eMAS scene.

Parameters	Sources
# of photons	10,000,000
Zenith/azimuth angle	Mean over eMAS scene
Molecular extinction	Molecular extinction profile from CPL
Aerosol extinction	Clear sky extinction profile from CPL
Cloud extinction	Cloud extinction profile from CPL
Weight of photon	1
SSA	Mean of aircraft in-situ data
Phase function	Henye-Greenstein for particle
	Rayleigh for molecule
Domain	Scene length \times scene width \times 5 km height

Table 3. Comparison of ACI calculated from aircraft, eMAS, and MODIS at different resolutions. The R^2 of ACI and HP was shown in this table. The differences of ACI due to smoothing data from 1 km to 10 km, and due to artifactual retrieval were calculated. The red color represents ACI calculated using all data, and the blue data represents the ACI calculated using uncontaminated data.

Case	aircraft	eMAS (1 km)		eMAS (10 km)		MODIS (10 km)	R^2 of ACI-HP	Smooth	Artifactual retrieval (1 km)
		uncontaminated	all	uncontaminated	all				
1	0.32	0.3	0.24	0.11	0.05	0.12	0.93	63.30%	20%
2	0.17	0.16	0.11	0.05	0.03	0.04	0.87	68.70%	31.30%
3	0.25	0.28	0.21	0.17	0.09	0.13	0.91	39.30%	25%

Table 4. Comparison of ACI calculated using contaminated and uncontaminated data. Variations of ACI caused by aerosol humidification effect and 3-D radiation transfer effect were also shown in this table. Red color represents ACI calculated using maximum hygroscopic growth factor, and blue color represents ACI calculated using minimum hygroscopic growth factor.

Case	Uncontaminated	Humidification effect		3-D radiation transfer effect	Contaminated
		High RH	Low RH		
1	0.3	0.26	0.247	0.28	0.24
2	0.16	0.12	0.118	0.14	0.11
3	0.28	0.23	0.22	0.25	0.21
Average contribution	-	18.7%	21.8%	10.10%	-

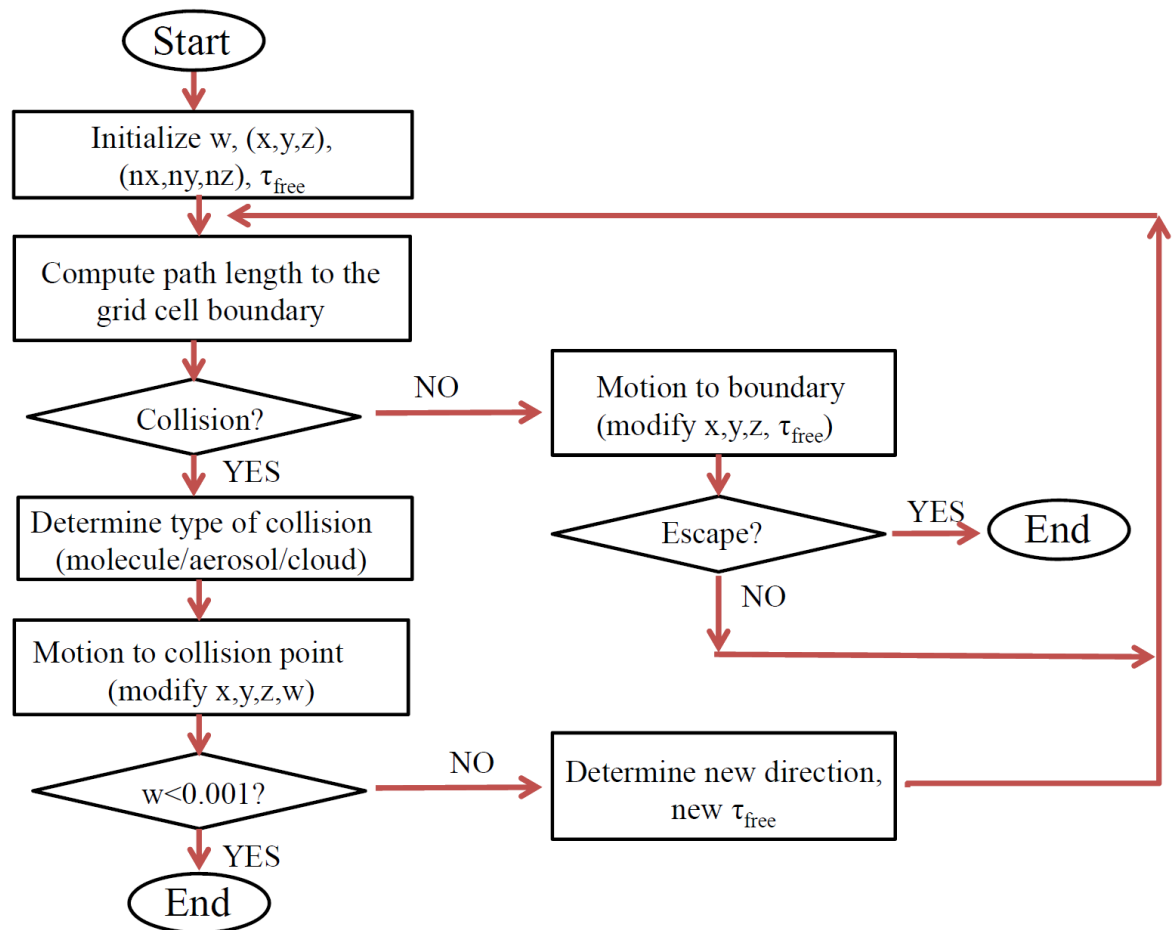


Figure 1. The algorithm flowchart for the Monte Carlo Radiative Transfer model used in this study. Here w represents the photon weight, (x, y, z) represents the position of the photon, (n_x, n_y, n_z) represents the direction of movement, τ_{free} represents the free optical path that a photon can travel without any interactions.

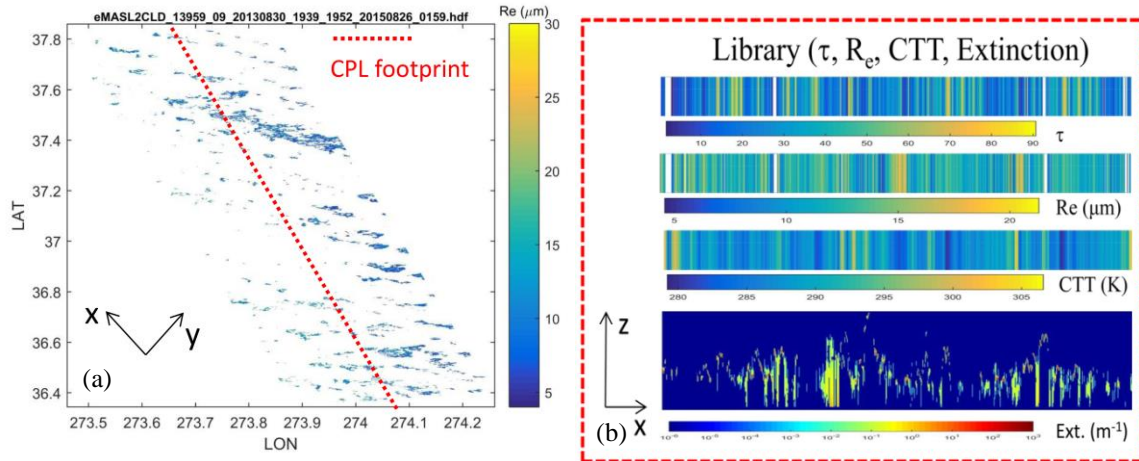


Figure 2. Example of constructing three-dimensional cloud field using collocated CPL and eMAS data. Data obtained from eMAS measurement on Aug. 30 2013 (leg 9). CPL footprint overlay on eMAS image (Panel a). The library (Panel b) of cloud optical thickness, effective radius, cloud top temperature and extinction profiles used to compare with the off-nadir pixel from eMAS retrieval.

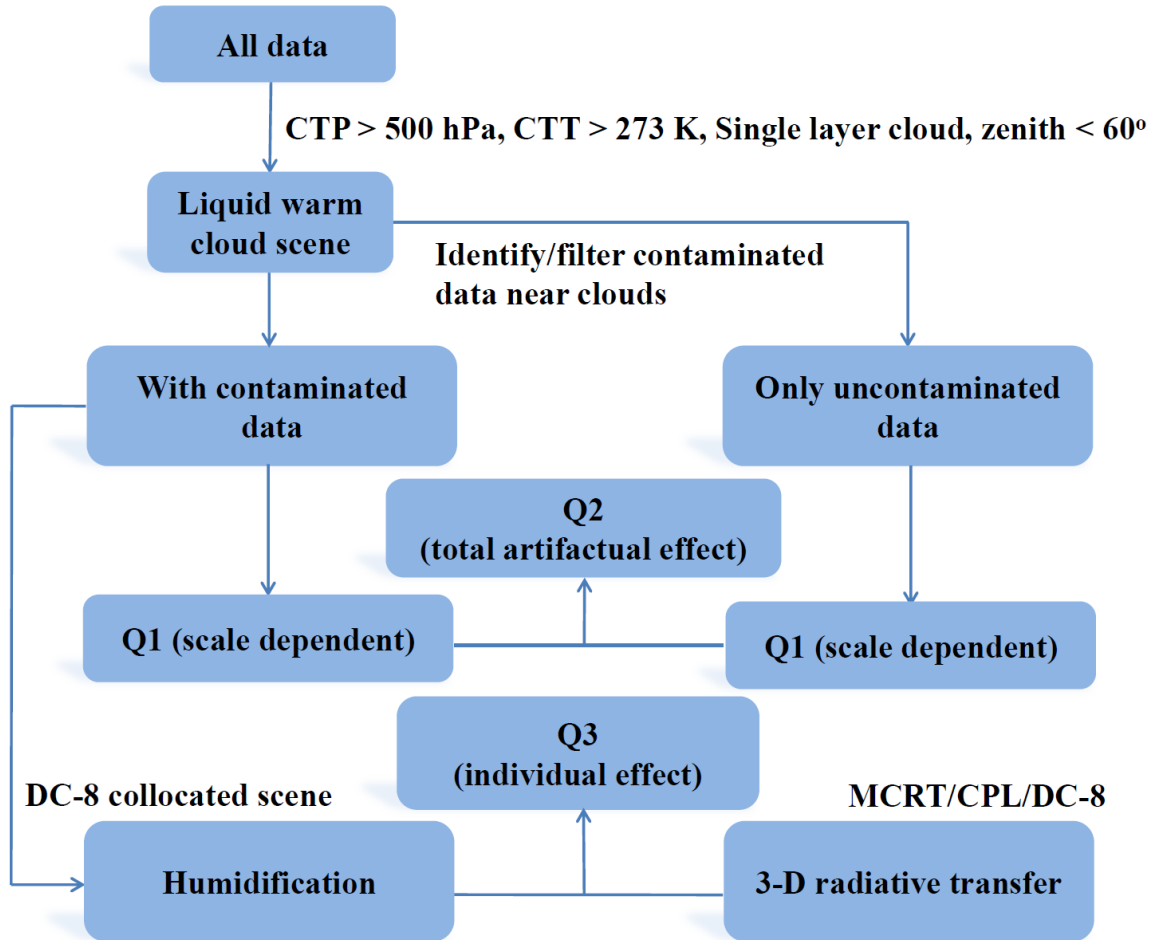


Figure 3. Flowchart of this study showing the steps to solve the research questions.

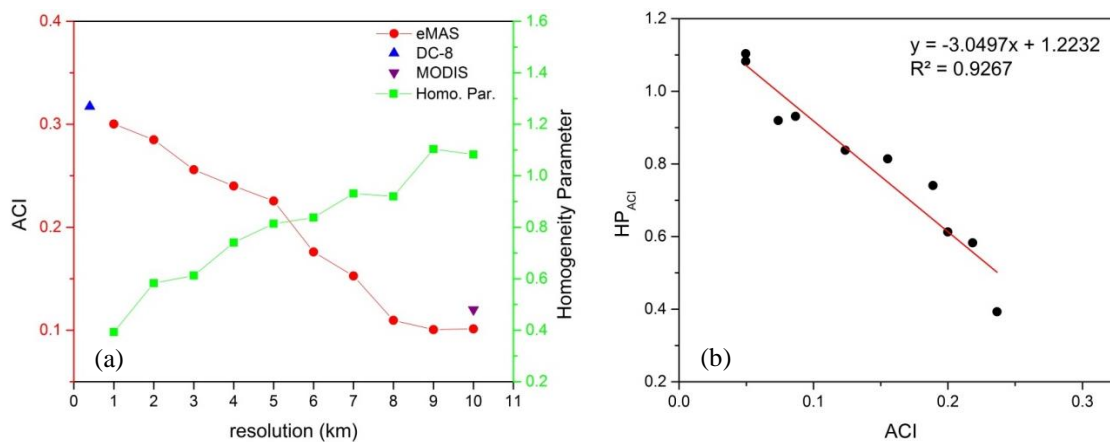


Figure 4. The ACI calculated from eMAS (red), MODIS (purple) and aircraft (DC-8, blue), as well as the homogeneity parameter (green) as a function of data resolution ranging from 1 km to 10 km (Panel a). The linear relationship between eMAS derived ACI and homogeneity parameter calculated using Eq. 10 (Panel b).

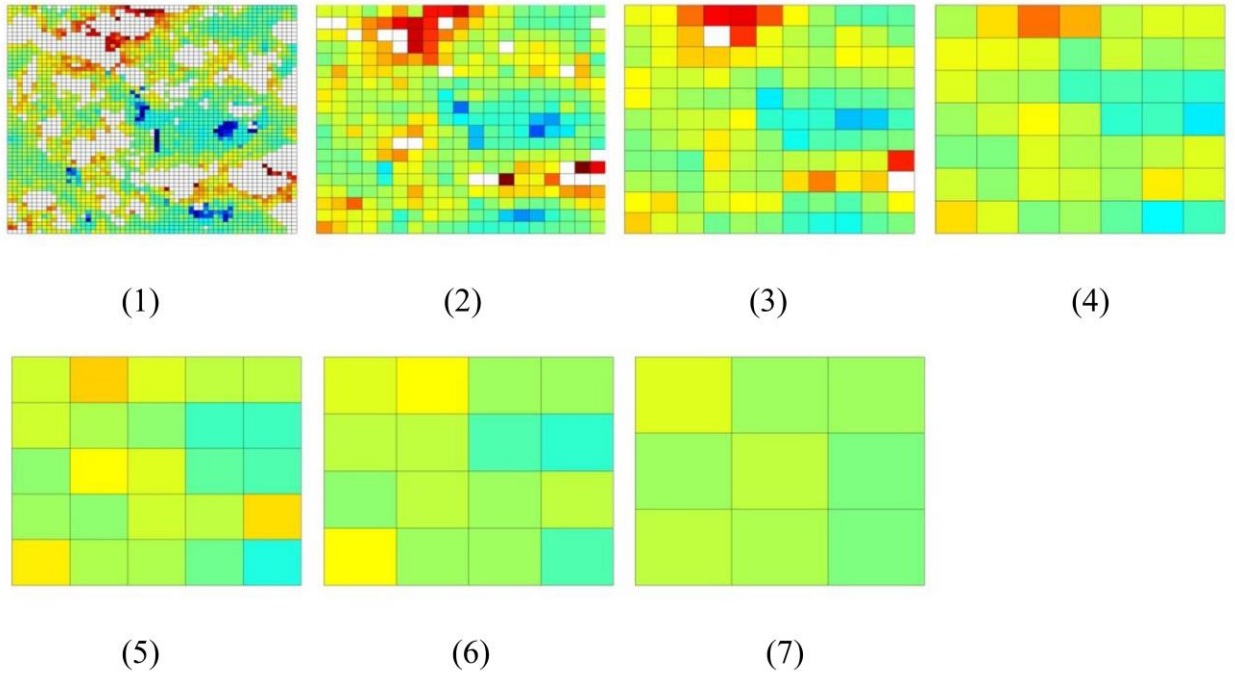


Figure 5. An example scene where AOD (aerosol optical depth) was aggregated from 0.5 km to 10 km resolution (from panel 1 to panel 7). This process significantly smoothed out the signal of AOD, reducing the standard deviation of AOD without changing its mean.

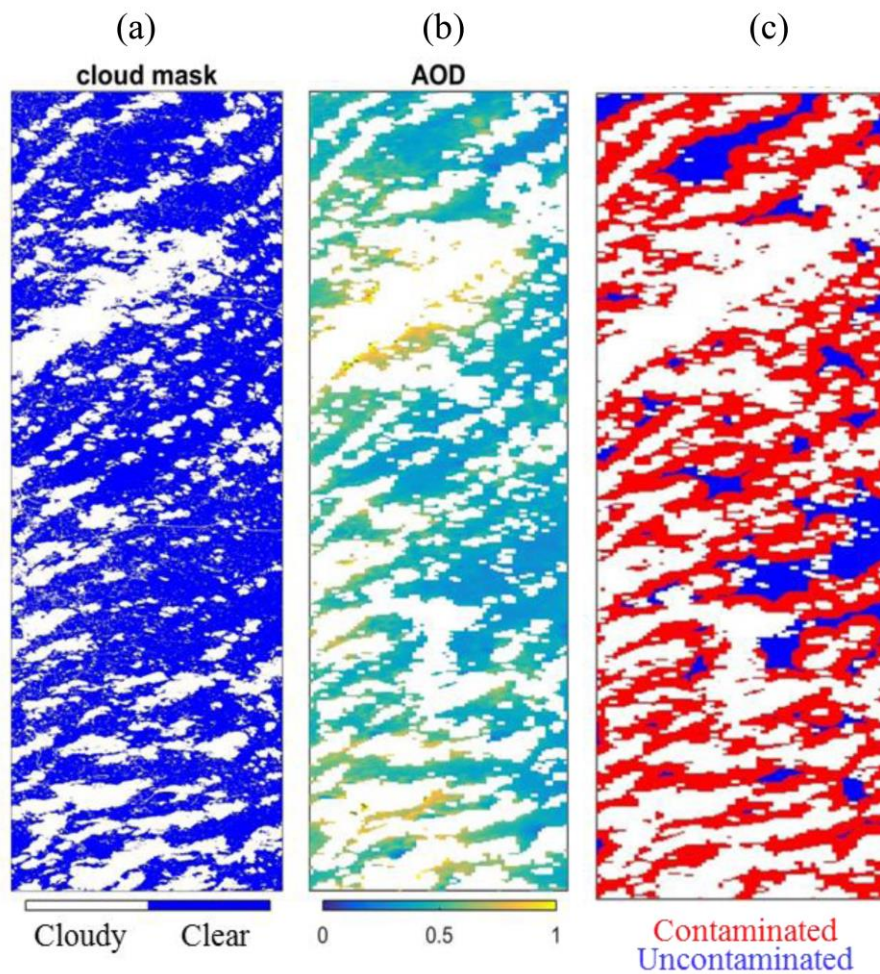


Figure 6. eMAS image of cloud mask (Panel a) on the 30 Aug 2013. Coinciding aerosol optical depth retrieved from eMAS (Panel b). Separated contaminated (red) and uncontaminated (blue) aerosol retrievals (Panel c) determined by using the 4 km critical distance for this scene.

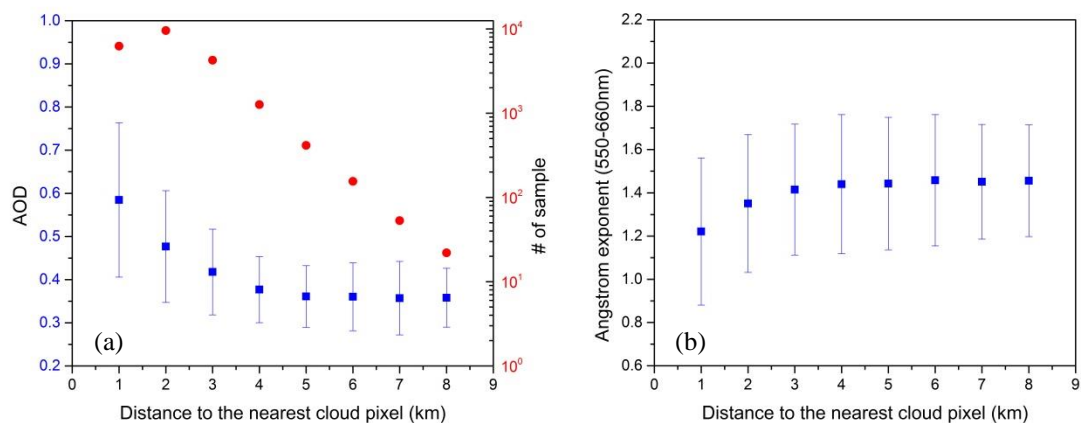


Figure 7. AOD (Panel a) and Angstrom exponent (Panel b) as a function of the distance from each aerosol pixel to its nearest cloud pixel. The blue squares represent the mean of AOD/ \AA in each distance bin. Blue bars represent the standard deviation of AOD/ \AA . Red points represent number of samples in each bin.

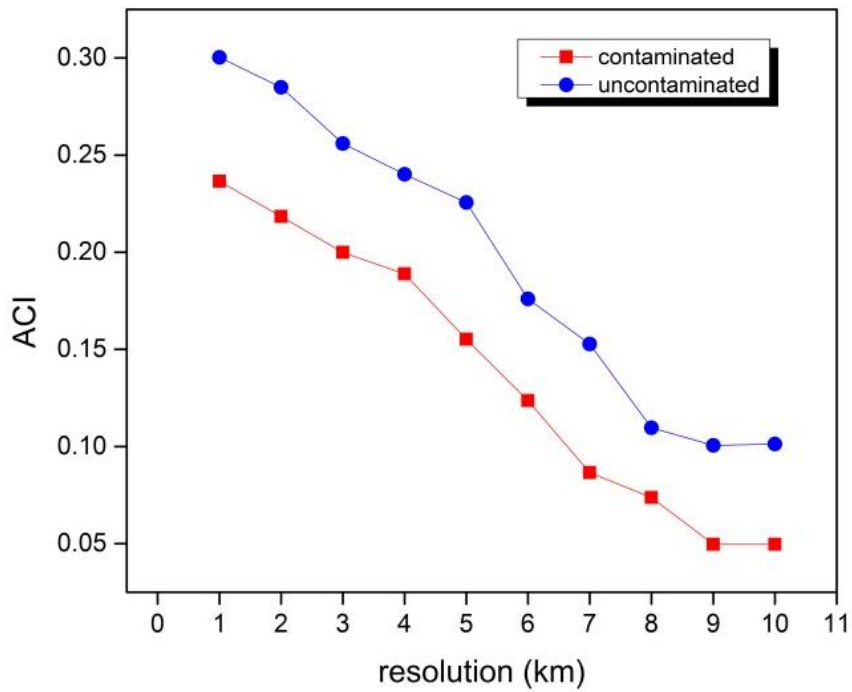


Figure 8. ACI calculated using all data (red, contaminated) and uncontaminated (blue) data with resolution aggregated from 1 km to 10 km.

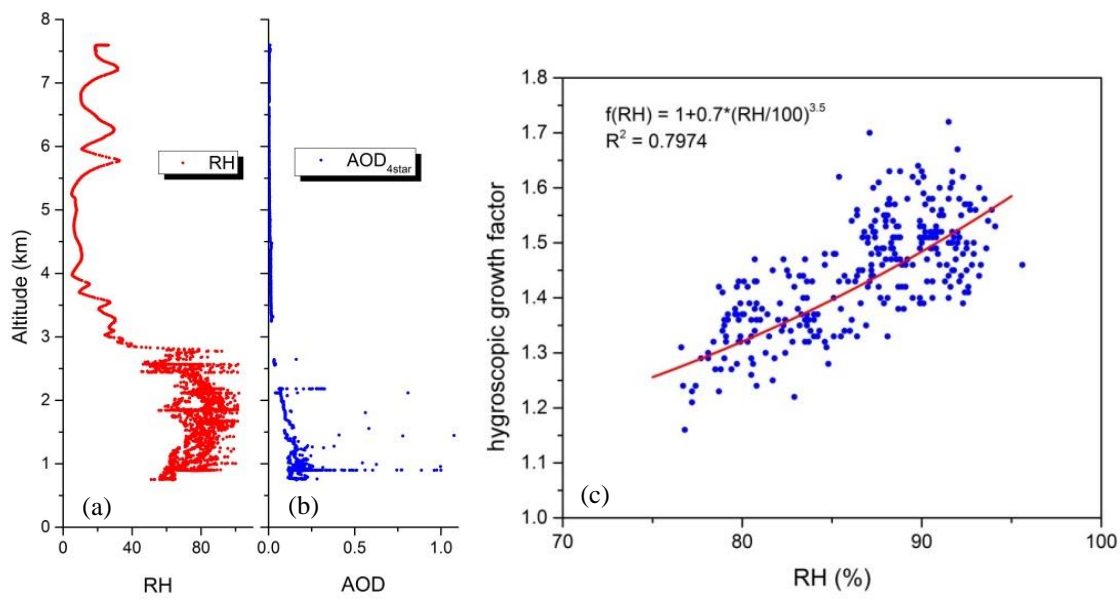


Figure 9. Profiles of RH and AOD (Panel a and b) measured from DC-8 aircraft. Aerosol hygroscopic growth factor as a function of RH (Panel c). The AOD profile was obtained from 4STAR which was installed on the top of aircraft and measures the AOD above the aircraft.

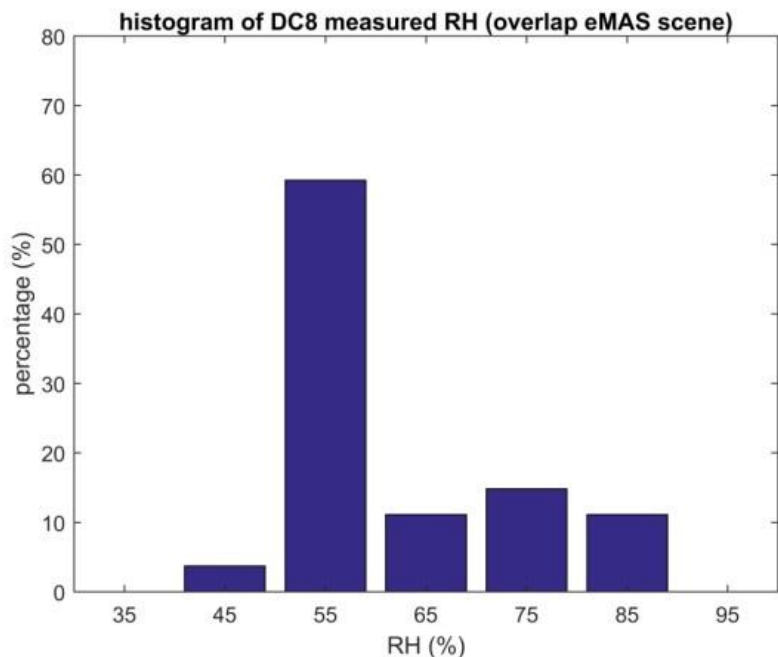


Figure 10. Frequency distribution (%) of DC-8 aircraft in-situ measured clear sky RH. In this figure, only clear sky data points are included. To determine the clear sky measurement, we first checked the cloud droplet number concentration and liquid water content sampled from the cloud probe. If cloud probe shows there is no cloud droplet in the sample, and then we classify the measured RH for clear sky, otherwise, we classify as cloudy sky.

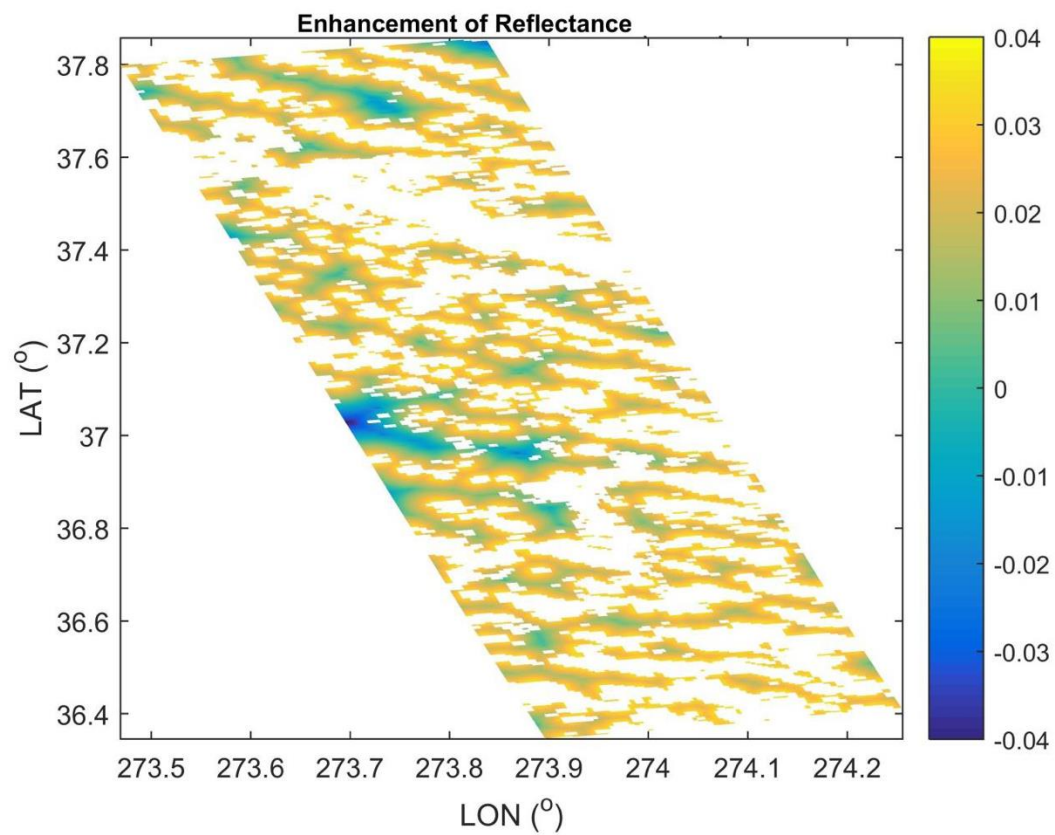


Figure 11. The enhancement of TOA reflectance for clear sky pixels only simulated from MCRT model. The color bar represents the magnitude of enhancement.

Chapter 5

Summary, conclusions and future work

1 Summary and conclusions

Aerosols play a critical role in the climate system. A change in aerosol properties may directly impact atmospheric radiation and also lead to a change in the microphysical and radiative properties of clouds, thus directly and indirectly influence the Earth's climate. The interactions among aerosol, cloud, precipitation, and meteorological conditions are complex and sometimes enhance or offset with each other making them even more mystery. This complexity hampers our understanding of the climate response to anthropogenic activity and causes the largest uncertainty in climate prediction.

Three primary objectives of this work aiming to contribute to this field are: 1) deepen our understanding of how cloud responses to aerosol loading; 2) examine the variation of aerosol-cloud interactions (ACI) over a wide range of meteorological conditions and the subsequent regional radiative forcing; 3) investigate the errors in quantifying the ACI from remote sensing observations. We have been fortunate of having several major modes of information to work with: data from the Cloud Aerosol Radiative forcing Dynamics EXperiment (CARDEX) campaign, data from the Studies of Emissions and Atmospheric Composition, Clouds and Climate Coupling by Regional Surveys (SEAC⁴RS) campaign, data from satellite, and a Monte Carlo Radiation Transfer (MCRT) model designed by the author. The information from any one of these platforms is useful for recognizing specific parts of the ACI as demonstrated by the vast number of papers that define and derive aerosol indirect effect (AIE) using one data source. However, the integration of all those data is more powerful and allows us to gain confidence in our results and ensuing interpretations, but full of difficulties. It requires an understanding of

fundamental knowledge, data fusion skills, and strong programming ability. Additionally, with the availability of those data, this work crosses boundaries by addressing a wide range of aerosol-cloud interaction processes across multiple scales in time and space. Nonetheless, it is also recognized in this work that the nature of aerosol-cloud interaction processes remains a challenging problem requiring careful analysis and caveats.

In this research, we first studied aerosol-cloud interactions in trade cumulus cloud regime using aircraft in situ data and high-resolution surface remote sensing data. More polluted clouds are associated with more and smaller cloud droplets. These clouds are substantially deeper and narrower with greater cloud liquid water path (LWP) than less polluted clouds. The deeper and narrower clouds in high polluted condition are mainly due to the warmer, more humid and shallower boundary layer and the intensified cloud edge evaporation effect as a result of aerosol loading. The changes in clouds that are embedded in a layer with a high concentration of absorbing aerosols over this region are not consistent with a reduction in cloud coverage and cloud LWP via the semi-direct effect. Instead, cloud cover and cloud LWP increase with increased black carbon aerosol. As a consequence of pollution aerosols, the regional top of atmosphere (TOA) shortwave (SW) forcing increases significantly due to the deeper clouds which develop under highly polluted conditions. This study focused on data from dry days to partially constrain the meteorological variations. However, the observed correlations cannot fully explain the cause and effect relationship between aerosols and clouds; further modeling studies are required to isolate the impact of aerosols from other meteorological impacts on cloud properties.

After investigating the marine cloud responses to aerosol, the focus was shifted to continental shallow warm clouds using multiple remote sensing data. Aerosol-cloud relationships were investigated under different meteorological conditions, and their influences on regional radiative forcing were examined. Results show that non-precipitating and precipitating clouds have similar responses to aerosol loading but different magnitudes. The key properties of cloud, including LWP, cloud optical thickness (COT), cloud fractional coverage (CF) and cloud thickness, generally increased with aerosol optical depth (AOD) for both types of cloud except for effective radius (R_e). The CF, LWP, COT and cloud thickness increase with increased AOD from 0 to 0.7. After that, these parameters generally decreased with increasing AOD. This indicates that aerosols favor cloud growth under relatively unpolluted conditions but likely to dissipate cloud at high pollution condition, mainly due to enhanced entrainment of overlying dry air which evaporates cloud droplets. The calculated ACI was generally higher under unstable, humid conditions and was lower under unstable, dry conditions. This was due to stronger entrainment of dry air above the cloud which increased mixing at the cloud top, evaporating cloud droplets leading to a loss of cloud water. Under stable conditions, the ACI is higher for precipitating than for non-precipitating clouds because the former are susceptible to precipitation suppression by aerosol-induced reduction in droplet size. The total TOA cloud radiative forcing (CRF) was estimated to be -80 W m^{-2} when the ACI increased to 0.3. Clouds with greater LWP exhibit a greater ACI as well as stronger CRF. Aerosol indirect forcing of the estimated anthropogenic portion of the aerosol due to the intrinsic aerosol effect was estimated to be -0.63 W m^{-2} and the forcing due to the extrinsic aerosol effect was estimated to be -1.77 W m^{-2} . This demonstrates the strong

radiative forcing associated with the aerosol indirect effect on cloud cover for the clouds observed during SEAC⁴RS.

In the last part, the errors due to sampling scale and remote sensing retrieval artifacts (aerosol humidification and 3-D radiation transfer) when quantifying aerosol indirect effects on shallow warm clouds were investigated by utilizing remote sensing, in situ data and a radiative transfer model. ACI shows a strong scale-dependent behavior. It decreases as data resolution decreases. Estimation of the ACI using in-situ aircraft data is similar to ACI derived from the enhanced MODIS Airborne Simulator (eMAS) data at 1 km resolution, but generally higher than ACIs derived using coarser resolution data. The MODIS-derived ACI is similar to eMAS derived ACI at 10 km resolution. This high-resolution remote sensing data demonstrates its ability to bridge the scale gap through data aggregation. 1-km resolution is sufficient to compare with in-situ measurement. The smoothing of aerosol and cloud fields may cause a large variation of estimated ACI which can be as high as 69% at 10 km resolution. It is therefore essential to biases arising from the spatial resolution of the data when estimating the aerosol-cloud interaction and associated radiative forcing. The biases in the ACI arising from artifacts related to remote sensing retrievals (aerosol humidification and 3-D radiation transfer) were evaluated. A Monte Carlo Radiation Transfer model was constructed and used together with in-situ and remote sensing observations. The results show that the aerosol humidification effect accounts for an 18.7% - 21.8% decrease in corrected estimated ACI. The magnitude of this effect depends on aerosol loading and its chemical composition. The effect should be larger for pollution-derived sulfate particles than for natural mineral dust. The 3-D radiative transfer effect enhances the reflectance in clear regions around broken clouds.

The 3-D effect can cause about a $\sim 10\%$ difference in ACI for a broken cloud scene. Three-D radiative effects in the regions near clouds are important in the understanding of aerosol indirect effects on climate from satellite observations. Thus, one should be cautious in applying the 1-D approximation in frequently-used plane-parallel radiative transfer models to compute clear-sky solar radiation in cumulus fields or using aerosol products derived from the 1-D approximation in aerosol indirect effect research.

2 Future work

In this study, we filtered data to consider only shallow warm cloud and limited AOD above cloud to be very small. However, aerosol layers lofted in the atmosphere are frequently observed, and these aerosols can absorb solar radiation, changing atmospheric stability, circulation, and ultimately cloud properties, especially when absorbing aerosols are presented. Those absorbing aerosols can initially overlay the cloud deck, but later subside and are mixed into the clouds. These interactions include adjustments to aerosol-induced solar heating and microphysical effects which remain a large uncertainty. In future work, it is of great interest to investigate this problem. Also, the aerosol effects on cirrus clouds are more uncertain than warm liquid clouds. Cirrus clouds are of particular importance since they have extensive global coverage (20-25% globally and as much as 70% over tropics) and occur high in the atmosphere, indicating such clouds can exert an overall warming effect like GHGs do (different from shallow warm clouds which exerting a net cooling effect) and act as one of the major modulators of the global radiation budget. It is meaningful to apply some techniques used in this dissertation to study the cirrus clouds response to aerosols and their impacts on climate forcing.